

In-situ and Ex-situ Observations of Lithium De-intercalation from  $\text{LiCoO}_2$ :  
Atomic Force Microscopy and Transmission Electron Microscopy Studies

by

Anne Cléménçon

Diplôme d'Ingénieur de l'Ecole Polytechnique, France,  
2005

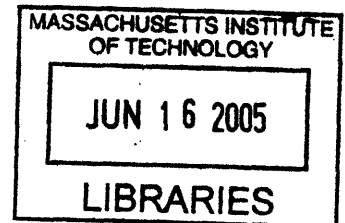
SUBMITTED TO THE DEPARTMENT OF MECHANICAL ENGINEERING IN  
PARTIAL FULFILLMENT OF THE REQUIREMENTS FOR THE DEGREE OF  
MASTER OF SCIENCE IN MECHANICAL ENGINEERING

at the

MASSACHUSETTS INSTITUTE OF TECHNOLOGY

June 2005

© 2005 Massachusetts Institute of Technology  
All rights Reserved



Signature of Author: \_\_\_\_\_  
Department of Mechanical Engineering  
May 2005

Certified by: \_\_\_\_\_  
Yang Shao-Horn  
Atlantic Richfield Career Development Assistant Professor of Mechanical Engineering  
Thesis Supervisor

Accepted by: \_\_\_\_\_  
Lallit Anand  
Professor of Mechanical Engineering  
Chairman, Department Graduate Committee

**BARKER**

Report Documentation Page			Form Approved OMB No. 0704-0188		
Public reporting burden for the collection of information is estimated to average 1 hour per response, including the time for reviewing instructions, searching existing data sources, gathering and maintaining the data needed, and completing and reviewing the collection of information. Send comments regarding this burden estimate or any other aspect of this collection of information, including suggestions for reducing this burden, to Washington Headquarters Services, Directorate for Information Operations and Reports, 1215 Jefferson Davis Highway, Suite 1204, Arlington VA 22202-4302. Respondents should be aware that notwithstanding any other provision of law, no person shall be subject to a penalty for failing to comply with a collection of information if it does not display a currently valid OMB control number.					
1. REPORT DATE <b>JUN 2005</b>		2. REPORT TYPE		3. DATES COVERED <b>00-06-2005 to 00-06-2005</b>	
4. TITLE AND SUBTITLE <b>In-situ and Ex-situ Observations of Lithium De-intercalation from LiCoO2: Atomic Force Microscopy and Transmission Electron Microscopy Studies</b>				5a. CONTRACT NUMBER	
				5b. GRANT NUMBER	
				5c. PROGRAM ELEMENT NUMBER	
6. AUTHOR(S)				5d. PROJECT NUMBER	
				5e. TASK NUMBER	
				5f. WORK UNIT NUMBER	
7. PERFORMING ORGANIZATION NAME(S) AND ADDRESS(ES) <b>Massachusetts Institute of Technology, Department of Mechanical Engineering, 77 Massachusetts Avenue, Cambridge, MA, 02139</b>				8. PERFORMING ORGANIZATION REPORT NUMBER	
9. SPONSORING/MONITORING AGENCY NAME(S) AND ADDRESS(ES)				10. SPONSOR/MONITOR'S ACRONYM(S)	
				11. SPONSOR/MONITOR'S REPORT NUMBER(S)	
12. DISTRIBUTION/AVAILABILITY STATEMENT <b>Approved for public release; distribution unlimited</b>					
13. SUPPLEMENTARY NOTES					
14. ABSTRACT					
15. SUBJECT TERMS					
16. SECURITY CLASSIFICATION OF:			17. LIMITATION OF ABSTRACT	18. NUMBER OF PAGES <b>108</b>	19a. NAME OF RESPONSIBLE PERSON
a. REPORT <b>unclassified</b>	b. ABSTRACT <b>unclassified</b>	c. THIS PAGE <b>unclassified</b>			

# In-situ and Ex-situ Observations of Lithium De-intercalation from $\text{LiCoO}_2$ : Atomic Force Microscopy and Transmission Electron Microscopy Studies

by

Anne Cl  men  on

Submitted to the Department of Mechanical Engineering in May 2005 in Partial  
Fulfillment of the Requirements for the Degree of Master of Science  
in Mechanical Engineering

## ABSTRACT

Lithium cobalt dioxide is the most commonly used material for positive electrodes in lithium rechargeable batteries. During lithium de-intercalation from this material,  $\text{Li}_x\text{CoO}_2$  undergoes a number of phase transitions, which have been studied by bulk techniques and first-principles calculations. The objective of this work was to examine the effect of charge and discharge on individual  $\text{LiCoO}_2$  crystals. Atomic Force Microscopy and Transmission Electron Microscopy were used to observe the effects of lithium ion de-intercalation from  $\text{Li}_x\text{CoO}_2$  in individual crystals.

This work was the first study to use in-situ Atomic Force Microscopy to probe the dynamic evolution of  $\text{Li}_x\text{CoO}_2$  crystal morphology as lithium ions are de-intercalated from the material. The overall crystal morphology did not seem to evolve very much during the first charge and discharge cycle however evidence was found for expansion and contraction of crystal steps during cycling. The evolution of layer spacing was quantified from AFM data and was found to be in agreement with X-ray diffraction studies by other researchers. Furthermore, rounded bumps were observed on the surface of most of the crystals, and it is speculated that these bumps are  $\text{Li}_2\text{CO}_3$  impurities, formed on the surface of  $\text{LiCoO}_2$  after storage in air. Lastly, the formation of a surface layer on  $\text{Li}_x\text{CoO}_2$  crystals and the gold foil substrate was observed when the cell was over-discharged to approximately 2.5V.

Transmission Electron Microscopy was used to image individual  $\text{Li}_x\text{CoO}_2$  crystals for different values of lithium concentration in the range corresponding to the insulator-metal phase transition. Electron diffraction patterns revealed the presence of lithium-vacancy ordering in charged  $\text{Li}_x\text{CoO}_2$  samples. In parallel, Electrochemical Impedance Spectroscopy and X-ray Diffraction were used to characterize the evolution of the electronic and structural properties of  $\text{Li}_x\text{CoO}_2$  during the phase transition. EIS data showed that the electronic resistivity of  $\text{Li}_x\text{CoO}_2$  decreased by three orders of magnitude at the onset of charge, in agreement with literature. XRD data from charged  $\text{Li}_x\text{CoO}_2$  samples showed an increase in layer spacing, also in good agreement with previous studies done by other researchers.

Thesis Supervisor: Yang Shao-Horn

Title: Atlantic Richfield Career Development Assistant Professor of Mechanical Engineering

## **Acknowledgements**

The author would like to acknowledge the Office of Naval Research for funding this project through the Young Investigator Award N00014-03-10448.

I am very thankful to my Academic Research Advisor Yang Shao-Horn for her guidance and the time she spent helping me throughout this project. I also thank her for securing funding for this project and for running the Electrochemical Energy Laboratory at MIT.

I also wish to acknowledge all the graduate students of the Electrochemical Energy Laboratory, particularly Elisa Alonso for her help in the laboratory and for collecting the Scanning Electron Microscopy images. Special thanks to Dr. Sundeep Kumar, who helped me with AC impedance data analysis and collecting FT-IR, as well as for his advice on many aspects of the project.

## Table of contents

ABSTRACT.....	3
Acknowledgements.....	4
List of figures.....	6
Introduction.....	13
Atomic force microscopy studies of lithium battery materials.....	17
The insulator-metal transition in $\text{Li}_x\text{CoO}_2$ .....	19
1 Synthesis and characterization of the $\text{LiCoO}_2$ parent sample.....	29
1.1 Solid-state synthesis of $\text{LiCoO}_2$ .....	29
1.2 Preparation of composite electrodes and coin cells.....	29
1.3 Characterization of the parent sample.....	30
2 A study of the morphological evolution of individual $\text{LiCoO}_2$ crystals during cycling by AFM.....	33
2.1 Experimental.....	33
2.1.1 Preparation and characterization of gold and crystals electrodes.....	33
2.1.2 AFM imaging.....	36
2.2 Results and discussion.....	39
2.2.1 Objectives.....	39
2.2.2 General crystal morphology and tip shape effects.....	40
2.2.3 Surface features on the crystals.....	45
2.2.4 Evolution of crystal morphology during charge and discharge.....	50
2.2.5 The effect of over-discharge.....	67
2.3 Conclusions.....	72
3 TEM studies and AC impedance studies of $\text{Li}_x\text{CoO}_2$ .....	73
3.1 Experimental.....	73
3.1.1 Preparation of coin cells.....	73
3.1.2 XRD testing.....	73
3.1.3 TEM testing.....	74
3.1.4 AC impedance spectroscopy.....	74
3.2 Results and discussion.....	75
3.2.1 X-ray diffraction results and discussion.....	75
3.2.2 Transmission Electron Microscopy results and discussion.....	79
3.2.2.1 Characterization of the parent sample.....	79
3.2.2.2 Single-phase $\text{Li}_x\text{CoO}_2$ with lithium content in the range 0.7-0.75.....	81
3.2.2.3 Single-phase $\text{Li}_x\text{CoO}_2$ with a lithium content in the range 0.97 - 0.95.....	87
3.2.2.4 Two-phase $\text{Li}_x\text{CoO}_2$ with a lithium content of 0.85.....	89
3.2.2.5 Open questions.....	91
3.2.2.6 Bright-field TEM images of charged $\text{Li}_x\text{CoO}_2$ samples.....	92
3.2.2.7 General remarks.....	94
3.2.3 Electrochemical Impedance Spectroscopy results and discussion.....	95
Conclusion.....	104
References.....	106

## List of figures

- Figure 1: Crystal structure of  $\text{LiCoO}_2$ .  $\text{LiCoO}_2$  has a layered structure consisting of lithium and cobalt sheets stacked alternatively between oxygen sheets. Li and Co occupy octahedral sites in alternating layers between the oxygen planes. This structure can be described as having rhombohedral symmetry with space group  $R\bar{3}m$ . The cell parameters are  $a=2.815\text{\AA}$  and  $c=14.05\text{\AA}$ . ..... 14
- Figure 2: Phase stability in  $\text{Li}_x\text{CoO}_2$  as a function of lithium concentration, calculated from first principles [5]. ..... 16
- Figure 3: Evolution of  $\text{Li}_x\text{CoO}_2$  cell parameters as a function of lithium content [7]. At the onset of charge, lithium ions are removed from lithium planes and the electrostatic forces acting between the neighboring oxygen planes cause them to move apart, increasing the cell parameter  $c$ . At a lithium concentration of approximately  $x=0.5$ , the  $c$  parameter reaches a maximum. For lithium concentrations below  $x=0.5$ , the layer spacing contracts. .... 16
- Figure 4: Evolution of the electrical conductivity of  $\text{Li}_x\text{CoO}_2$  as a function of reciprocal temperature ..... 27
- Figure 5: Equivalent circuit proposed by Levi et al. to model the electroanalytical behavior of  $\text{Li}_x\text{CoO}_2$  electrodes [29]. ..... 27
- Figure 6: Equivalent circuit proposed by Dokko et al. to model the electroanalytical behavior of  $\text{Li}_x\text{CoO}_2$  single-particles [31]. ..... 28
- Figure 7: Equivalent circuits proposed by Nobili et al. to model the electroanalytical behavior of  $\text{Li}_x\text{CoO}_2$  composite electrodes. Circuit (a) is inspired by Levi et al. while circuit (b) is inspired by Bruce et al. [30]. ..... 28
- Figure 8: XRD pattern of  $\text{LiCoO}_2$ , measured with a Rigaku RU300 powder diffractometer, using copper  $K\alpha$  radiation. X-ray diffraction data was collected in theta-two theta reflection mode, at  $2^\circ$  per minute scan rate, between  $10^\circ$  and  $90^\circ$ .  $\text{LiCoO}_2$  was synthesized from  $\text{Li}_2\text{CO}_3$  and  $\text{Co}_3\text{O}_4$  in air at  $600^\circ\text{C}$  for 12 hours and at  $900^\circ\text{C}$  for 24 hours. .... 31
- Figure 9: Close-up of the XRD pattern of  $\text{LiCoO}_2$ , on the  $15^\circ$ -  $62^\circ$  range. .... 31
- Figure 10: Electrochemical cycling of a  $\text{LiCoO}_2$  positive electrode vs. lithium metal. The first cycle corresponds to the full line and the second cycle to the dotted line. The coin cell was cycled at a rate of  $C/50$  (theoretical full charge in 50 hours) using a Solartron 1470 Battery Tester. The applied current was equal to  $5.48\text{mA/g}$  of active material. .... 32

- Figure 11: SEM image of a gold foil with  $\text{LiCoO}_2$  crystals pressed onto it. The  $\text{LiCoO}_2$  crystals are distributed evenly on the surface and lie flat on the foil. Indentations left by other crystals can also be seen on the foil (indicated by arrows)..... 35
- Figure 12: Cyclic voltammetry curve of a coin cell containing lithium metal as the negative electrode, gold foil as the positive electrode, and  $\text{LiPF}_6$  in EC:DMC (1:1) as the electrolyte. Cellgard 2500 microporous polypropylene membranes were used as separator. In the 2.5-4.5V interval, the cycles do not exhibit any feature, indicating that lithium does not react with gold at those potentials..... 35
- Figure 13: Top view and side view of the AFM sample stage with in-situ electrochemical cell..... 38
- Figure 14: Pictures of the AFM cell setup. An open battery is assembled inside the sample holder provided by Veeco Instruments. The positive electrode ( $\text{LiCoO}_2$  crystals pressed onto a gold foil) is placed at the center of the holder and clamped under a Teflon ring. The counter and reference electrodes are made from lithium foil and are supported by a groove in the Teflon ring. In some experiments, the lithium electrodes were connected directly to the two screws. In other experiments, a copper wire was used as current collector between the screws and the foil. The counter electrode is made circular to ensure homogeneous current distribution. Black insulating tape is used to hold the cell in place on the sample stage, and to avoid shorting the cell. Later in the experiment, electrolyte is poured into the Teflon ring. .... 38
- Figure 15: SEM image of a  $\text{LiCoO}_2$  crystal pressed on a gold foil. The crystal is cracked in the middle, probably due to the application of pressure to embed the crystals in gold. Very few crystals exhibit such cracks. This crystal has the typical plate-like shape of  $\text{LiCoO}_2$  crystals; the flat surface on the top of the crystal most probably corresponds to the (003) plane orientation. The crystal shows two types of growth steps which are often seen on  $\text{LiCoO}_2$  crystals: steps parallel to the basal plane, and steps in the orthogonal direction. The shape of the crystal is slightly rounded, which could be a sign that the sample is slightly overstoichiometric in lithium. .... 42
- Figure 16: SEM image of  $\text{LiCoO}_2$  crystals dispersed on a gold foil. Most of the crystals lie flat on the foil. Some crystals have clear growth steps on the edges, others are more rounded. .... 42
- Figure 17: 3D image of a typical AFM scan of a  $\text{LiCoO}_2$  crystal. The scan is  $7.843\text{ }\mu\text{m} \times 7.843\text{ }\mu\text{m}$ . The sides of the crystal are slanted, with different angles in different directions. The arrows indicate the slant angle. .... 43
- Figure 18: 3D image of an AFM scan showing  $\text{LiCoO}_2$  crystals dispersed on a gold foil. Most of the crystals have slanted sides, and the all the crystals seem to be slanted in the same direction. The arrows indicate the slant angle. The discrepancy between the

AFM images of the crystals and the SEM images of similar crystals arises from the convolution of the tip shape with the sample morphology in AFM imaging. .... 43

Figure 19: Characteristics of the silicon nitride probes used in Contact Mode AFM imaging. The probes are NP probes from Veeco Instruments. The tip has a pyramidal shape and is mounted on a cantilever. The front, back and side angles of the tip are approximately  $35^\circ$ . The tip mounting angle is  $10.5^\circ$ , therefore in effect the front angle of the tip is approximately  $45^\circ$  and the back angle is  $25^\circ$ . .... 44

Figure 20: Schematic showing the effect of tip shape on the height profile measured by AFM. As the tip scans the surface of the sample, the tip side walls can hit a crystal even though the tip end is on the gold foil. Therefore this type of tip cannot measure steep inclines accurately. .... 44

Figure 21: 3D image of an AFM scan showing  $\text{LiCoO}_2$  crystals. The scan size is  $4.185\mu\text{m}$ . This scan was performed in argon, in the absence of electrolyte. There are rounded bumps on the surface of the crystals and similar bumps are seen on most  $\text{LiCoO}_2$  crystals. The bumps are 50-250 nm in diameter and 5-15 nm in height. The black square indicates where a close-up scan was performed. .... 47

Figure 22: AFM scan of the surface of a  $\text{LiCoO}_2$  crystal. The scan size is  $0.9\mu\text{m}$ . The color scale indicates the topography of the sample. This image is a close-up of the crystal top surface shown in Figure 21. The bumps on the surface of the crystal are 50 to 250nm in diameter, and 5 to 15 nm in height. Some of the bumps seem to have similar shapes. This is most probably a tip shape artifact..... 47

Figure 23: X-ray diffraction pattern of the  $\text{LiCoO}_2$  sample after storage in air for 6 months, zoomed on the background for angles  $15^\circ$ - $40^\circ$ . The pattern shows the presence of  $\text{Li}_2\text{CO}_3$  impurities in the sample. It is believed that  $\text{Li}_2\text{CO}_3$  is a product of the reaction between  $\text{LiCoO}_2$  and  $\text{CO}_2$  present in air. .... 48

Figure 24: FT-IR spectra of  $\text{Li}_2\text{CO}_3$  and  $\text{LiCoO}_2$ . The data were collected in transmittance mode on a Thermo Nicolet Magna 860 (USA), and a pellet was prepared for imaging with approximately 95% KBr and 5%  $\text{Li}_2\text{CO}_3$  or  $\text{LiCoO}_2$ . The KBr spectrum was removed from the data shown here. The  $\text{LiCoO}_2$  sample was stored in air for 6 months after synthesis and shows the presence of  $\text{Li}_2\text{CO}_3$  on the surface of the crystals: the  $\text{LiCoO}_2$  spectrum has a peak around  $870\text{cm}^{-1}$ , which corresponds to the peak attributed to the bending mode of  $\text{CO}_3$  (shown with an asterisk on the graphs)..... 48

Figure 25: 3D images of AFM scans. The scan size is  $1.165\mu\text{m}$ . All three scans correspond to the same area of the crystal edge, and imaging as done in electrolyte, without applying an electric current. The images, from left to right, were recorded at the beginning of the experiment, after 15 minutes, and after one hour. The bumps present on the face of the crystal seem to disappear gradually over time..... 49



Figure 26: Potential curve of the in-situ electrochemical cell used in experiment 050605 (left) shown alongside the potential curve of coin cell 083004b_11 (right). The AFM cell was charged galvanostatically at a rate of C/4 to an approximate lithium content of $x=0.5$ . After a 30 minute rest step, the cell was discharged at C/4. The reference coin cell was cycled at a rate of C/50. ....	53
Figure 27: 3D images of AFM scans in experiment 050605. The same crystal is shown initially, at the end of charge, during discharge, and at the end of discharge. The overall morphology of the crystal does not seem to evolve much. The height of the steps on the sides of the crystal were measured and their evolution was studied throughout cycling. ....	54
Figure 28: Measure of the step height on the crystal. ....	55
Figure 29 : Evolution of the step height during experiment 050605. Step a was measured for different lithium contents. ....	55
Figure 30: Potential curve of AFM cell 050605 as a function of time. The cell was charged and discharged at a rate of C/4 and held at open-circuit for 30 min between charge and discharge. ....	56
Figure 31: Potential curve of the in-situ electrochemical cell used in experiment 042505 (left) shown alongside the potential curve of coin cell 083004b_11 (right). The AFM cell was charged galvanostatically at a rate of C/2 to an approximate lithium content of $x=0.5$ . After a 10 minute rest step, the cell was discharged at C/2. The reference coin cell was cycled at a rate of C/50. ....	59
Figure 32: 3D images of AFM scans in experiment 042505. The same crystal is shown initially, at the end of charge, during discharge, and at the end of discharge. Another crystal was present on the left-hand side of the top images. This crystal disappeared in later images, probably pushed away by the AFM tip. The overall morphology of the crystal does not seem to evolve much. The heights of the steps on the sides of the crystal were measured and their evolution was studied throughout cycling. ....	60
Figure 33: Measures of the step heights on the edge of the crystal, in two directions. ....	61
Figure 34: Evolution of the step height during experiment 042505. Steps a and d correspond to the same feature on the crystal, measured in different directions. Therefore the evolution of the average of steps a and d was analyzed. ....	61
Figure 35: Potential curve of the in-situ electrochemical cell used in experiment 042506. The cell was charged galvanostatically at a rate of C/2 to an approximate lithium content of $x=0.5$ . After a 10 minute rest step, the cell was discharged at C/2. ....	62
Figure 36: Evolution of $\text{Li}_x\text{CoO}_2$ cell parameters as a function of lithium content [7]. ...	66

- Figure 37: Mechanism for step expansion during charge. Lithium ions are first pulled out of selected layers. As lithium ions are pulled out of one layer, vacancies are created and the diffusivity of lithium ions increases. Therefore it is easier to remove more lithium ions from that same layer. .... 66
- Figure 38: Voltage curve of the in-situ AFM cell 042505. The working electrode is  $\text{LiCoO}_2$  crystals pressed onto a gold foil, the counter and reference electrodes are lithium metal, and the electrolyte is  $\text{LiPF}_6$  in EC:DEC. The cell was charged halfway and discharged at  $C/2$ . The cell does not recharge entirely, and the cell potential drops significantly at the end of discharge. .... 69
- Figure 39: 3D images and height images corresponding to two AFM scans of a crystal in sample 042505 during discharge of the cell. The three-dimensional images show the entire crystal. The height images represent a zoomed image of the top surface of the crystal. The image size is  $1\mu\text{m}$  and the height scale is 50nm, the same in both images. The images on the left were taken when the cell potential was 3.39V, and the images on the right were taken when the cell potential was 2.36V. The images corresponding to the lower potential show that surface features have appeared on the surface of the crystal. .... 70
- Figure 40: Potential curve of in-situ cell used in experiment 042605. The cell was charged and discharged halfway at  $C/2$ . The potential drops sharply at the end of discharge and seems to plateau again at approximately 2.3V. .... 71
- Figure 41: Three-dimensional images of consecutive AFM scans of the gold foil at the end of the discharge of cell 042604. The indentation in the gold foil was left by a crystal which was pushed away by the AFM tip. The image on the left was recorded at a cell potential of 2.343V, and the image on the right at 2.336V. Some rounded bumps appear on the gold foil between the two scans. .... 71
- Figure 42: X-ray diffraction pattern of as-prepared and charged samples of  $\text{Li}_x\text{CoO}_2$  for  $x=0.97, 0.85, 0.75$ . .... 76
- Figure 43: X-ray diffraction pattern of as-prepared and charged samples of  $\text{Li}_x\text{CoO}_2$  for  $x=0.97, 0.85, 0.75$ : close-up of the (003) peak. As lithium is de-intercalated from the material, the layer spacing increases, which causes the (003) peak to shift to the lower angles. .... 77
- Figure 44: X-ray diffraction pattern of as-prepared and charged samples of  $\text{Li}_x\text{CoO}_2$  for  $x=0.97, 0.85, 0.75$ : close-up on the  $35^\circ$ - $55^\circ$  range. As lithium is de-intercalated from the material, the layer spacing increases, which causes the (006) peak to shift to the lower angles. .... 77
- Figure 45: Electron diffraction patterns of the  $\text{LiCoO}_2$  parent phase. These diffraction patterns are indexed to the hexagonal cell and do not have super-lattice reflections.

The zone axes are $[-1\ 1\ 1]_{\text{hex}}$ for the pattern on the top and $[1\ -1\ 2]_{\text{hex}}$ for the pattern in the center, $[001]_{\text{hex}}$ for the pattern on the bottom. ....	80
Figure 46: Electron diffraction patterns of a sample charged to a composition of $\text{Li}_{0.7}\text{CoO}_2$ (on the left), compared with diffraction patterns of the $\text{LiCoO}_2$ parent sample (on the right). The diffraction pattern of the charged sample has super-lattice reflections, indicated by white arrows. ....	82
Figure 47: Schematics of (a) lithium ion positions in the $\text{LiCoO}_2$ parent sample, (b) proposed lithium ion positions in $\text{Li}_{0.7}\text{CoO}_2$ in a hexagonal cell and (c) proposed lithium ion positions in $\text{Li}_{0.7}\text{CoO}_2$ in a monoclinic cell. The black dots represent lithium ions, the white dots represent vacancies and the gray dots represent a statistical distribution of lithium ions and vacancies. ....	83
Figure 48: Crystallographic relationship between the hexagonal $\text{LiCoO}_2$ and monoclinic cell. ....	84
Figure 49: Electron diffraction pattern of a sample charged to a composition of $\text{Li}_{0.75}\text{CoO}_2$ (on the left), compared with a diffraction pattern of the $\text{LiCoO}_2$ parent sample (on the right). The diffraction pattern of the charged sample has super-lattice reflections, indicated by white arrows. ....	86
Figure 50: Schematics of lithium ion positions in $\text{Li}_{0.75}\text{CoO}_2$ in a hexagonal cell. The black dots represent lithium ions and the white dots represent vacancies. The supercell is $2a_{\text{hex}} \times 2a_{\text{hex}} \times c_{\text{hex}}$ . ....	86
Figure 51: Electron diffraction pattern of a sample charged to a composition of $\text{Li}_{0.97}\text{CoO}_2$ (on the left), compared with a diffraction pattern of the $\text{LiCoO}_2$ parent sample (on the right). The diffraction pattern of the charged sample has super-lattice reflections, indicated by white arrows. ....	88
Figure 52: Schematics of lithium ion positions in $\text{Li}_{0.97}\text{CoO}_2$ in a monoclinic cell. The black dots represent lithium ions and the gray dots represent sites partially occupied by lithium ions. The supercell is $2a_{\text{mon.}} \times 2a_{\text{mon.}} \times 4c_{\text{mon.}}$ . ....	88
Figure 53: Electron diffraction patterns of a sample charged to a composition of $\text{Li}_{0.85}\text{CoO}_2$ (on the left), compared with diffraction patterns of the $\text{LiCoO}_2$ parent sample (on the right). The diffraction pattern of the charged sample has super-lattice reflections, indicated by white arrows. ....	90
Figure 54: Electron diffraction patterns from a charged $\text{Li}_{0.85}\text{CoO}_2$ sample. The proposed model cannot explain the super-lattice reflections present in these patterns. ....	91
Figure 55: Bright-field TEM images of crystals charged to a lithium content of 0.85. There are microstructures on the edges of the crystals, which could correspond to domains of the insulating and the metallic phases. ....	93

Figure 56: Charge curves of cells 10 (a) and 14 (b), used in AC impedance measurements. Both coin cells were charged at a slow rate of C/100 and the charge was interrupted in order to perform impedance spectroscopy measurements at different lithium contents. Measurements were taken at $x=1, 0.95, 0.9, \dots 0.7$ for coin cell 083004b_10 and at $x=1, 0.98, 0.96, \dots 0.7, 0.6$ and $0.5$ for coin cell 083004b_14. Before and after each impedance step, the cell was allowed to reach equilibrium for 10min at open-circuit.....	96
Figure 57: Nyquist and Bode plots of coin cells 083004b_10 (a) and 083004b_14 (b). Impedance was measured for frequencies ranging from 10kHz to 15mHz, with a perturbation voltage of 5mV.....	97
Figure 58: Equivalent circuits modeling the behavior of lithium batteries. All of these circuits were used to fit the experimental data, with similar results. In the analysis of the data, circuit (a) was chosen because it is a better representation of the physics of a lithium battery. ....	101
Figure 59: Intercalation capacitance a function of lithium content $x$ , for coin cells 083004b_10 (a) and 083004b_14 (b). $C_{\text{int}}$ was calculated according to: $C_{\text{int}} = -\frac{1}{(\omega Z_w^n)_{\omega \rightarrow 0}}$ .....	102
Figure 60: Electronic resistance of the composite electrode as a function of lithium content $x$ , for coin cells 083004b_10 (a) and 083004b_14 (b). $R_e$ was assessed by fitting the AC impedance data according to the equivalent circuit (a) shown in Figure 58. ....	102
Figure 61: Charge transfer resistance as a function of lithium content $x$ , for coin cells 083004b_10 (a) and 083004b_14 (b). $R_e$ was assessed by fitting the AC impedance data according to the equivalent circuit (a) shown in Figure 47.....	103

## Introduction

Lithium rechargeable batteries are well designed for light portable applications such as laptops and cell phones because of their high energy density. They are also used in hybrid vehicles, as well as for military applications. Lithium is the most electropositive (-3.04V vs. standard hydrogen electrode) and the lightest metal (molar mass: 6.94g/mol), ensuring that lithium batteries have a high energy density. However, lithium rechargeable batteries suffer from capacity fade and slow recharging. Capacity fade is linked to the change of material properties due to repeated charge/discharge cycles. During repeated cycling, some of the active material can become inactive, decreasing the capacity of the battery. Furthermore, the speed at which a battery can be charged or discharged has to do with how fast lithium ions can migrate through the different components and the interfaces that separate them. Therefore it is necessary to optimize the material and interfaces properties to allow faster recharging of the battery.

Most commercial lithium batteries use lithium cobalt dioxide ( $\text{LiCoO}_2$ ) as the positive electrode material. The voltage of  $\text{Li}_x\text{CoO}_2$  vs. lithium metal is approximately 4V, high enough to provide a good energy density to the battery, and not high enough to cause electrolyte decomposition.

When synthesized at high temperature (800°C),  $\text{LiCoO}_2$  has a layered structure consisting of lithium and cobalt sheets stacked alternatively between ABCABC close-packed oxygen arrays. Li and Co occupy octahedral sites in alternating layers between the oxygen planes. This structure can be described as having rhombohedral symmetry with space group  $R\bar{3}m$  (Figure 1). The cell parameters are  $a=2.815\text{\AA}$  and  $c=14.05\text{\AA}$  [1]. During cycling of the battery, lithium ions intercalate in and de-intercalate out of the lithium planes in the  $\text{Li}_x\text{CoO}_2$  layered structure.

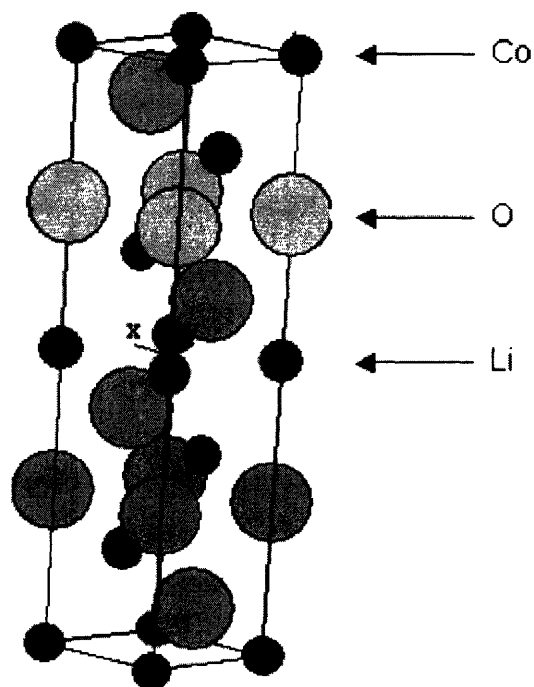


**Figure 1: Crystal structure of  $\text{LiCoO}_2$ .**  $\text{LiCoO}_2$  has a layered structure consisting of lithium and cobalt sheets stacked alternatively between oxygen sheets. Li and Co occupy octahedral sites in alternating layers between the oxygen planes. This structure can be described as having rhombohedral symmetry with space group  $R\bar{3}m$ . The cell parameters are  $a=2.815\text{\AA}$  and  $c=14.05\text{\AA}$ .

LiCoO<sub>2</sub> has a theoretical specific capacity of 274mAh/g. However, commercial batteries typically achieve a reversible capacity of 140mA/g by using an upper cutoff voltage of 4.2V, corresponding to the de-intercalation and intercalation of 0.5 Li ions per unit cell LiCoO<sub>2</sub>. Charging the lithium batteries beyond the upper cutoff voltage of 4.2V induces capacity loss. Several causes have been proposed for this capacity fade, involving both the bulk and the surface of the LiCoO<sub>2</sub> crystals. During cycling, the layered structure of Li<sub>x</sub>CoO<sub>2</sub> undergoes expansion and contraction, creating stresses and strains inside the material [2], [3]. When the strains become too large for the material to sustain, the structure changes. Capacity decreases when the number of lithium ions that can intercalate back into the host structure decreases. Strains can also cause cracks, dislocations and stacking faults leading to loss of electronic contact between particles [4].

Li<sub>x</sub>CoO<sub>2</sub> exhibits a number of phase transformations (Figure 2). As the battery is charged and discharged, the lithium content  $x$  in Li<sub>x</sub>CoO<sub>2</sub> changes and a phase transformation occurs when a new thermodynamically stable phase can be created. It is believed that phase transformations have a negative effect on the reversibility of the intercalation/de-intercalation of lithium ions. Phase transformations have been widely studied using experimental techniques as well as ab initio calculations.

Van der Ven et al. calculated the phase diagram of Li<sub>x</sub>CoO<sub>2</sub> from first principles [5]. They found that the layered O3 phase is stable for lithium contents superior to  $x=0.3$ . They also predicted in-plane ordering of lithium ions around  $x=0.5$  and  $x=0.3$ . Ordering at  $x=0.5$  was also reported by Reimers and Dahn from in-situ X-ray diffraction (XRD) studies [6]. The lattice constants calculated by Van der Ven et al. agree well with the measurements reported by Amatucci et al. from X-ray diffraction [7] (Figure 3). When lithium content is  $x=0.5$ , the layer expansion reaches a maximum. It is therefore expected that most of the damage due to stresses and strain in the material occurs for lithium concentrations around  $x=0.5$ .

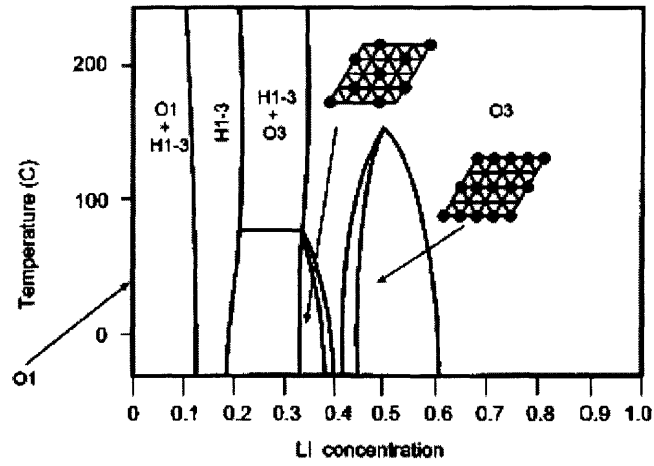


Figure 2: Phase stability in  $\text{Li}_x\text{CoO}_2$  as a function of lithium concentration, calculated from first principles [5].

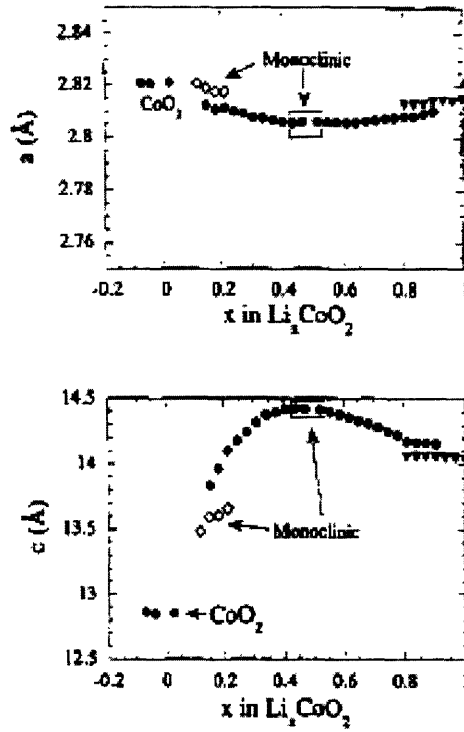


Figure 3: Evolution of  $\text{Li}_x\text{CoO}_2$  cell parameters as a function of lithium content [7]. At the onset of charge, lithium ions are removed from lithium planes and the electrostatic forces acting between the neighboring oxygen planes cause them to move apart, increasing the cell parameter  $c$ . At a lithium concentration of approximately  $x=0.5$ , the  $c$  parameter reaches a maximum. For lithium concentrations below  $x=0.5$ , the layer spacing contracts.



The motivation of this work is to examine the effect of charge and discharge on individual crystals, in an effort to better understand some of the reasons of capacity fade. This work has two main parts. The first part examines the evolution of crystal morphology during cycling by Atomic Force Microscopy (AFM). The second part studies the insulator-metal transition in  $\text{Li}_x\text{CoO}_2$  by Transmission Electron Microscopy (TEM) and Electrochemical Impedance Spectroscopy (EIS).

## **Atomic force microscopy studies of lithium battery materials**

AFM can provide unique insight on the effect of electrochemical cycling on individual crystals. Using in-situ Atomic Force Microscopy coupled with electrochemical cycling, it is possible to probe the dynamic evolution of crystal morphology during cycling. In-situ AFM has been used by other researchers to study electrode materials in lithium batteries. A number of these studies have to do with surface film formation on the negative electrode: lithium or graphite [8], [9], [10], [11]. A few studies have concentrated on positive electrode materials such as  $\text{MoO}_3$  and  $\text{LiMn}_2\text{O}_4$  [12], [13], [14].

Koltypin et al. studied the evolution of composite graphite electrodes during lithium intercalation and de-intercalation by in-situ AFM [8]. The composite electrodes (graphite flakes, PVdF, copper current collector) were cycled vs. lithium metal in EC:DMC electrolyte containing  $\text{LiPF}_6$  or  $\text{LiAsF}_6$  salts. The same graphite flake was successfully imaged continuously during an entire intercalation and de-intercalation cycle and morphological changes were observed.

Bullard and Smith studied the evolution of the (010) surface of a  $\text{MoO}_3$  single crystal during lithium intercalation by in-situ AFM [12]. In-situ AFM images showed the nucleation and growth of  $\text{Li}_x\text{MoO}_3$  precipitates at the (010) surface, preferentially on surface steps. The strain caused by the expansion of the layers creates cracks in the crystal.

Vidu et al. imaged  $\text{LiMn}_2\text{O}_4$  composite electrodes using ex-situ and in-situ Electrochemical Atomic Force Microscopy and Lateral Force Microscopy [13, 14]. In-situ EC-AFM and LFM scans were performed under potentiostatic conditions on

composite electrodes ( $\text{LiMn}_2\text{O}_4$ , acetylene black and Teflon) placed in an electrochemical cell containing lithium foil and  $\text{LiPF}_6$  electrolyte. They reported the formation of a surface film as soon as the positive electrode was brought into contact with the electrolyte. They also observed the dissolution of surface particles during charging, and analyzed the rate of dissolution quantitatively by height distribution functions. Furthermore, the effect of polymer coating of  $\text{LiMn}_2\text{O}_4$  on the thermal stability of the material was also studied by in-situ AFM. It was shown that during a charge/discharge cycle, surface morphology changes are much smaller on the material with a polymer coating.

Lastly, a recent study by Campana et al. quantified the step height evolution in highly oriented pyrolytic graphite during lithium intercalation and de-intercalation [15]. During the first cycle, an irreversible increase in step height of  $24 \pm 7\%$  was measured in 1 M  $\text{LiClO}_4$  in EC:DMC. On subsequent intercalation/ de-intercalation cycles, a reversible change in graphene layer spacing of  $\pm 17\%$  was evidenced. The authors argued that the statistical procedure they use to measure the step height yields more accurate results than the examination of single line scans, because of the presence of a thick and uneven surface layer of the surface of the graphite.

To the best of our knowledge, no study of individual crystals of  $\text{LiCoO}_2$  by in-situ AFM has been reported in literature. We propose to examine the morphological evolution of individual  $\text{Li}_x\text{CoO}_2$  crystals during lithium intercalation and de-intercalation by in-situ AFM. In order to isolate the intrinsic properties of  $\text{LiCoO}_2$  crystals and dispense with the use of binder and carbon additives, the AFM samples consist of  $\text{LiCoO}_2$  crystals pressed onto a gold foil.

## The insulator-metal transition in $\text{Li}_x\text{CoO}_2$

The second aspect of this work is a study of the insulator-metal transition occurring in  $\text{Li}_x\text{CoO}_2$  for  $0.75 \leq x \leq 0.94$ . This two-phase transition has been studied by a number of researchers, and their results are briefly outlined below.

Reimers and Dahn performed an in-situ XRD study of lithium intercalation in  $\text{Li}_x\text{CoO}_2$ . They found evidence of a first-order transition for  $0.75 \leq x \leq 0.93$ , but the origin of the transition was not explained [6]. Ohzuku et al. performed XRD studies of lithium batteries and showed the presence of two phases at  $x=0.8$ : both have a hexagonal lattice, the first one with cell parameters  $a=2.82\text{\AA}$  and  $c=14.08\text{\AA}$ , the second one with  $a=2.82\text{\AA}$  and  $c=14.19 \pm 0.015\text{\AA}$  [2]. Ménétrier et al. also performed a XRD study of  $\text{Li}_x\text{CoO}_2$  samples for  $0.7 \leq x \leq 1$ , and closely examined the (003) peak [16]. The disappearance of the original peak at  $2\theta=18.98^\circ$  and the appearance of a new peak at  $2\theta=18.80^\circ$  showed the existence of a two-phase domain for  $0.75 \leq x \leq 0.94$ . They also conducted electronic measurements with a four-probe direct current method, and showed that  $\text{Li}_x\text{CoO}_2$  is metallic for  $0.50 \leq x \leq 0.74$  and semiconductor for  $x=0.98$  (Figure 4). An explanation is given for the change in conductivity: as the concentration of lithium ions  $x$  in  $\text{Li}_x\text{CoO}_2$  decreases, diamagnetic  $\text{Co}^{\text{III}}$  ions are oxidized to paramagnetic  $\text{Co}^{\text{IV}}$  ions which leads to an increase in charge carriers. The semiconductor behavior of  $\text{LiCoO}_2$  can be explained by a small departure from stoichiometry resulting in the presence of  $\text{Co}^{\text{IV}}$  ions in the initial material. Ménétrier et al. also performed a  $^7\text{Li}$  MAS NMR study which revealed the appearance of a second phase with delocalized-electron behavior upon charging. This evidence confirms that the metal-insulator transition is associated with the phase transition, and that electronic delocalization is the reason behind this phase transition. In effect, the two phases have very similar crystal structures.

First-principles calculations of phase stability in  $\text{Li}_x\text{CoO}_2$  performed by Van der Ven et al. did not reveal a two-phase region for  $x=0.75$  to  $0.94$ , which would indicate that the phase transition is not due to lithium-vacancy ordering [5]. Failure to predict the two-phase region was attributed to the local-density approximation used in the calculations.

Marianetti et al. identified the metal-insulator transition in  $\text{Li}_x\text{CoO}_2$  as a first-order Mott transition of impurities, using Density Functional Theory calculations [17]. For dilute lithium-vacancy concentrations in  $\text{Li}_x\text{CoO}_2$ , the vacancy potential binds the holes and generates an impurity band separated from the top of the valence band. The impurity band can split if the on-site correlations are strong enough, and a Mott insulator is formed. Compared to traditional doped semi-conductors,  $\text{Li}_x\text{CoO}_2$  has a particularly high mobility of the lithium ions, which lets the ions arrange into two phases at room temperature.

This work uses a variety of experimental techniques to study the insulator-metal transition: Transmission Electron Microscopy, X-ray diffraction and electrochemical impedance spectroscopy. Although this phase transition has been studied by a number of researchers, it is still unclear how this phase transition nucleates and propagates through individual crystals, and whether the metallic phase is associated with ordering.

### **Transmission Electron Microscopy:**

A number of researchers have studied the effect of charging and cycling  $\text{LiCoO}_2$  crystals by Transmission Electron Microscopy. Gabrisch et al. conducted a study of dislocations in as-prepared  $\text{LiCoO}_2$  crystals by TEM [18]. Perfect dislocations were observed on the (0001) planes and in some cases these dislocations dissociated into Shockley partial dislocations. The authors proposed that the glide of these dislocations could be responsible for the crystal structure transitions observed during de-lithiation: O3, H1-3 and O1.

Different studies approached the problem of cycling and its effect on  $\text{LiCoO}_2$  by studying individual crystals by TEM. Wang et al. prepared electrochemical cells using  $\text{LiCoO}_2$  as the active material in the positive electrode [4, 19]. These cells were cycled 50 times at a rate of C/5 and cycling was stopped at the discharged state. TEM and electron diffraction were used to study the effect of cycling on the crystals. It was found that approximately 50% of the particles showed damage, particularly lattice strain, and approximately 20% were fractured. Furthermore, the cycled particles showed signs of cation disorder between the octahedral site layers. This type of disorder creates new reflections in the

electron diffraction pattern indexed as  $(10\bar{1}0)$ . Because this disorder is localized it does not have any effect on bulk XRD measurements. Severely strained particles also showed reflections halfway between the central beam and the  $(11\bar{2}0)$  reflections. These new reflections were attributed to spinel disorder in the material. Damage to the crystals accumulates during cycling and could be a cause of capacity fade in lithium batteries.

Li et al. reported a study of commercial Sanyo lithium batteries by impedance spectroscopy, XRD, SEM and TEM [20]. The electrode materials were examined in pristine condition and after cycling at fast rate. The positive electrode active material was  $\text{LiCoO}_2$  and the authors reported the presence of damage to the crystals after cycling. This damage took the form of cracks, dislocations, as well as cation disorder in the lithium and cobalt layers. All these defects are probably caused by the stresses and strains which appear inside the particles during cycling and could contribute to capacity fade by reducing the amount of lithium available for electrochemical cycling.

Choi et al. performed a TEM study of cycled  $\text{LiCoO}_2$ , particularly nano-crystalline  $\text{LiCoO}_2$  particles [21]. They also observed cation disorder and the formation of spinel on the surface of the cycled particles. They noted that the cycle life of nano-crystalline  $\text{LiCoO}_2$  is better than that of coarse-grained  $\text{LiCoO}_2$  because of the shorter diffusion distance inside the particles.

Gabrisch, Fultz, Yazami et al. also conducted studies of cycled  $\text{LiCoO}_2$ . The authors reported that the initial O3 structure of  $\text{LiCoO}_2$  partially transforms to a cubic spinel phase on the surface of the particles during cycling [22-24]. Upon further cycling, the cubic phase spreads into the crystal. The spinel phase has a lower electrochemical activity than O3  $\text{LiCoO}_2$ , therefore this effect could be a cause of capacity fade. Also, strains are caused inside the lattice at the boundary between O3 and spinel phases, and these strains can cause damage to the particle. It was also found that storage at high voltage could cause the formation of the cubic spinel phase as well as an increased number of dislocations and strains.

Shao-Horn et al. examined  $\text{Li}_{0.5}\text{CoO}_2$  crystals by a combination of TEM and XRD [25]. The sample was prepared by charging as-prepared  $\text{LiCoO}_2$  at a very slow rate until a lithium concentration of  $x=0.5$  was reached. Therefore this sample was not cycled

repeatedly, as were those studied by other researchers. Electron diffraction showed in-plane as well as out-of-plane lithium vacancy ordering in the monoclinic crystal structure. The ordering can take place in three orientations, and several phases with different orientations can nucleate in the same crystal, creating a mazed microstructure. No evidence was found for cobalt and lithium cation disorder and spinel formation. Such phenomena are not expected to appear during the first cycle of the material. Electron diffraction patterns corresponding to the lithium vacancy ordering were found to resemble patterns for the spinel structure.

To conclude, most TEM studies of  $\text{LiCoO}_2$  have to do with particles which have been cycled repeatedly. To the best of our knowledge, no TEM study has been done on the evolution of  $\text{Li}_x\text{CoO}_2$  particles during the insulator-metal transition in the first electrochemical charge. Such a study could provide clues on how the phase transition develops inside individual crystals.

### **Electrochemical Impedance Spectroscopy:**

Electrochemical Impedance Spectroscopy probes the ionic and electronic processes occurring inside the battery, yielding information on electrolyte and electrode resistance, charge transfer resistance, ionic diffusion and capacitor effects as a function of lithium content in the positive electrode material.

A number of studies examined the AC impedance spectroscopy response of composite electrodes containing  $\text{Li}_x\text{CoO}_2$  as a function of lithium concentration or applied potential. Choi et al. performed combined XRD and EIS studies of  $\text{Li}_x\text{CoO}_2$  and  $\text{Li}_x\text{NiO}_2$  [26]. EIS tests were performed on a three-electrode cell by galvanostatically cycling the cell and measuring impedance at regular intervals. The charge rate was  $C/10$  and the frequency range was 1mHz to 100kHz. They observed high- and medium-frequency semi-circles, as well as a low frequency line inclined at  $45^\circ$ . The line was attributed to Warburg impedance, which represents lithium ions diffusion through the positive electrode. The high-frequency semi-circle remains constant with lithium content, and was attributed to particle-to-particle contact resistance and capacitance among the  $\text{LiMO}_2$  particles. The medium-frequency semi-circle was attributed to absorption of the lithium ions into the host material. The diffusivity of the lithium ions in the oxide material was around  $10^{-11} \text{ cm}^2\text{s}^{-1}$  at room temperature, and increased with decreasing lithium content. The authors attributed the variation of the lithium ion diffusivity to the fact that diffusion is facilitated when the number of vacant sites in the material increases.

Barker et al. studied  $\text{Li}_x\text{CoO}_2$  by potential step techniques and ac and dc impedance techniques [27]. They found the lithium diffusion coefficient to be in the  $10^{-9} \text{ cm}^2\text{s}^{-1}$  range. They used a two-electrode cell for their measurements and assumed that in the case of a well-prepared composite electrode, the positive electrode impedance is much smaller than that of the lithium metal electrode. They measured impedance on an as-prepared cell at  $\text{OCV}=3.1\text{V}$  and on a charged cell at  $4.2\text{V}$ . In both cases they see a high-frequency semi-circle followed by a straight line, and they attribute the semi-circle to the lithium/electrolyte interface.

Aurbach, Levi et al. studied thin  $\text{LiCoO}_2$  composite electrodes by slow scan rate cyclic voltammetry (SSCV), potentiostatic intermittent titration technique (PITT) and electrochemical impedance spectroscopy [28, 29]. They found that the electroanalytical behavior of  $\text{Li}_x\text{CoO}_2$  behavior is similar to that of other transition metal oxide and graphite electrodes. They performed EIS measurements on cells at different potentials. In the impedance spectra, they identified a high-frequency semi-circle, a medium-frequency semi-circle, a Warburg impedance region followed by a steep line at low frequencies. The high-frequency semi-circle was attributed to surface film phenomena. This high-frequency semi-circle is potential-independent and is similar to surface film-related semi-circles measured for other types of electrodes. FTIR measurements showed that as-prepared  $\text{LiCoO}_2$  was covered with a  $\text{Li}_2\text{CO}_3$  surface film, probably due to the reaction between that  $\text{LiCoO}_2$  and  $\text{CO}_2$  in ambient air. Next, they attributed the medium-frequency semi-circle to the charge-transfer resistance associated to the slow interfacial transfer of lithium ions, and to the double-layer capacitance corresponding to the interface between the surface film and the oxide. This semi-circle was strongly potential-dependent, and the decrease of the charge transfer resistance during lithium de-intercalation could be partially related to the increase of the oxide electronic conductivity. Lastly, the Warburg impedance is related to diffusion of lithium ions in the bulk of the oxide, and the low-frequency capacitance was attributed to the accumulation of lithium ions into the bulk of the oxide. Figure 5 shows the equivalent circuit proposed by Levi et al. to model the electroanalytical behavior of  $\text{Li}_x\text{CoO}_2$  electrodes.

Nobili et al. performed AC impedance studies on  $\text{Li}_x\text{CoO}_2$  composite electrodes at different temperatures [30]. They characterized the impedance spectra by a high-frequency semi-circle attributed to the presence of a surface-layer, a medium-frequency semi-circle associated with charge-transfer, a low-frequency semi-circle corresponding to the electronic properties of the oxide, and a low-frequency line associated with ionic diffusion. The second semi-circle appeared as lithium ions are de-intercalated from the positive electrode. The low-frequency semi-circle was attributed to the electronic properties of the material because the resistance associated with it varied in the potential range corresponding to the insulator-metal transition. The capacitance associated with it,



$C_e$ , was attributed to the roughness of the electrodes. Figure 7 shows two equivalent circuits proposed by the authors. Both models gave three semi-circles in the impedance spectra and the authors could not distinguish between them.

In order to distinguish the impedance characteristics of  $\text{Li}_x\text{CoO}_2$  from the binder and carbon additives present in composite electrodes, Dokko et al. examined  $\text{LiCoO}_2$  single particles by AC impedance spectroscopy and potential step methods [31]. These single-particles are 5-20 $\mu\text{m}$  large and are agglomerations of single-crystals. The Nyquist plots show a high-frequency semi-circle, which was attributed to charge-transfer resistance and double-layer capacitance, a Warburg impedance region, and a capacitive behavior at low frequencies. Figure 6 shows the equivalent circuit proposed by Dokko et al. to model the behavior of  $\text{Li}_x\text{CoO}_2$  single-particles. Their findings are similar to those of Levi, Aurbach, et al. except for the fact that they did not observe a second semi-circle in the impedance data. They also conducted tests on composite electrodes and observed two semi-circles. They attributed the second semi-circle to the porous structure of composite electrodes containing carbon additives and binder.

In further impedance studies, Levi et al. addressed the issue of the presence of a second semi-circle in impedance spectra of composite electrodes, and its absence for single particles [32]. They proposed a model taking into account the structure of composite electrodes. The model used a non-homogeneous and layered distribution of the oxide material and finite values for the resistance of the oxide bulk and the electrolyte present in the pores of the electrode. They showed that the second semi-circle is due to the intercalation capacity of the thin parts of the electrodes working in parallel with the highly resistant thick parts of the electrode.

To conclude, different studies have attributed the features seen in AC impedance spectra of  $\text{Li}_x\text{CoO}_2$  to a surface layer effect, a charge transfer resistance coupled with a double-layer capacitance, the electronic resistance of the positive electrode material, and ionic diffusion represented by a Warburg impedance. It is particularly interesting to perform electrochemical impedance spectroscopy measurements in the range of lithium concentrations that correspond to the metal-insulator phase transition because

information can be obtained on the evolution of the electronic conductivity of the positive electrode as a function of lithium content.

This study draws information from a variety of experimental techniques (AFM, TEM, EIS) to probe the evolution of individual  $\text{Li}_x\text{CoO}_2$  crystals as a function of lithium content. Such information as can be obtained from this study can provide clues on the reasons behind capacity fade and maybe help engineer new positive electrodes materials with better electrochemical properties.

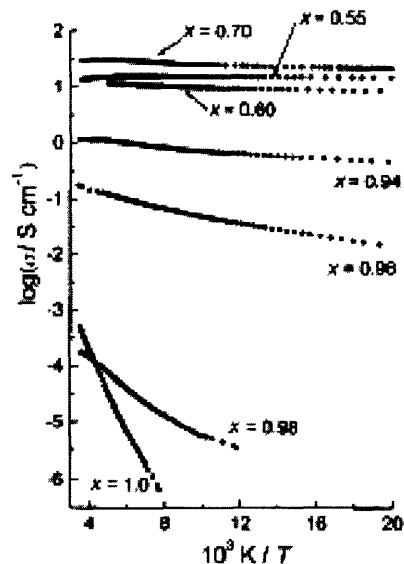


Figure 4: Evolution of the electrical conductivity of  $\text{Li}_x\text{CoO}_2$  as a function of reciprocal temperature for various lithium concentrations  $x$  [16].

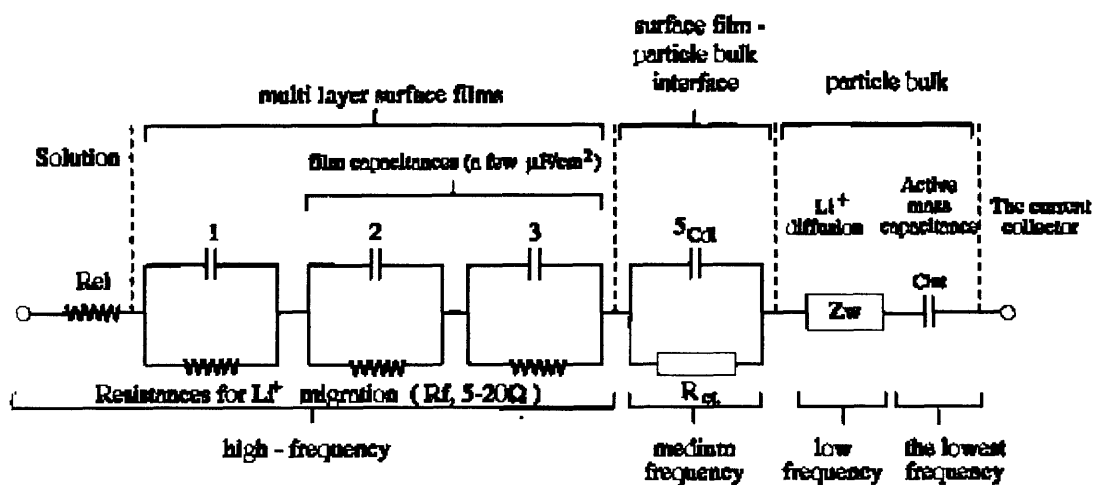


Figure 5: Equivalent circuit proposed by Levi et al. to model the electroanalytical behavior of  $\text{Li}_x\text{CoO}_2$  electrodes [29].

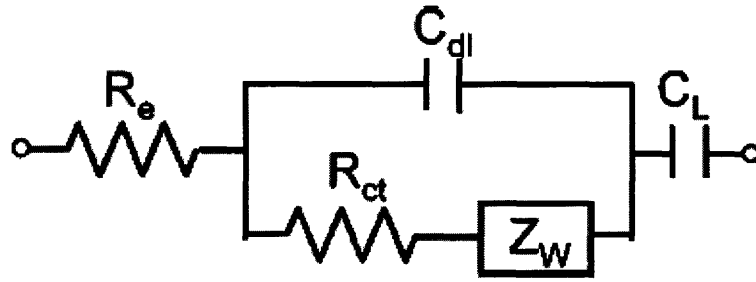


Figure 6: Equivalent circuit proposed by Dokko et al. to model the electroanalytical behavior of  $\text{Li}_x\text{CoO}_2$  single-particles [31].

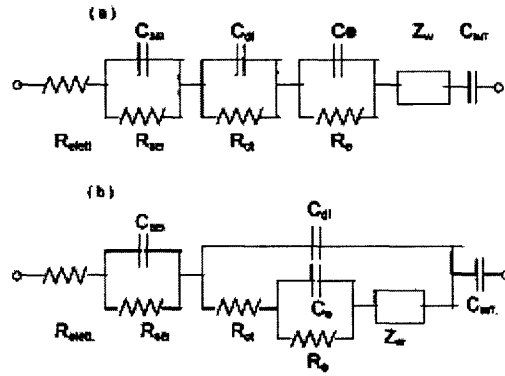


Figure 7: Equivalent circuits proposed by Nobili et al. to model the electroanalytical behavior of  $\text{Li}_x\text{CoO}_2$  composite electrodes. Circuit (a) is inspired by Levi et al. while circuit (b) is inspired by Bruce et al. [30].

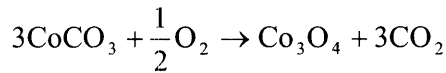
# 1 Synthesis and characterization of the LiCoO<sub>2</sub> parent sample

In order to study the effect of charging on LiCoO<sub>2</sub> crystals, samples were prepared by solid-state synthesis. The stoichiometry of LiCoO<sub>2</sub> samples was verified by X-ray diffraction and electrochemical testing. The following paragraphs will describe synthesis methods and results.

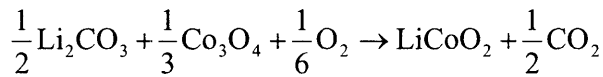
## 1.1 Solid-state synthesis of LiCoO<sub>2</sub>

LiCoO<sub>2</sub> samples were prepared by solid-state synthesis from carbonate precursors:

Co<sub>3</sub>O<sub>4</sub> was synthesized from CoCO<sub>3</sub> (Alfa Aesar) at 400°C in air for 24 hours with intermediate grinding. Heating and cooling rates were 2° per minute. Solid state-synthesis of Co<sub>3</sub>O<sub>4</sub> takes place according to the following reaction:



LiCoO<sub>2</sub> was synthesized from the resulting Co<sub>3</sub>O<sub>4</sub> and Li<sub>2</sub>CO<sub>3</sub> (Alfa Aesar Puratronic) for 12 hours at 600°C and 24 hours at 900°C in air with intermediate grinding. Heating and cooling rates were 2° per minute. Solid state-synthesis of LiCoO<sub>2</sub> takes place according to the following reaction:



Different ratios of Li<sub>2</sub>CO<sub>3</sub> to Co<sub>3</sub>O<sub>4</sub> were tested, and it was found that a ratio of Li:CO of 0.96:1 lead to a stoichiometric sample of LiCoO<sub>2</sub>.

## 1.2 Preparation of composite electrodes and coin cells

For electrochemical testing, composite electrodes were prepared with LiCoO<sub>2</sub> powder and placed in cells. First, 80% weight LiCoO<sub>2</sub> powder, 10% weight Super P Carbon (MMM Carbon) and 10% weight PVDF (polyvinylidene difluoride) were thoroughly mixed by manual grinding, and made into a slurry by adding NMP (1-Methyl-2-pyrrolidinone, EMD). The slurry was spread on aluminum foil and vacuum dried. The electrode thickness is approximately 80µm, of which 20µm is the thickness of the foil.

Electrodes were cut and placed in 2016 coin cells with lithium metal as the counter electrode and 1M  $\text{LiPF}_6$  in DMC:EC (1:1) electrolyte (Merck). Cellgard 2500 microporous polypropylene membranes were used as separator. Coin cells were prepared in a Vacuum Atmospheres glovebox, with oxygen and moisture contents inferior to 1ppm. Coin cells were allowed to rest overnight in the glovebox before testing, in order to let the electrolyte permeate through the separator.

### **1.3 Characterization of the parent sample**

The  $\text{LiCoO}_2$  sample was characterized by X-ray diffraction and electrochemical testing. X-ray diffraction studies of  $\text{LiCoO}_2$  samples were performed with a Rigaku RU300 powder diffractometer, using copper  $K\alpha$  radiation. X-ray diffraction data were collected in theta two-theta reflection mode, at  $2^\circ$  per minute scan rate, between  $10^\circ$  and  $90^\circ$ . The cell parameters were refined using commercial software Jade. Figure 8 shows the XRD pattern of the  $\text{LiCoO}_2$  parent sample. Figure 9 shows a close-up of this pattern, and does not reveal any impurity peaks. The cell parameters were refined using the software Jade, and were found to be:  $a=2.813\pm0.001\text{\AA}$  and  $c=14.030\pm0.006\text{\AA}$ .

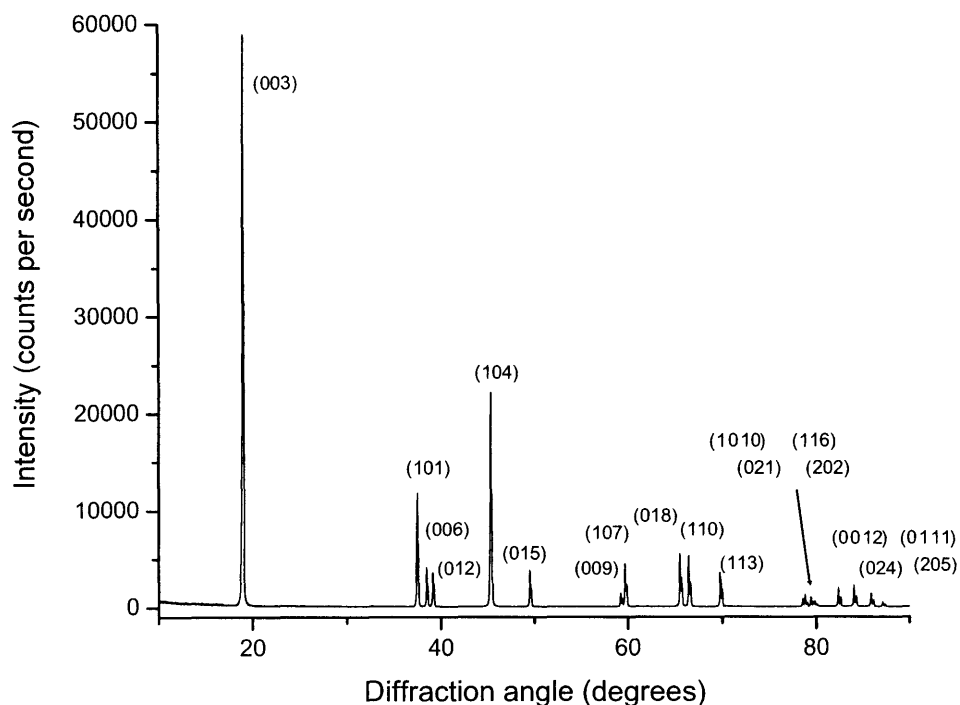


**Figure 8: XRD pattern of  $\text{LiCoO}_2$ , measured with a Rigaku RU300 powder diffractometer, using copper  $K\alpha$  radiation. X-ray diffraction data was collected in theta-two theta reflection mode, at  $2^\circ$  per minute scan rate, between  $10^\circ$  and  $90^\circ$ .  $\text{LiCoO}_2$  was synthesized from  $\text{Li}_2\text{CO}_3$  and  $\text{Co}_3\text{O}_4$  in air at  $600^\circ\text{C}$  for 12 hours and at  $900^\circ\text{C}$  for 24 hours.**

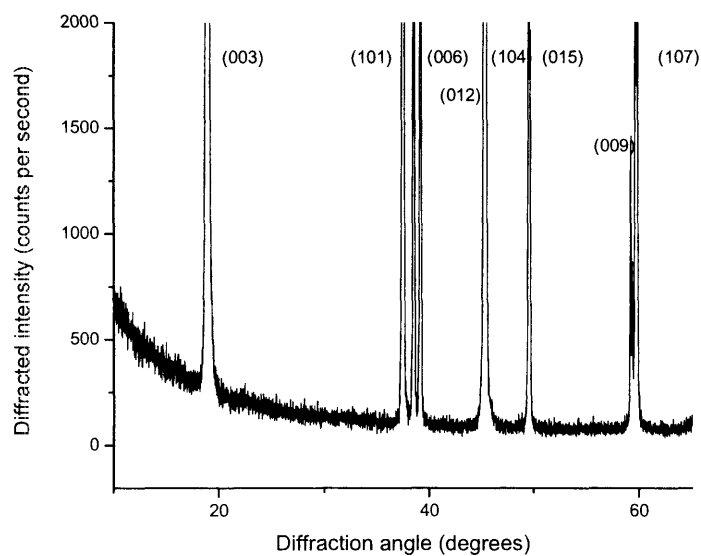


**Figure 9: Close-up of the XRD pattern of  $\text{LiCoO}_2$ , on the  $15^\circ$ -  $62^\circ$  range.**

Electrochemical testing was conducted by galvanostatically cycling the coin cells at a rate of C/50 with a Solartron 1470 Battery Tester. A cut-off voltage of 4.5V was used. Figure 10 shows the cell voltage as a function of lithium content  $x$ , for coin cell 083004b\_11 prepared with a  $\text{LiCoO}_2$  composite electrode. The galvanostatic charge profile shows a feature at approximately  $x=0.5$ , characteristic of stoichiometric  $\text{LiCoO}_2$ .

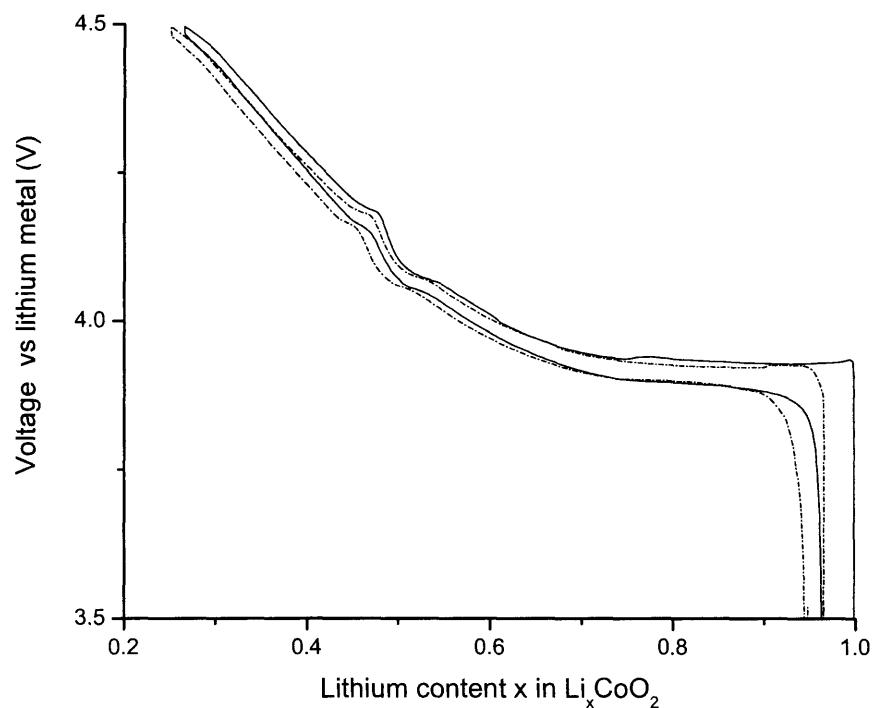


**Figure 10: Electrochemical cycling of a  $\text{LiCoO}_2$  positive electrode vs. lithium metal. The first cycle corresponds to the full line and the second cycle to the dotted line. The coin cell was cycled at a rate of C/50 (theoretical full charge in 50 hours) using a Solartron 1470 Battery Tester. The applied current was equal to 5.48mA/g of active material.**



## **2 A study of the morphological evolution of individual LiCoO<sub>2</sub> crystals during cycling by AFM**

### **2.1 Experimental**

#### **2.1.1 Preparation and characterization of gold and crystals electrodes**

For AFM imaging, electrodes were prepared by dispersing LiCoO<sub>2</sub> crystals on a gold foil disk (Scientific Instruments) and pressing them into the gold. The gold foil acts as a physical support for the crystals, as well as a current collector. The advantage of this setup is that there are no carbon additives and binder, therefore the intrinsic properties of LiCoO<sub>2</sub> are studied. The crystals were suspended in acetone and dropped on the gold foil before pressing, in order to achieve a good dispersion of crystals on the gold. Then the crystals were pressed between two gold foil disks at 15,000 psi using a Carver hydraulic press. Scanning Electron Microscope images of the electrodes showed that the crystals were generally well dispersed on the gold (Figure 11). The crystals are slightly embedded into the gold and indentations left by previous crystals can be seen in the gold foil. A very small number of crystals show cracks, probably due to the application of pressure to embed the crystals into the foil (Figure 15).

The gold foil was reused for different experiments. After each experiment, the crystals were dissolved in hydrochloric acid (Mallinkrodt), and the foil was rinsed in deionized water. Finally the foil was pressed flat again, but some indentations remain.

The amount of active material on the gold foil was determined by weighing. This technique yields an approximate value of the weight of the crystals, the accuracy of the balance being of the same order of magnitude as the weight of the crystals.

Gold was chosen because it should be inert in the electrochemical cell. The electrochemical properties of the gold foil vs. lithium metal were studied using a coin cell containing gold foil as the positive electrode, lithium metal as the negative electrode and 1M LiPF<sub>6</sub> in DMC:EC (1:1) electrolyte (Merck). Two Cellgard 2500 microporous polypropylene membranes were used as separator. Cyclic voltammetry data from this

coin cell was collected by Sundeep Kumar on a Solartron 1470 Battery Tester. (Figure 12) The rate was 5.5mV/s for the first cycle and 1.8mV/sec for the second and third cycles. Data was collected on two identical coin cells and the results were reproducible. The cyclic voltammograms corresponding to the first, second and third cycles of the cell do not show any peaks between 2.5V and 4.5V, indicating that gold foil is electrochemically stable against lithium metal in that voltage window. The peak around 4.5V on the first cycle may be associated with the formation of a surface film on the fresh gold surface and the peak around 5V corresponds to the decomposition of electrolyte. In the second and third cycles, the peak around 4.5V disappears because the fresh gold surface is already covered with a passive layer.

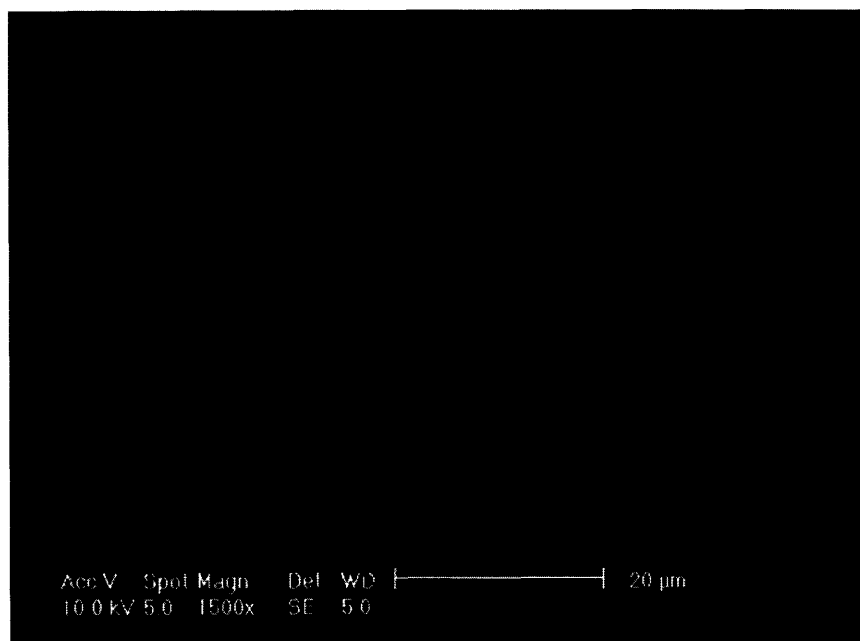


**Figure 11: SEM image of a gold foil with  $\text{LiCoO}_2$  crystals pressed onto it. The  $\text{LiCoO}_2$  crystals are distributed evenly on the surface and lie flat on the foil. Indentations left by other crystals can also be seen on the foil (indicated by arrows).**

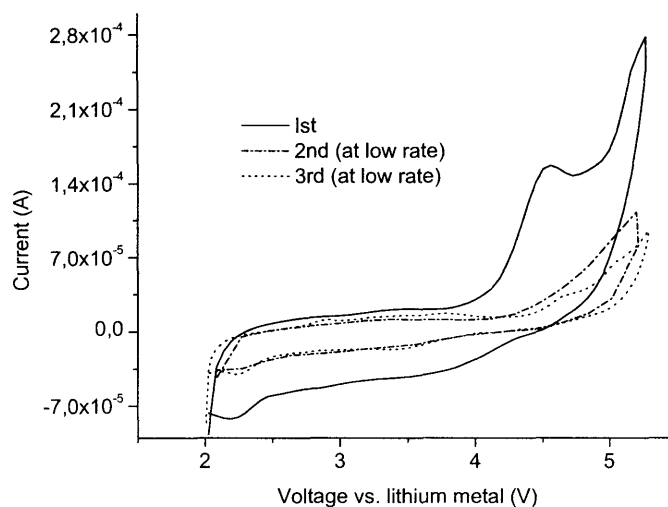


**Figure 12: Cyclic voltammetry curve of a coin cell containing lithium metal as the negative electrode, gold foil as the positive electrode, and  $\text{LiPF}_6$  in EC:DMC (1:1) as the electrolyte. Cellgard 2500 microporous polypropylene membranes were used as separator. In the 2.5-4.5V interval, the cycles do not exhibit any feature, indicating that lithium does not react with gold at those potentials.**

### 2.1.2 AFM imaging

AFM imaging was conducted with a Veeco Instruments Enviroscope coupled with a Nanoscope IIIa controller and a Nanoscope EC Bipotentiostat. AFM imaging was done in Contact Mode with silicon nitride and silicon probes, in-situ and ex-situ.

For in-situ imaging, an open cell was prepared and placed inside the sample enclosure of the Enviroscope. The open cell was set up in the sample stage provided by Veeco instruments for in-situ imaging. Cell assembly was conducted inside a Vacuum Atmospheres glovebox, with oxygen and moisture contents inferior to 1ppm.  $\text{LiCoO}_2$  crystals pressed onto a gold foil served as the working electrode and lithium metal wires served as the counter and reference electrodes. The counter lithium electrode was given a circular shape in order to ensure homogeneous current distribution inside the cell. In some cases, the lithium electrodes were connected directly to the screws on the sample stage, and in other cases copper wire was used to connect the lithium electrodes to the screws. The lithium electrodes are made by rolling up thin strips of lithium foil in order to make lithium wires stiff enough to manipulate. It was noticed that electrolyte could rise inside these electrodes by capillary effect, reach the screws and affect the electrochemical measures. For this reason, copper wires were used to avoid capillary effect.

Figure 13 is a diagram of the cell setup. Figure 14 shows pictures of assembled cells. After assembly, the electrochemical cell was transferred to the Enviroscope in an air-tight container. The Enviroscope sample enclosure is air-tight and all the imaging was done in flowing dry argon (Airgas, Inc.). The sample enclosure was purged with Argon before insertion of the sample. However, exposure to air could not be avoided during transfer of the sample into the microscope. Efforts were taken to keep the exposure time as short as possible. The 1M  $\text{LiPF}_6$  in DMC:EC (1:1) electrolyte was added later and kept inside the glovebox until required. Adding the electrolyte to the electrochemical cell inside the Enviroscope also requires opening the sample enclosure. In order to avoid unnecessary exposure to air, the enclosure was opened as shortly as possible, and a positive pressure of Argon was maintained.

In typical AFM experiments, the topography of  $\text{LiCoO}_2$  crystals pressed onto the gold foil was first imaged ex-situ, then the electrolyte was added and the topography was measured again in-situ. Once an interesting imaging area was located, a current was applied to the cell in order to charge it galvanostatically and the same area was imaged continuously while the cell voltage was monitored. Typically, charge rates of  $C/2$  or  $C/4$  were used, which means that in theory all of the  $\text{LiCoO}_2$  would be charged in two or four hours. When possible the cell was charged for one hour to a lithium concentration of  $x=0.5$ , then discharged back to  $x=1$ . However, the value of lithium concentration is approximate because the weight of the active material on the gold foil is not determined accurately.

It must be stressed that such in-situ AFM experiments are very difficult to run because of the sensitivity of the cell components.

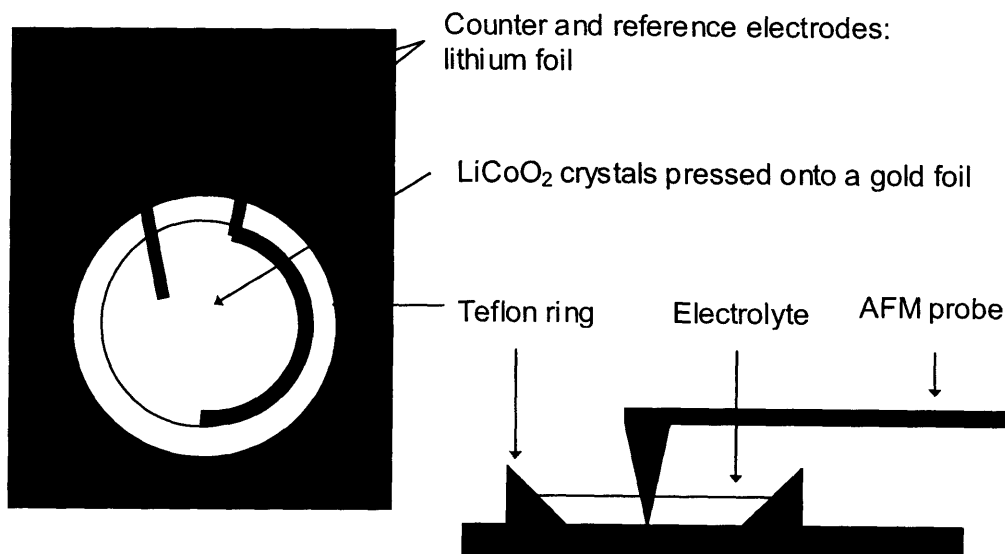


Figure 13: Top view and side view of the AFM sample stage with in-situ electrochemical cell.

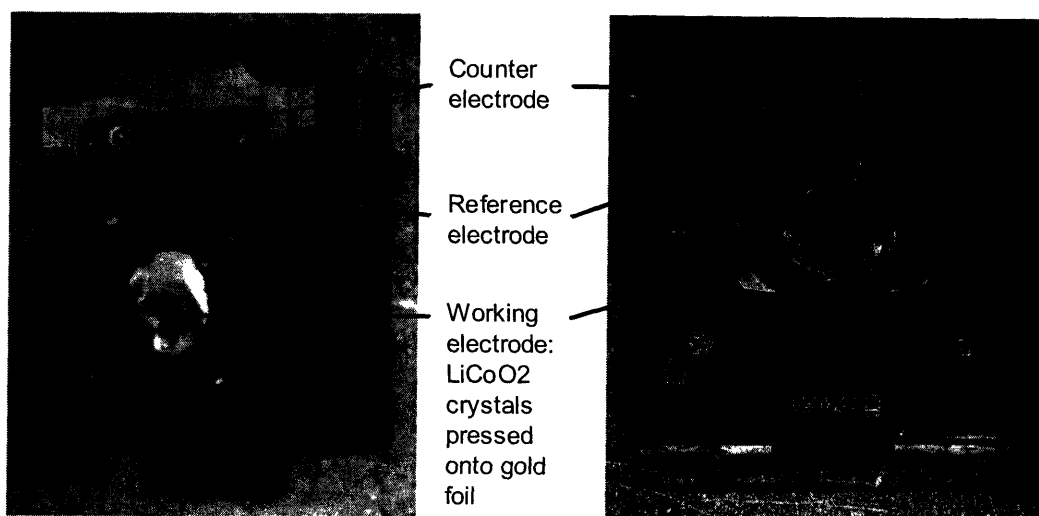


Figure 14: Pictures of the AFM cell setup. An open battery is assembled inside the sample holder provided by Veeco Instruments. The positive electrode (LiCoO<sub>2</sub> crystals pressed onto a gold foil) is placed at the center of the holder and clamped under a Teflon ring. The counter and reference electrodes are made from lithium foil and are supported by a groove in the Teflon ring. In some experiments, the lithium electrodes were connected directly to the two screws. In other experiments, a copper wire was used as current collector between the screws and the foil. The counter electrode is made circular to ensure homogeneous current distribution. Black insulating tape is used to hold the cell in place on the sample stage, and to avoid shorting the cell. Later in the experiment, electrolyte is poured into the Teflon ring.

## 2.2 Results and discussion

### 2.2.1 Objectives

To the best of our knowledge, this work is the first study to examine the effect of charging on the morphology of individual  $\text{LiCoO}_2$  crystals. The crystals can be imaged by Atomic Force Microscopy in-situ as the cell is being charged or discharged.

$\text{Li}_x\text{CoO}_2$  is a layered material consisting of alternating of lithium and cobalt planes stacked between oxygen planes. When the battery is charged, lithium ions de-intercalate out of the lithium planes and into the electrolyte. Electrostatic forces exist between neighboring oxygen planes, and when the lithium ions are removed from between these planes, these forces push the oxygen planes away from each other. When the battery is discharged, the process is reversed and the lithium ions intercalate back into the lithium. Therefore the crystal structure changes during charge and discharge, and these changes appear first at the edges of the lithium planes. In AFM experiments, steps at the edges of the crystals are imaged repeatedly as lithium de-intercalates and intercalates into the material.

Furthermore, it is expected that the large flat areas of the crystals correspond to the crystallographic (003) plane, which is the orientation of the lithium planes. In general, crystals dispersed onto the gold foil should fall flat, and it is assumed that the large flat surfaces at the top of the crystals imaged by AFM correspond to the (003) plane. When a crystal exhibited growth steps on its edges, they were studied. The evolution of the step height was studied, as well as the roughness of the crystal surface in order to detect surface layers.

First, the general morphology of crystals imaged in AFM will be discussed. Then, the evolution of crystal morphology during cycling will be described and hypotheses will be given to explain the observed behavior.

### 2.2.2 General crystal morphology and tip shape effects

Figure 15 and Figure 16 are Scanning Electron Microscope Images of  $\text{LiCoO}_2$  crystals pressed onto a gold foil. In general, crystals have a plate-like shape and lie flat on the gold foil. The crystal size varies between 1 and  $15\mu\text{m}$ , and the thickness is on the order of  $2\mu\text{m}$ . Some crystals have sharp edges and growth steps on the sides, parallel to the basal plane. Other crystals have more rounded shapes, which could be an indication that the sample is slightly overstoichiometric in lithium.

Figure 17 is a three-dimensional image of a typical AFM scan showing a  $\text{LiCoO}_2$  crystal embedded in gold foil. Most crystals imaged in AFM have this type of morphology. This image has similarities as well as differences with the SEM images of similar crystals. The top surface of the crystal and the gold foil seem to be imaged in the same manner as by SEM, however the edges of the crystal appear to be slanted. In AFM images, the slant angle depends on the direction of the edge. Conversely, SEM images of similar crystals show that the crystals have steep edges. Figure 18 shows a three-dimensional image of an AFM scan showing  $\text{LiCoO}_2$  crystals dispersed on a gold foil. The slant of the crystals edges seem to all be oriented in similar directions. Therefore this discrepancy between AFM and SEM images must arise from an imaging artifact, most likely the effect of the AFM tip shape. It is expected that the SEM images give a correct representation of the crystal morphology, and that the AFM images are distorted. The image collected by the Atomic Force Microscope is in effect a convolution of the shape of the tip and of the shape of the sample.

All experiments were conducted in Contact Mode, in which a tip scans along the surface of the sample to detect morphology. In most experiments, silicon nitride probes were used in AFM imaging. These probes were NP probes purchased from Veeco Instruments.

The tips are pyramid-shaped and have the following characteristics:

tip height :  $2.5 - 3.5\ \mu\text{m}$

front angle :  $35^\circ \pm 2^\circ$

back angle :  $35^\circ \pm 2^\circ$

side angle :  $35^\circ \pm 2^\circ$

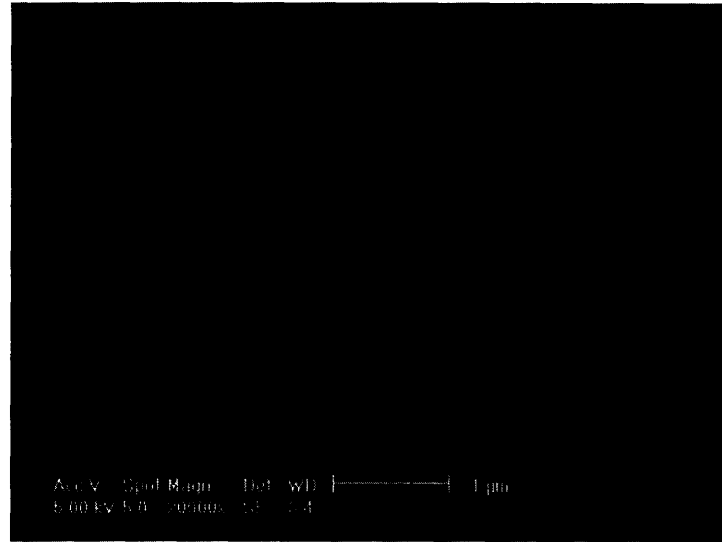
tip radius of curvature: 20 nm



Figure 19 shows a schematic of a silicon nitride probe. The probe is mounted on the tip holder with a  $10.5^\circ$  angle. Therefore, the front angle of the tip is approximately  $45^\circ$  and the back angle is  $25^\circ$ . Figure 20 is a schematic of the effect of the tip shape on the height profile measured by AFM. As the probe scans the surface of the sample, the tip side walls can hit a crystal even though the tip end is touching the gold. Therefore this type of tip cannot measure steep inclines with angles larger than  $65^\circ$  in the front,  $45^\circ$  in the back, and  $55^\circ$  on either side. The resulting AFM image shows that the crystal has slanted side walls, although the real crystal has steep sidewalls.

Tips with a higher aspect ratio also exist and could enable the imaging of steep surfaces. However, these probes are made from etched silicon, and wear out faster than the silicon nitride probes during repeated scanning. Furthermore, high aspect ratio probes generally have a very high spring constant. These stiff probes push the crystals off the gold foil instead of imaging the crystals. Different types of tips (RTESP, SCM-PIC, SCM-PIT from Veeco Instruments) were experimented with, but none was found to image the sample properly.

Although the use of silicon nitride NP tips introduces some imaging artifacts, most of the crystal features are rendered accurately, and AFM is a unique way of studying the evolution of crystal morphology on the nanometer scale during cycling in a battery. The top surface of the crystal as well as the surface of the gold foil are imaged accurately and can give information on the existence of surface layers. Furthermore, some crystals exhibit some growth steps parallel to the basal plane. If those steps are not too steep, they can be imaged and give information on the evolution of the crystal shape during cycling.



**Figure 15: SEM image of a  $\text{LiCoO}_2$  crystal pressed on a gold foil. The crystal is cracked in the middle, probably due to the application of pressure to embed the crystals in gold. Very few crystals exhibit such cracks. This crystal has the typical plate-like shape of  $\text{LiCoO}_2$  crystals; the flat surface on the top of the crystal most probably corresponds to the (003) plane orientation. The crystal shows two types of growth steps which are often seen on  $\text{LiCoO}_2$  crystals: steps parallel to the basal plane, and steps in the orthogonal direction. The shape of the crystal is slightly rounded, which could be a sign that the sample is slightly overstoichiometric in lithium.**

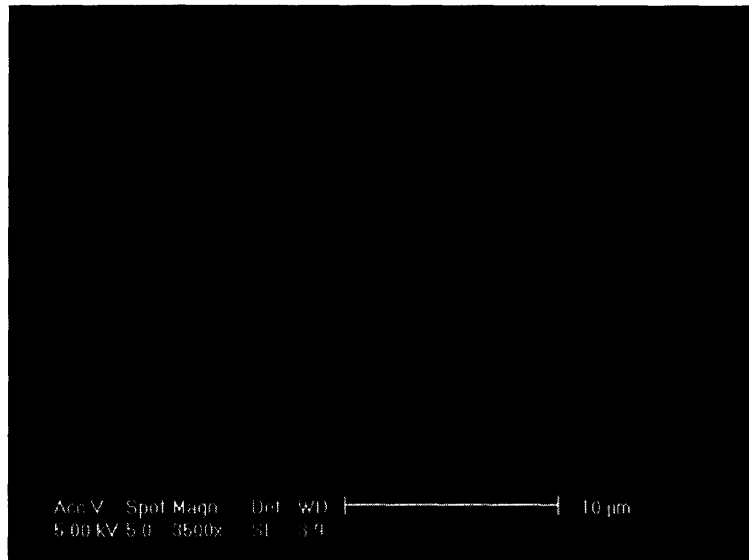


**Figure 16: SEM image of  $\text{LiCoO}_2$  crystals dispersed on a gold foil. Most of the crystals lie flat on the foil. Some crystals have clear growth steps on the edges, others are more rounded.**

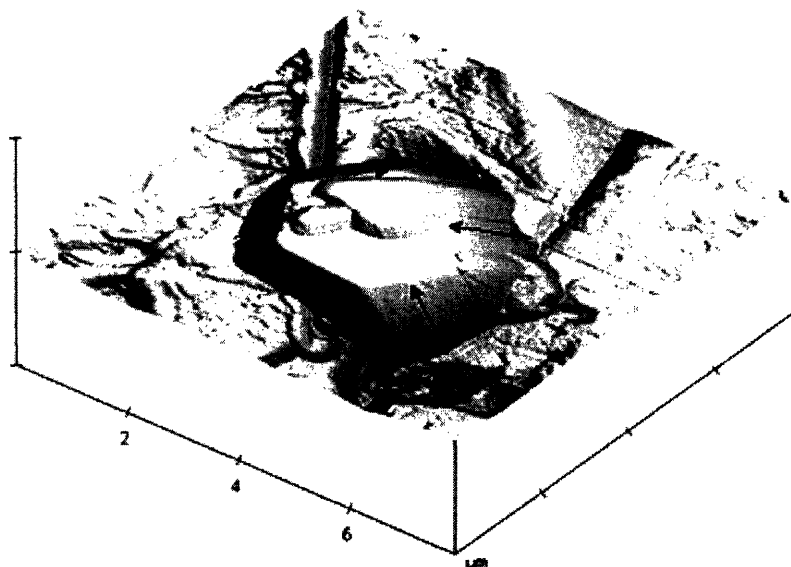


**Figure 17: 3D image of a typical AFM scan of a LiCoO<sub>2</sub> crystal. The scan is 7.843 μm x 7.843 μm x 7.843 μm. The sides of the crystal are slanted, with different angles in different directions. The arrows indicate the slant angle.**

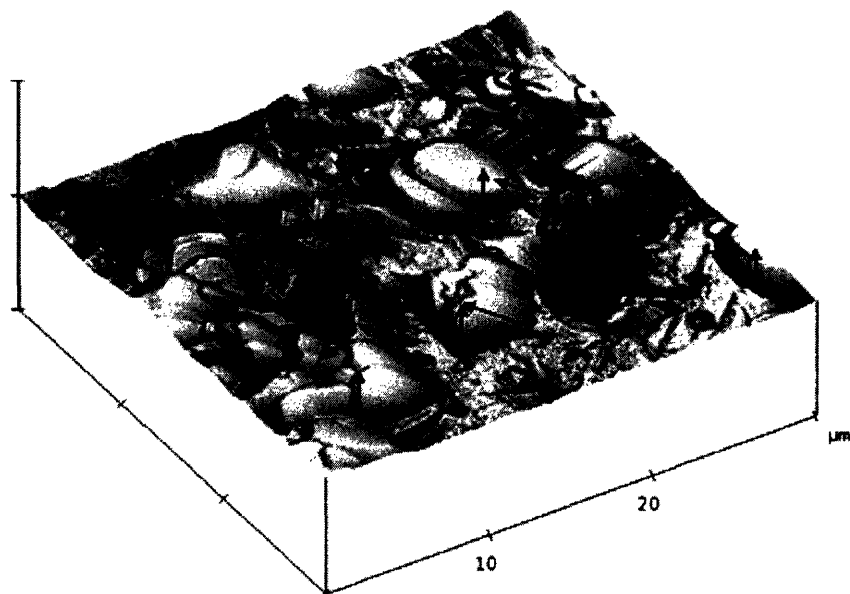


**Figure 18: 3D image of an AFM scan showing LiCoO<sub>2</sub> crystals dispersed on a gold foil. Most of the crystals have slanted sides, and the all the crystals seem to be slanted in the same direction. The arrows indicate the slant angle. The discrepancy between the AFM images of the crystals and the SEM images of similar crystals arises from the convolution of the tip shape with the sample morphology in AFM imaging.**

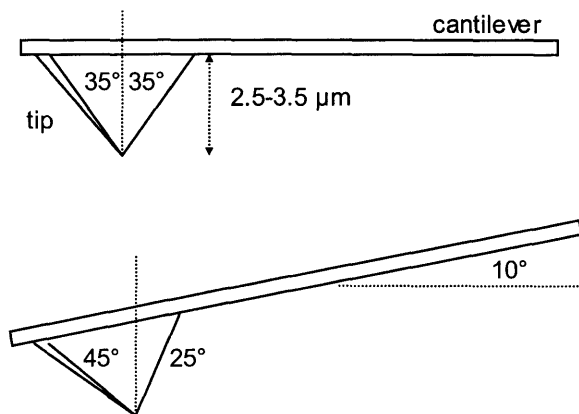


**Figure 19: Characteristics of the silicon nitride probes used in Contact Mode AFM imaging. The probes are NP probes from Veeco Instruments. The tip has a pyramidal shape and is mounted on a cantilever. The front, back and side angles of the tip are approximately 35°. The tip mounting angle is 10.5°, therefore in effect the front angle of the tip is approximately 45° and the back angle is 25°.**

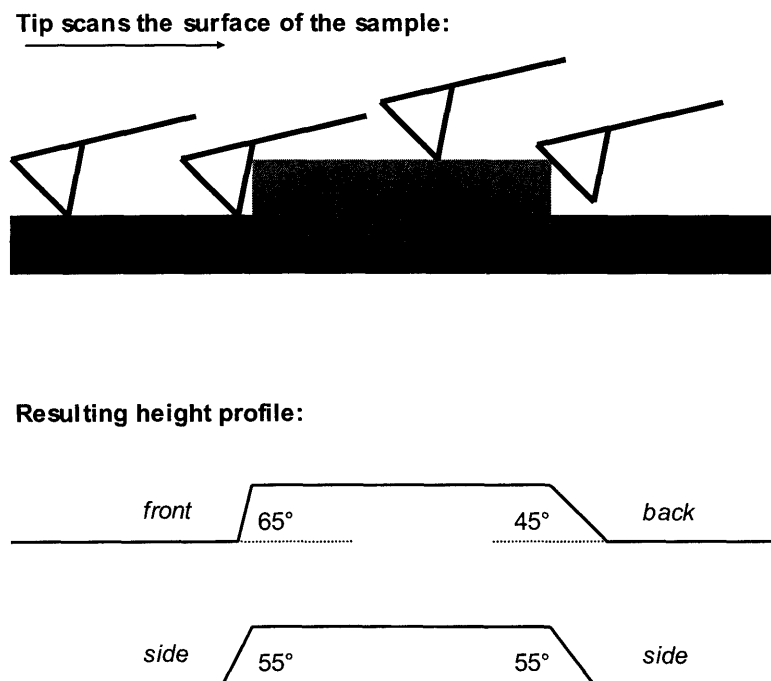
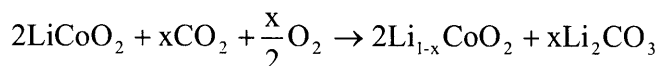


**Figure 20: Schematic showing the effect of tip shape on the height profile measured by AFM. As the tip scans the surface of the sample, the tip side walls can hit a crystal even though the tip end is on the gold foil. Therefore this type of tip cannot measure steep inclines accurately.**

### 2.2.3 Surface features on the crystals

Most of the crystals have rounded bumps on their surface. Figure 21 is a three-dimensional representation of LiCoO<sub>2</sub> crystals imaged by AFM in flowing dry argon, in the absence of electrolyte. There are round bumps on the top surface of the crystal, and similar bumps are seen on most LiCoO<sub>2</sub> crystals. Figure 22 shows a close-up view of some of these bumps. Some of the bumps have similar shapes. This is very probably an imaging artifact due to the shape of the probe tip. The bumps are 50-250 nm in diameter and 5-15 nm in height.

These bumps could be due to an impurity phase of Li<sub>2</sub>CO<sub>3</sub> present in the as-prepared LiCoO<sub>2</sub> sample. Other researchers have reported the presence of Li<sub>2</sub>CO<sub>3</sub> on the surface of as-prepared transition metal oxide crystals. [29] It is believed that Li<sub>2</sub>CO<sub>3</sub> forms as the transition metal oxide reacts with CO<sub>2</sub> present in air during storage, according to the following reaction:



The X-ray diffraction pattern recorded on our LiCoO<sub>2</sub> sample after 6 months storage in air shows the presence of Li<sub>2</sub>CO<sub>3</sub>. (Figure 23)

FT-IR data was also collected from a Li<sub>2</sub>CO<sub>3</sub> sample and the LiCoO<sub>2</sub> sample used in the experiments by Timothy McClure and Sundeep Kumar. Figure 24 shows the two spectra. The data was collected in transmittance mode on a Thermo Nicolet Magna 860 (USA), from a pellet containing approximately 95% of KBr and 5% of Li<sub>2</sub>CO<sub>3</sub> or LiCoO<sub>2</sub>. The Li<sub>2</sub>CO<sub>3</sub> spectrum shows two main peaks: a broad peak at around 1450cm<sup>-1</sup> attributed to the C-O asymmetric and symmetric stretching modes of Li<sub>2</sub>CO<sub>3</sub>, and a sharp peak at 870cm<sup>-1</sup> associated with the CO<sub>3</sub> bending mode. [33] The sharp peak at 870cm<sup>-1</sup> is also seen in the LiCoO<sub>2</sub> spectrum, indicating the presence of Li<sub>2</sub>CO<sub>3</sub> on the surface of LiCoO<sub>2</sub> crystals.

To conclude, the surface features observed on Li<sub>x</sub>CoO<sub>2</sub> crystals in AFM are most probably Li<sub>2</sub>CO<sub>3</sub> impurities.

In most experiments, the bumps initially present on the surface of the crystals seem to disappear gradually during the in-situ experiment, whether or not an electric current is applied. Figure 25 shows images of the same area on the side of a crystal, imaged by AFM at the beginning of the experiment, after 15 min, and after one hour. The imaging was done in electrolyte but no electric current was applied. The bumps initially present on the crystal almost fade away completely over the course of one hour. Therefore, it seems that  $\text{Li}_2\text{CO}_3$  impurities dissolve into the electrolyte.

### **Roughness of the crystal surface:**

Table 1 shows roughness measurements of the surface of  $\text{Li}_x\text{CoO}_2$  crystals during in-situ AFM imaging. The roughness measurements were done using the Nanoscope software. The roughness of the crystal surface is on the order of 1 to 5nm, and decreases as the crystal is imaged in-situ. The decrease in roughness is probably due decrease of the  $\text{Li}_2\text{CO}_3$  surface layer. The roughness of the crystal is small, and should not affect how the heights of crystal step are measured, as the images steps are several hundred of nanometers high. Furthermore, the step heights are measured by averaging neighboring scan lines, partially removing the effect of surface roughness on the height profile.

**Table 1: Roughness measurements of the surface of  $\text{Li}_x\text{CoO}_2$  crystals during in-situ AFM imaging.**

	Roughness (nm)	
	Experiment 042505	Experiment 050905
After adding electrolyte	4.29	2.8
At the beginning of charge	3.53	2.12
At the end of charge	2.83	1.90
At the end of discharge	2.67	1.23

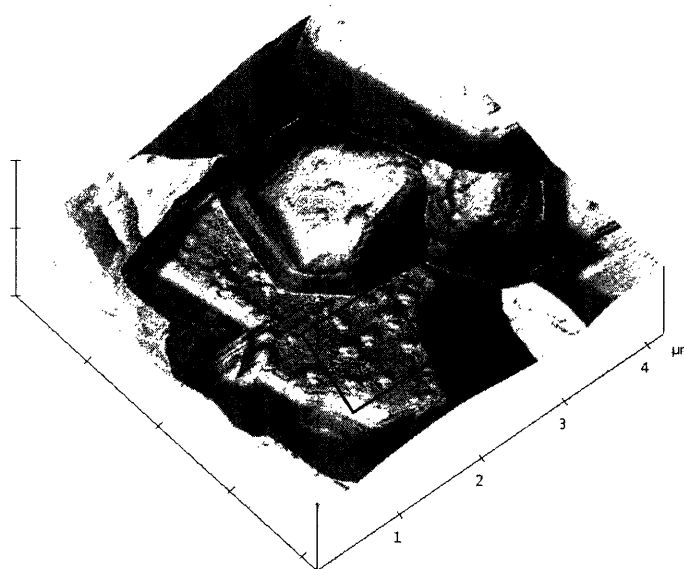


**Figure 21: 3D image of an AFM scan showing LiCoO<sub>2</sub> crystals. The scan size is 4.185 μm. This scan was performed in argon, in the absence of electrolyte. There are rounded bumps on the surface of the crystals and similar bumps are seen on most LiCoO<sub>2</sub> crystals. The bumps are 50-250 nm in diameter and 5-15 nm in height. The black square indicates where a close-up scan was performed.**

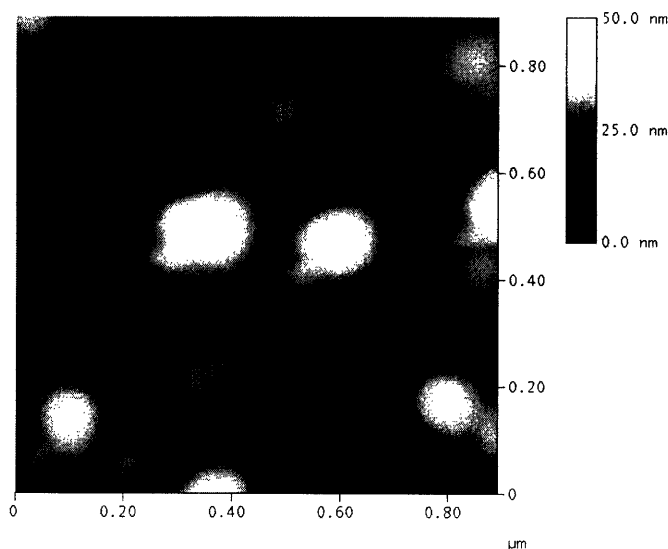


**Figure 22: AFM scan of the surface of a LiCoO<sub>2</sub> crystal. The scan size is 0.9 μm. The color scale indicates the topography of the sample. This image is a close-up of the crystal top surface shown in Figure 21. The bumps on the surface of the crystal are 50 to 250 nm in diameter, and 5 to 15 nm in height. Some of the bumps seem to have similar shapes. This is most probably a tip shape artifact.**

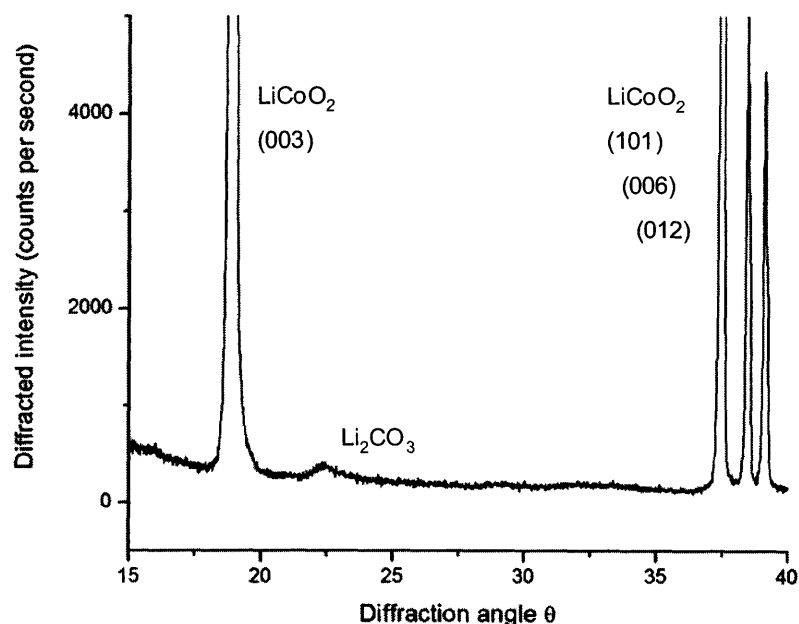


**Figure 23:** X-ray diffraction pattern of the  $\text{LiCoO}_2$  sample after storage in air for 6 months, zoomed on the background for angles  $15^\circ$ – $40^\circ$ . The pattern shows the presence of  $\text{Li}_2\text{CO}_3$  impurities in the sample. It is believed that  $\text{Li}_2\text{CO}_3$  is a product of the reaction between  $\text{LiCoO}_2$  and  $\text{CO}_2$  present in air.

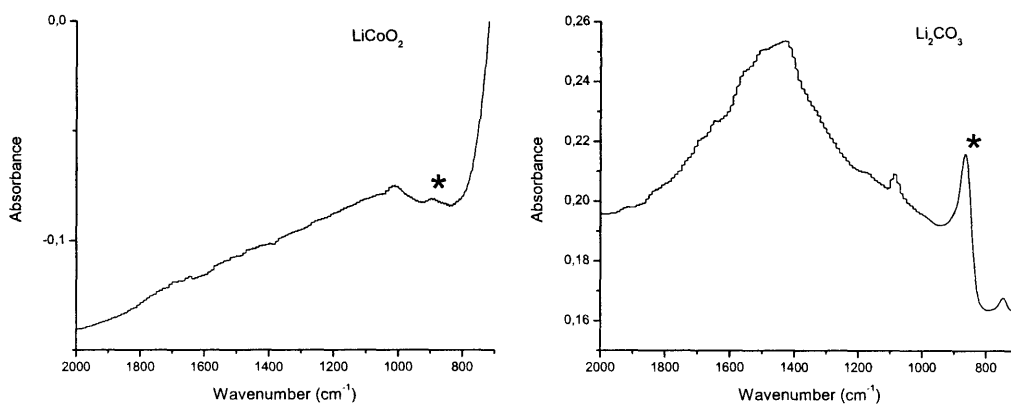


**Figure 24:** FT-IR spectra of  $\text{Li}_2\text{CO}_3$  and  $\text{LiCoO}_2$ . The data were collected in transmittance mode on a Thermo Nicolet Magna 860 (USA), and a pellet was prepared for imaging with approximately 95% KBr and 5%  $\text{Li}_2\text{CO}_3$  or  $\text{LiCoO}_2$ . The KBr spectrum was removed from the data shown here. The  $\text{LiCoO}_2$  sample was stored in air for 6 months after synthesis and shows the presence of  $\text{Li}_2\text{CO}_3$  on the surface of the crystals: the  $\text{LiCoO}_2$  spectrum has a peak around  $870\text{cm}^{-1}$ , which corresponds to the peak attributed to the bending mode of  $\text{CO}_3$  (shown with an asterisk on the graphs).



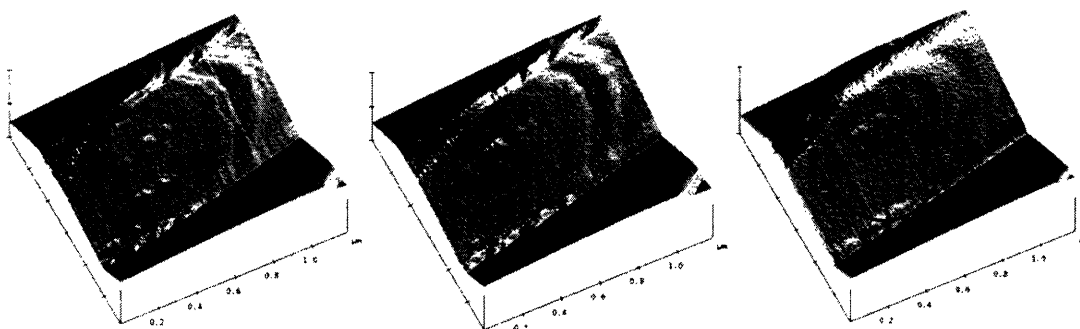


**Figure 25: 3D images of AFM scans. The scan size is 1.165  $\mu\text{m}$ . All three scans correspond to the same area of the crystal edge, and imaging as done in electrolyte, without applying an electric current. The images, from left to right, were recorded at the beginning of the experiment, after 15 minutes, and after one hour. The bumps present on the face of the crystal seem to disappear gradually over time.**

#### **2.2.4 Evolution of crystal morphology during charge and discharge**

##### **Objectives:**

Many  $\text{LiCoO}_2$  crystals have growth steps parallel to the (003) basal plane. This plane corresponds to the direction of the lithium, cobalt and oxygen planes in the crystal structure. As lithium ions are intercalated in and out of the material during cycling, the spacing between these layers expands and contracts. It is therefore expected that there will be some evolution of the overall morphology of the crystal during cycling. Using in-situ AFM, growth steps on a single crystal were imaged and their evolution was studied.

##### **Method for measuring step heights:**

The evolution of crystal step heights was studied in detail for several experiments, two of which are presented in detail below. In each experiment, the same crystal was imaged by AFM repeatedly during cycling of the in-situ electrochemical cell. Large flat surfaces of a crystal probably correspond to the (003) basal plane and the steps existing on the edges of these planes were imaged. The height of the steps was measured using the “Stepheight” function in the Nanoscope software provided by Veeco. This function uses line scans to measure height differences. The line scans do not correspond to a single line, but are averaged over a number of adjacent lines. This way, errors due to uneven surface layers are minimized. For each step, the height was initially measured 10 times to estimate the precision of the measurements. The standard deviation was calculated and corresponds to the error bars in the step height plots shown in the following pages.

## Experiment 050605:

Figure 27 shows three-dimensional images of the same crystal at different times: initially, after charge, during discharge and after the end of discharge. The electrochemical cell was charged galvanostatically at a rate of  $C/4$  for two hours, then left at open circuit for 30 min, and finally discharged at  $C/4$  for almost two hours. Figure 26 shows the voltage curve of this electrochemical cell alongside the reference voltage curve of coin cell 083004b\_11. The value of the lithium content  $x$  in  $\text{Li}_x\text{CoO}_2$  is calculated from the amount of active material in the sample and is very approximate because of the precision of the balance used in weighing.

The overall shape of the crystal does not seem to evolve much during cycling. An evolution in the surface layer on the crystal can be noted, and this is discussed in other sections.

The step height was measured for different steps present on the crystal. The orientation in which these measurements were taken is shown in Figure 28. The evolution of the step height compared to its initial value is shown in Figure 29 as a function of time during cycling. The evolution of the step height is expressed as a percentage of change:

$$\text{Percentage of change} = (\text{Step height} - \text{initial step height}) / \text{initial step height} * 100$$

During the initial rest step, the step height is at a low value. As the cell is charged, the voltage increases slowly around 4.1V. The step height increases gradually by approximately 4% and then decreases slightly to about +3%. When the cell has been charged half-way, it is allowed to reach equilibrium at open-circuit. The cell voltage decreases slightly and is almost constant at the end of the rest step. The decrease rate is 0.5mV/minute. At the same time, the step height stays constant. It may decrease slightly, but this trend is within experimental error. Lastly, the cell is discharged and the voltage decreases rapidly below 3V and reaches a plateau at around 2.5V. The poor reversibility of this cell may be due to the fast charge/discharge rate, and to the degradation of the electrolyte properties. The cell is kept under flowing argon during the experiment and the electrolyte evaporates continuously. By the end of the discharge, part of the electrolyte has crystallized and has a gel-like texture. Reducing the argon flow rate to a minimum

value was not sufficient to solve this problem. In future experiments it might be necessary to install a continuous flow of electrolyte in the cell to avoid this problem. During the discharge, the step height decreases approximately to its original value. The step height was only measured in AFM images corresponding to voltage values above 3V. Below 3V, lithium intercalation is not expected to be predominant, but rather other reactions are taking place.

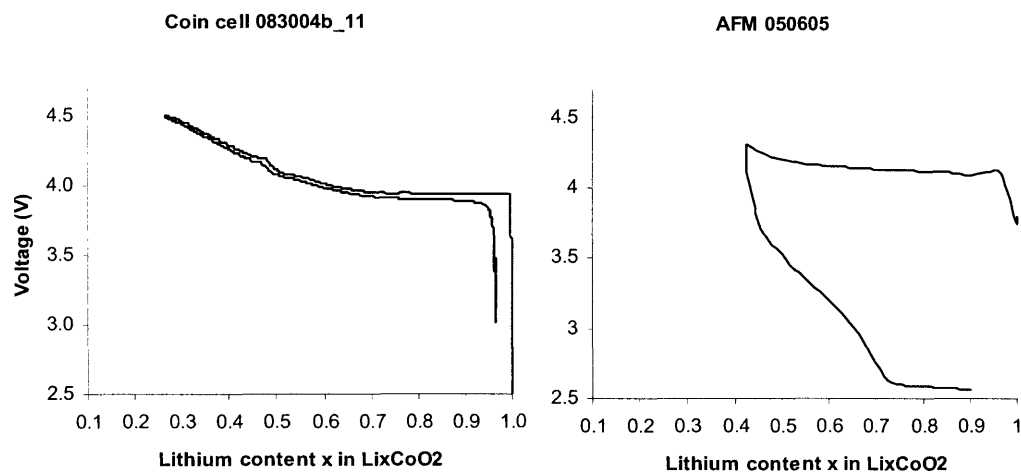


**Figure 26: Potential curve of the in-situ electrochemical cell used in experiment 050605 (left) shown alongside the potential curve of coin cell 083004b\_11 (right). The AFM cell was charged galvanostatically at a rate of  $C/4$  to an approximate lithium content of  $x=0.5$ . After a 30 minute rest step, the cell was discharged at  $C/4$ . The reference coin cell was cycled at a rate of  $C/50$ .**

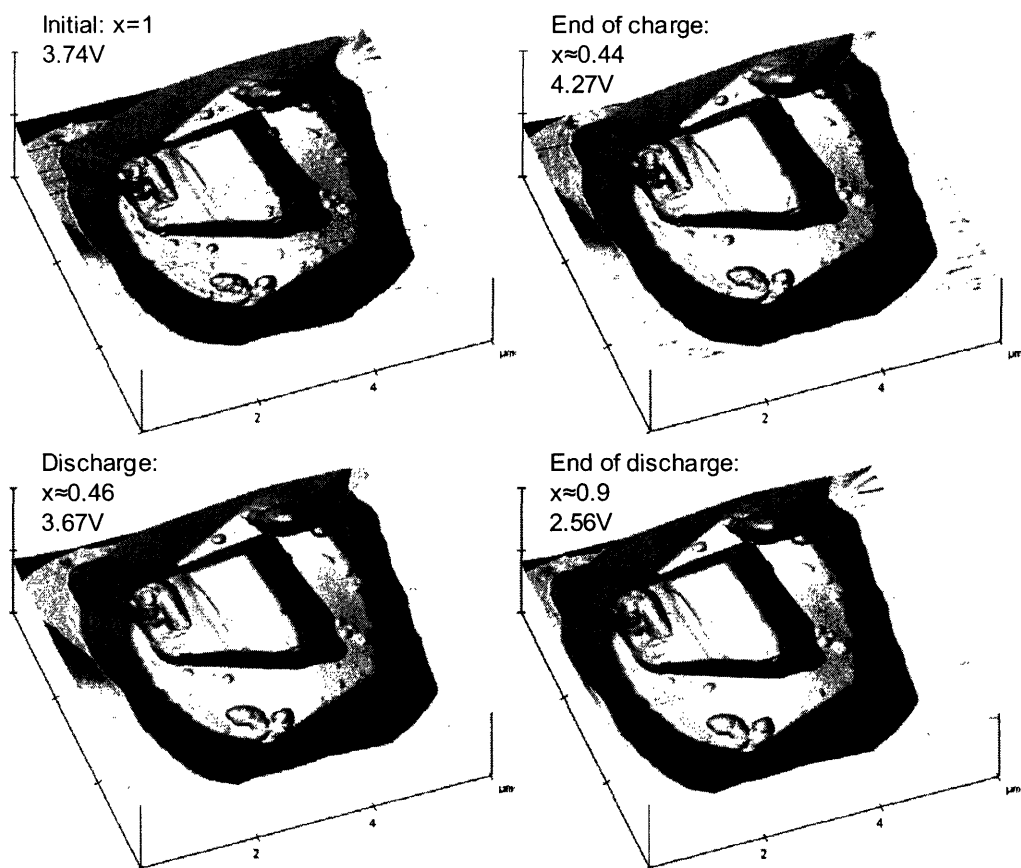


**Figure 27: 3D images of AFM scans in experiment 050605. The same crystal is shown initially, at the end of charge, during discharge, and at the end of discharge. The overall morphology of the crystal does not seem to evolve much. The height of the steps on the sides of the crystal were measured and their evolution was studied throughout cycling.**

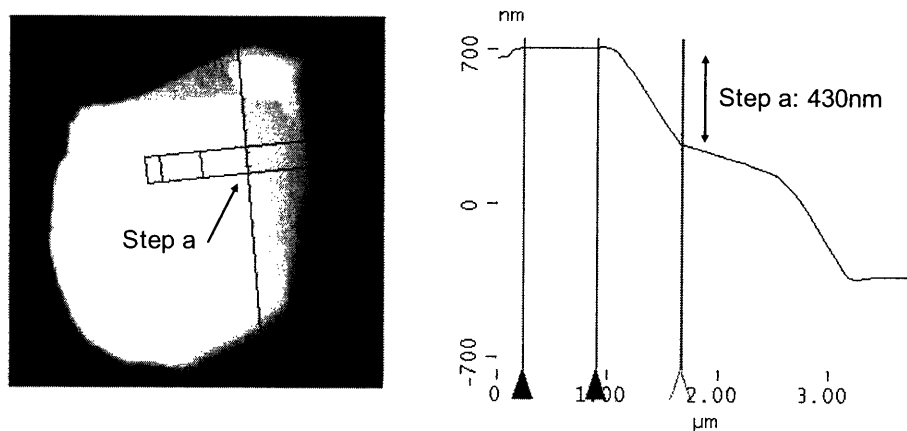


**Figure 28: Measure of the step height on the crystal.**

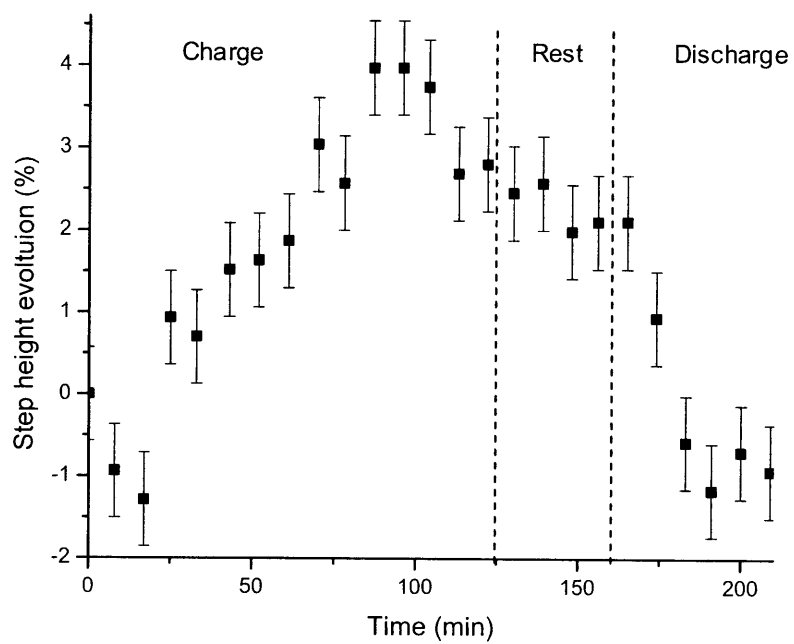


**Figure 29 : Evolution of the step height during experiment 050605. Step a was measured for different lithium contents.**

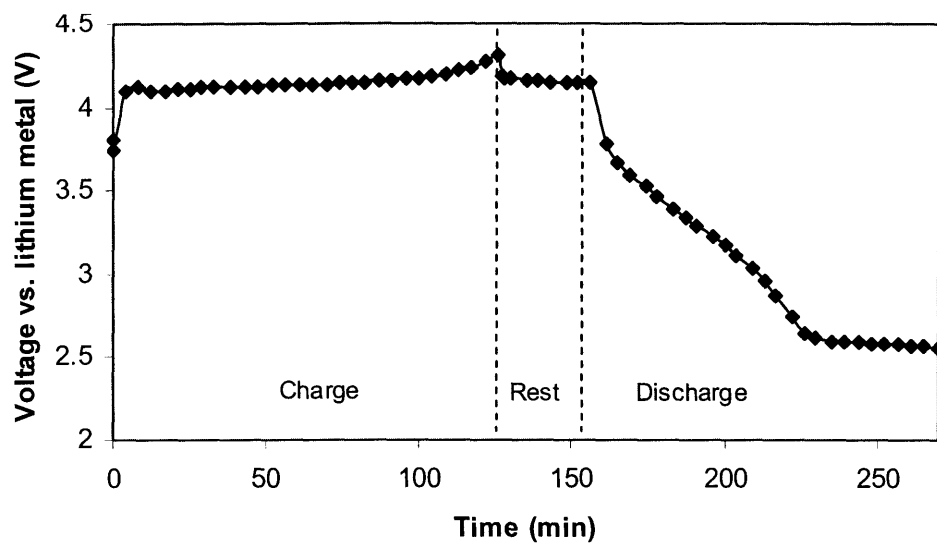


**Figure 30: Potential curve of AFM cell 050605 as a function of time. The cell was charged and discharged at a rate of C/4 and held at open-circuit for 30 min between charge and discharge.**



### Experiment 042505:

Figure 32 shows three-dimensional images of the same crystal at different times: initially, after charge, during discharge and after the end of discharge. The electrochemical cell was charged galvanostatically at a rate of  $C/2$  for one hour, then left at open circuit for 10 min, and finally discharged at  $C/2$  for almost one hour. Figure 31 shows the voltage curve of this electrochemical cell alongside the reference voltage curve of coin cell 083004b\_11. The value of the lithium content  $x$  in  $\text{Li}_x\text{CoO}_2$  calculated from the amount of active material in the sample is very approximate because of the precision of the balance used in weighing. Therefore the lithium content  $x$  was estimated using the potential curve and the correspondence relation between  $x$  and potential derived from the reference potential curve of coin cell 083004b\_11.

The overall shape of the crystal does not seem to evolve much during cycling. Another crystal can be seen in the first two images of Figure 32. This other crystal disappears in later images. It probably was not embedded enough in the gold foil and was pushed away by the AFM tip. An evolution in the surface layer on the crystal can be noted, and this is discussed in other sections.

The step height was measured for different steps present on the crystal and the orientation in which these measurements were taken is shown in Figure 33. Steps a and d correspond to the same feature on the crystal, therefore should have similar values. There may be some random errors in measuring the step heights because the shape of the crystal is slightly rounded. In order to achieve a more accurate measure of the steps, the average of steps a and d was calculated and its evolution measured. The evolution of this average values is shown in Figure 34 as a function of time during cycling. The evolution of the step height is expressed as a percentage of change:

$$\text{Percentage of change} = (\text{Step height} - \text{initial step height}) / \text{initial step height} * 100$$

Initially the step height is at a low value. At the onset of charge, the step height increases by approximately +6% and then decreases again. During the end of the charge and the open-circuit rest step, it stays almost constant, within measuring errors. Finally, during

discharge the step height increases again to approximately +7% of its initial value and then decreases to approximately its initial value.

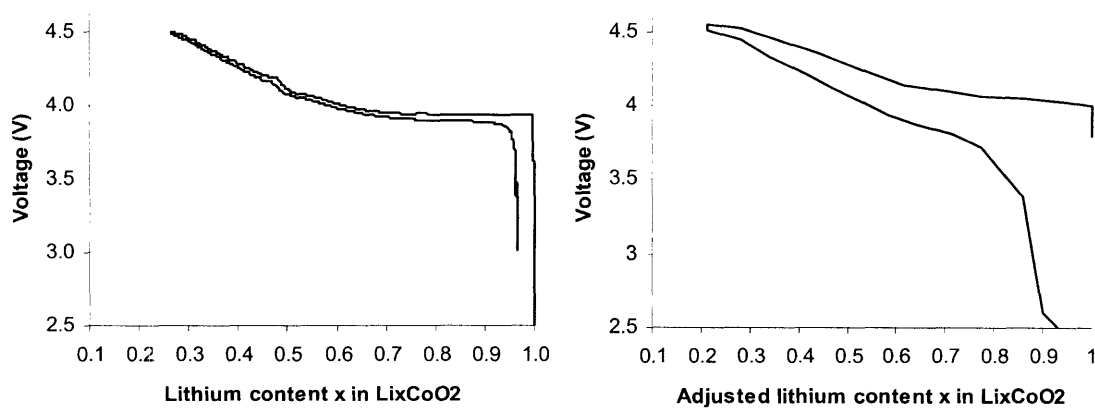


**Figure 31: Potential curve of the in-situ electrochemical cell used in experiment 042505 (left) shown alongside the potential curve of coin cell 083004b\_11 (right). The AFM cell was charged galvanostatically at a rate of  $C/2$  to an approximate lithium content of  $x=0.5$ . After a 10 minute rest step, the cell was discharged at  $C/2$ . The reference coin cell was cycled at a rate of  $C/50$ .**

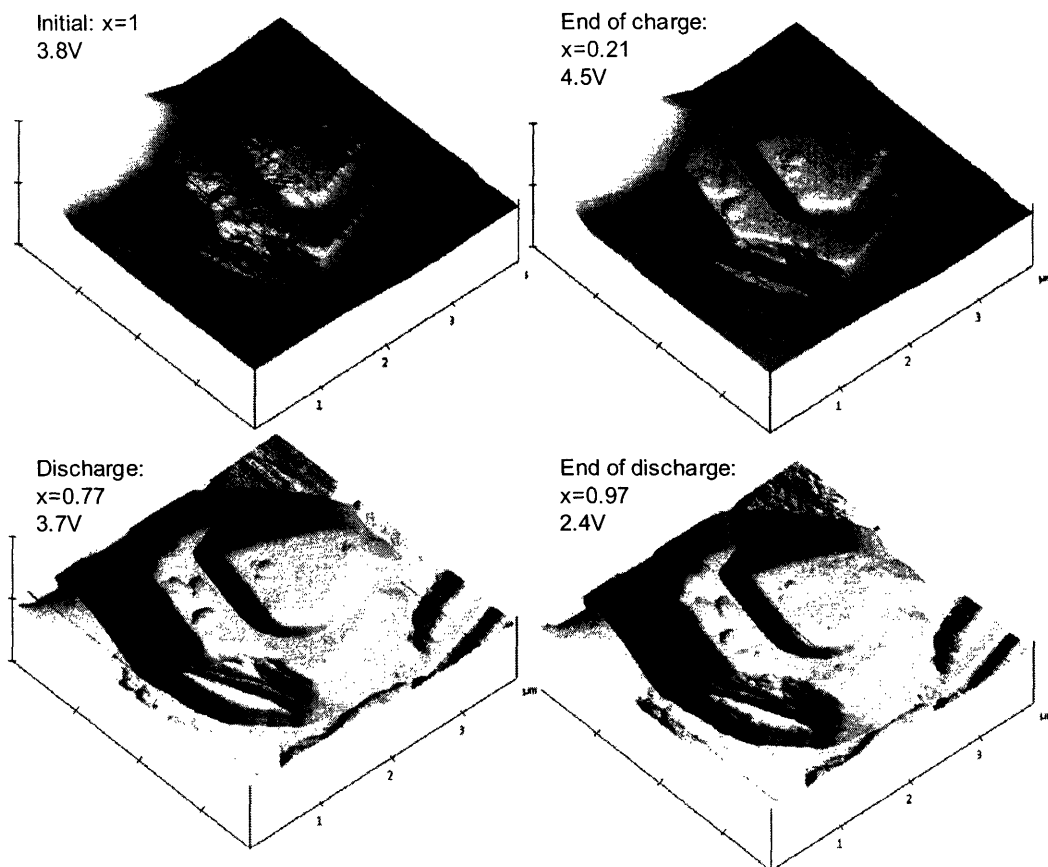


**Figure 32: 3D images of AFM scans in experiment 042505. The same crystal is shown initially, at the end of charge, during discharge, and at the end of discharge. Another crystal was present on the left-hand side of the top images. This crystal disappeared in later images, probably pushed away by the AFM tip. The overall morphology of the crystal does not seem to evolve much. The heights of the steps on the sides of the crystal were measured and their evolution was studied throughout cycling.**

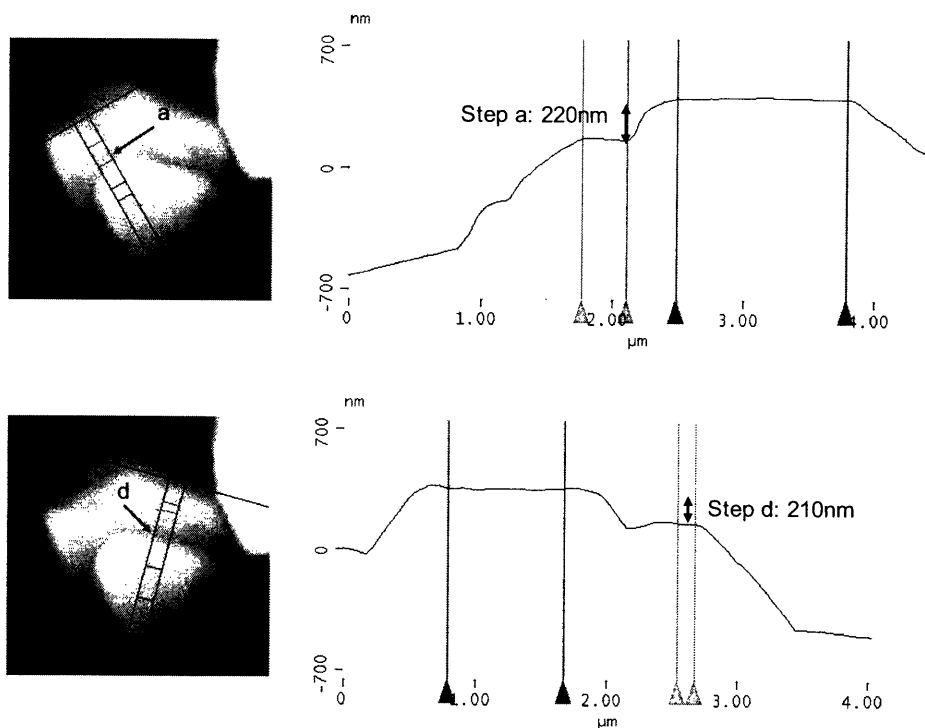


**Figure 33: Measures of the step heights on the edge of the crystal, in two directions.**

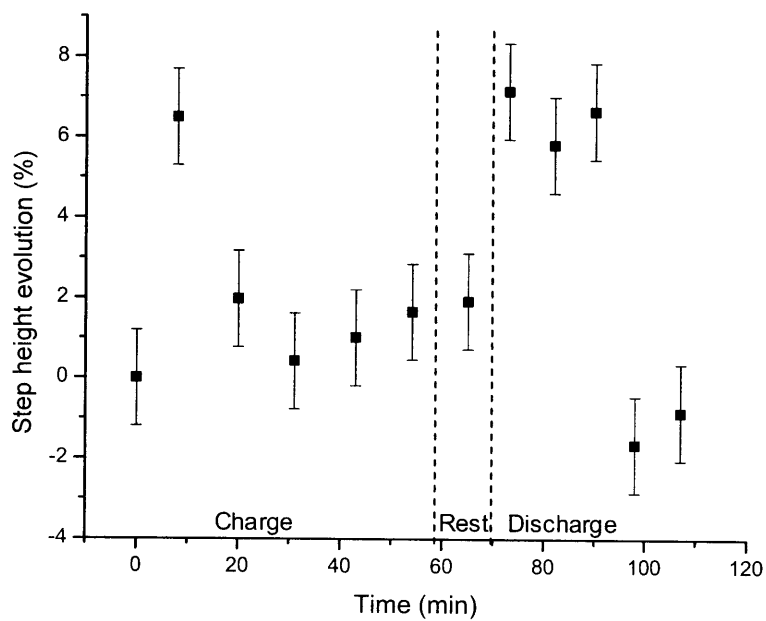


**Figure 34: Evolution of the step height during experiment 042505. Steps a and d correspond to the same feature on the crystal, measured in different directions. Therefore the evolution of the average of steps a and d was analyzed.**

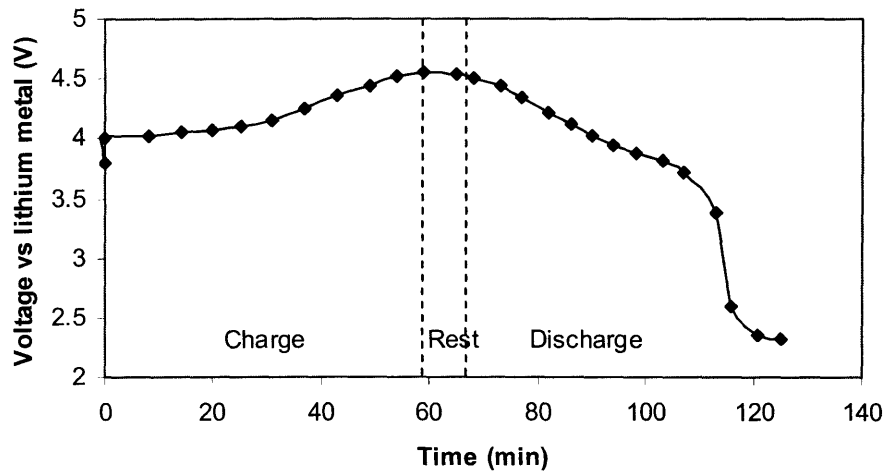


**Figure 35: Potential curve of the in-situ electrochemical cell used in experiment 042506. The cell was charged galvanostatically at a rate of  $C/2$  to an approximate lithium content of  $x=0.5$ . After a 10 minute rest step, the cell was discharged at  $C/2$ .**

### **Interpretation of the results:**

Other researchers have measured the evolution of lattice spacing in  $\text{Li}_x\text{CoO}_2$  as a function of  $x$  by X-ray Diffraction and have shown that the layer spacing increases during the beginning of charge, reaches a maximum at around  $x=0.5$  and then decreases again for lower values of  $x$  (Figure 36) [7]. This behavior is reversible for the most part. At a lithium concentration of 50% the lattice spacing has increased by 3.5% compared to the value at  $x=1$ . For lower lithium contents, the material goes through a transition to a monoclinic structure and the lattice spacing decreases by up to 10%, compared to the value at  $x=1$ .

In the paragraphs below, the evolution of step height during charge, rest and discharge are analyzed and compared for experiments 050605 and 042505, and interpretations are given.

#### Charge:

In both experiments, the step height increases to a maximum and then decreases during the charge step. This is consistent with X-ray diffraction data. According to XRD measurements of the layer spacing, this maximum is reached at a lithium concentration of 50%. However, in our AFM experiments, the lithium concentration in  $\text{Li}_x\text{CoO}_2$  is not 50% when the step height maximum is reached. This discrepancy could be due to two factors. First, the amount of active material in each AFM sample is only known approximately. This amount is measured by weighing the gold foil before and after pressing  $\text{LiCoO}_2$  crystals onto it. However, the amount of  $\text{LiCoO}_2$  typically used is on the order of 0.1mg, close to the precision of the balance. An error on the weighing will lead to an error in the calculated lithium content in the material. Second, the calculated lithium content is an average value for all the crystals present in the sample. In reality, some crystals may be charged faster than others.

Furthermore, different steps might evolve at different speeds. It is suspected that lithium ions de-intercalate first out of selected layers. As lithium ions are pulled out of one layer, vacancies are created and the diffusivity of lithium ions increases. It is easier to remove

more lithium ions from that same layer than from other layers. Figure 37 shows a schematic of this mechanism for step expansion. If this hypothesis holds true, some steps will be depleted of lithium faster than others, and their height will reach a maximum even before the average lithium content of the active material reaches 50%.

As lithium concentration reaches 50% at the edge of the crystal, the rhombohedral-monoclinic transition starts taking place, which corresponds to the largest c lattice parameter. After the monoclinic transition around 0.45, the lattice parameter begins to decrease. All step height measurements show a decrease at the end of charge.

Lastly, the evolution of step heights is expressed in terms of percentage of change in comparison with a lithium concentration of 100%. Measured step heights increase by 4% in experiment 050605 and 6% in experiment 042505. These values are not completely consistent with the increase of 3.5% measured by XRD, but they are of the same order of magnitude.

#### Open-circuit rest step:

At the end of charge, the cell is allowed to rest during 10 to 30 minutes, and the lithium concentration tends to reach equilibrium inside the crystal. Both sets of measurements show that the step height is constant or slightly decreasing during rest.

#### Discharge:

In experiment 050605, the voltage decreased very fast during discharge and it is difficult to form conclusions on the data.

In experiment 042505, the voltage curve shows that the discharge was good. When the discharge starts, more lithium ions are intercalated into the edge of the crystal, leading to the step expansion. When the concentration of lithium ions in the crystals becomes larger than 50%, the layer spacing starts decreasing again. This evolution is consistent with XRD data, and corresponds to the inverse of the evolution during charge.



**Conclusions:**

The step heights measured in experiments 042505 and 050605 show similar trends during the de-intercalation of lithium ions from the material: the step height increases and then decreases. This evolution is consistent with XRD studies previously conducted by other groups. The magnitude of the step expansion is 4-6%, comparable to that measured by XRD.

Only experiment 042505 shows good electrochemical data for the discharge. During lithium intercalation, the step height increases and then decreases, corresponding to XRD results.

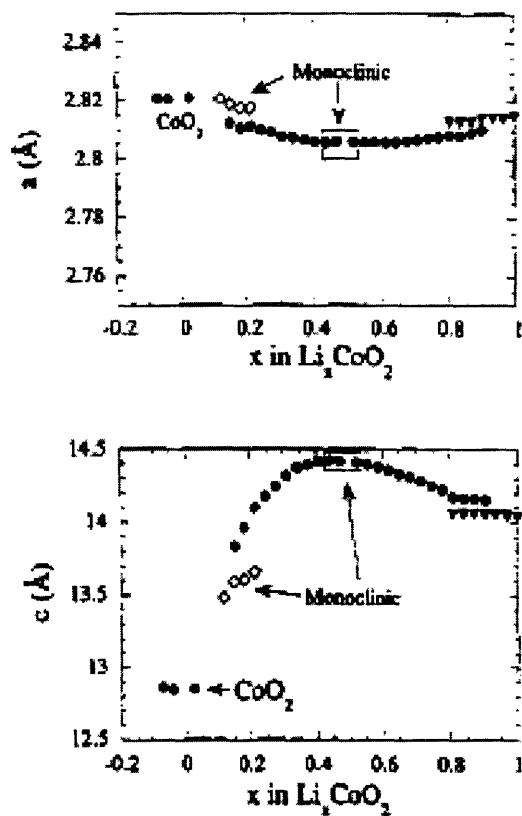


Figure 36: Evolution of  $\text{Li}_x\text{CoO}_2$  cell parameters as a function of lithium content [7].

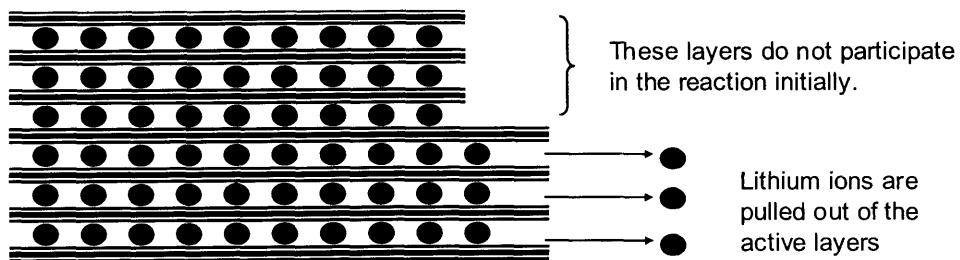


Figure 37: Mechanism for step expansion during charge. Lithium ions are first pulled out of selected layers. As lithium ions are pulled out of one layer, vacancies are created and the diffusivity of lithium ions increases. Therefore it is easier to remove more lithium ions from that same layer.

### 2.2.5 The effect of over-discharge

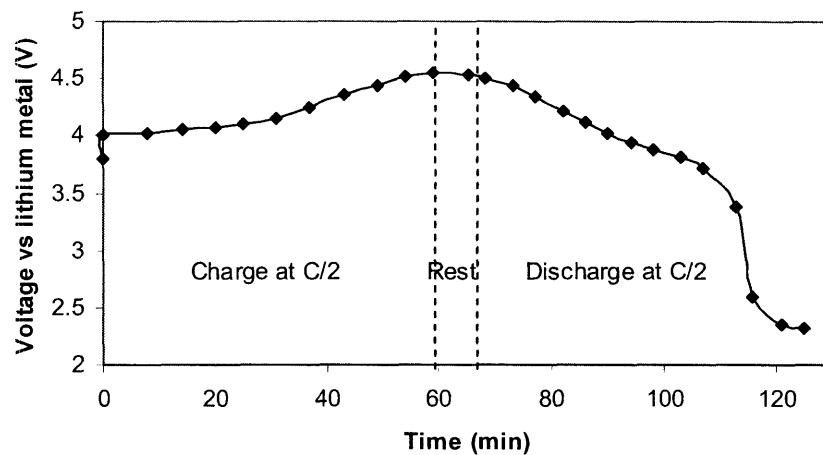
In some experiments, the sample was successfully charged and discharged at a rate of C/2. Typically the sample was charged for one hour, which corresponds to the removal of half of the lithium from the lithium transition metal oxide, and then discharged for one hour. The  $\text{Li}_x\text{CoO}_2$  crystals do not recharge fully: some of the lithium ions cannot be re-intercalated back into the host structure. When this occurs, the cell potential drops to less than 3V. Different experiments show that surface features appear as the cell potential goes below 3V.

Figure 39 shows three-dimensional images of a crystal imaged at the end of discharge in experiment 042505. A zoomed height image of the top surface of the crystal is also shown. Figure 38 shows the voltage curve corresponding to the same in-situ cell. The images on the left of Figure 15 were taken before the voltage drop (at 3.39V) and the images on the right were taken after the voltage drop (at 2.36V). At the voltage drops to approximately 2.3V, surface features appear on the crystal. These surface features are rounded bumps, around 100 to 150 nm in diameter and 2 to 3 nm in height.

These surface features are shown to appear on the crystal surface in experiment 042505, but it seems that similar features also appear on the gold foil at the end of discharge in experiment 042605. Figure 41 shows two three-dimensional images corresponding to two consecutive scans of the sample at the end of discharge and Figure 40 is the potential plot corresponding to this experiment. The images represent the surface of the gold foil with a cell potential of 2.343V and 2.336V, respectively. Some rounded bumps appear on the gold foil between the two scans. The largest bump is 300nm in diameter and 30nm in height.

To conclude, similar rounded bumps appear on the surface of the crystals and the gold foil at the end of discharge, when the potential drops below 3V. It seems that the potential then has a plateau around 2.3V, which could correspond to another electrochemical reaction. Figure 12 shows the cyclic voltammetry curve of a coin cell containing gold foil and lithium metal. The discharge during the first cycle exhibits a peak at approximately 2.3V, which could correspond to the same phenomenon. One hypothesis is that lithium

ions cannot intercalate back into the host structure and interact with surface layers on  $\text{LiCoO}_2$ .



**Figure 38: Voltage curve of the in-situ AFM cell 042505. The working electrode is  $\text{LiCoO}_2$  crystals pressed onto a gold foil, the counter and reference electrodes are lithium metal, and the electrolyte is  $\text{LiPF}_6$  in EC:DEC. The cell was charged halfway and discharged at  $C/2$ . The cell does not recharge entirely, and the cell potential drops significantly at the end of discharge.**

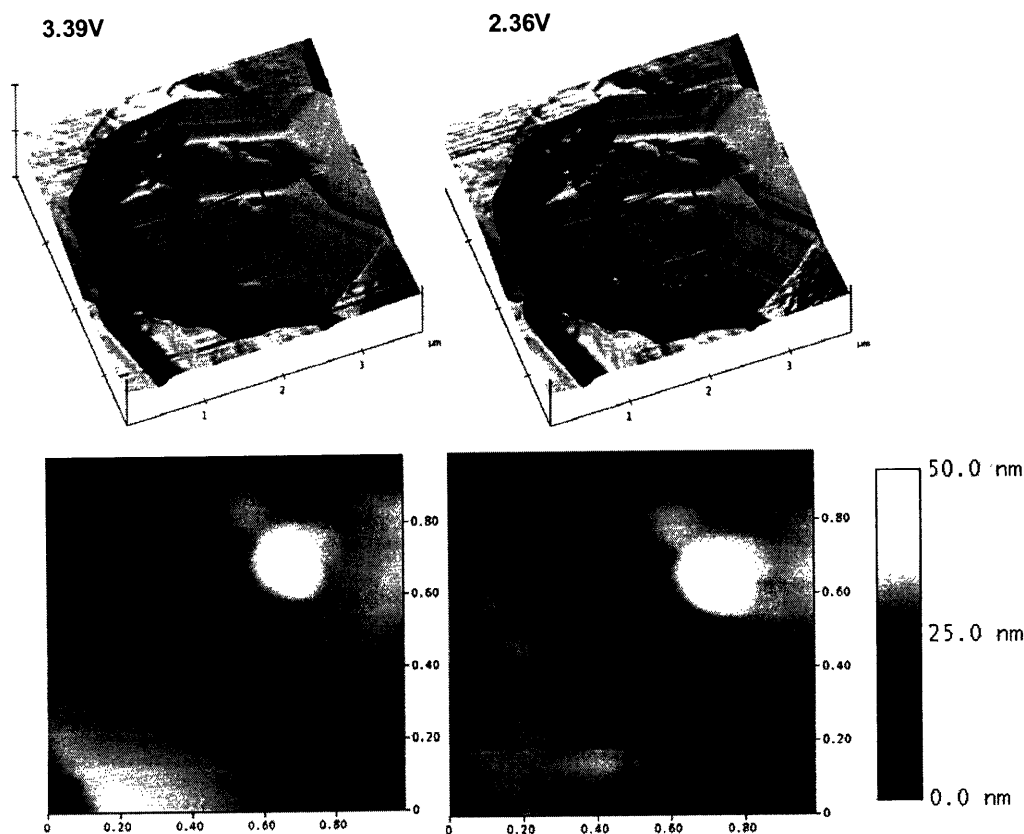


**Figure 39: 3D images and height images corresponding to two AFM scans of a crystal in sample 042505 during discharge of the cell. The three-dimensional images show the entire crystal. The height images represent a zoomed image of the top surface of the crystal. The image size is 1 $\mu$ m and the height scale is 50nm, the same in both images. The images on the left were taken when the cell potential was 3.39V, and the images on the right were taken when the cell potential was 2.36V. The images corresponding to the lower potential show that surface features have appeared on the surface of the crystal.**

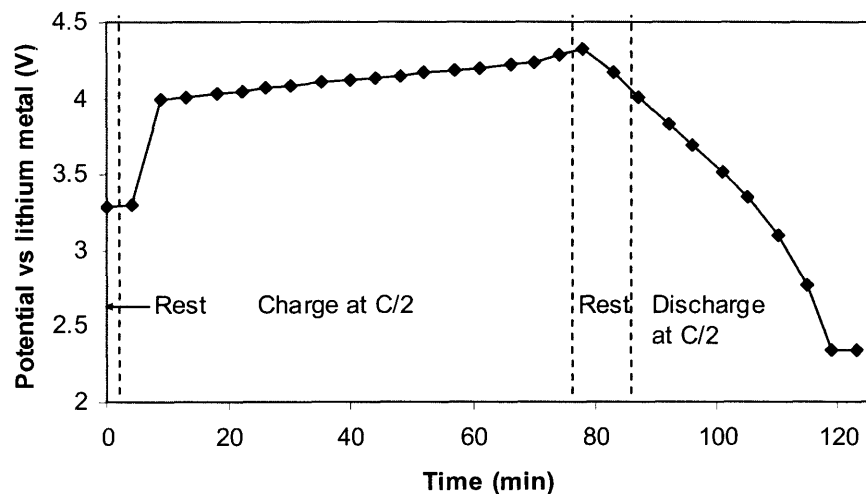


**Figure 40: Potential curve of in-situ cell used in experiment 042605. The cell was charged and discharged halfway at C/2. The potential drops sharply at the end of discharge and seems to plateau again at approximately 2.3V.**

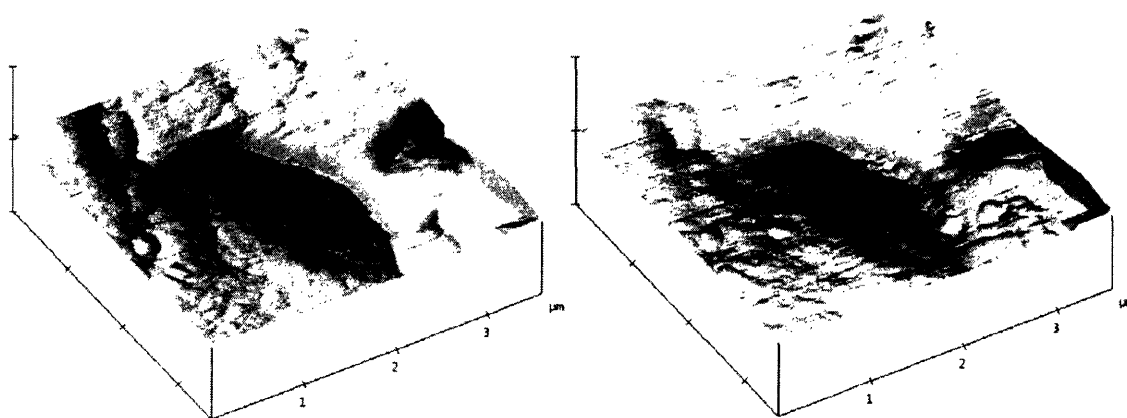


**Figure 41: Three-dimensional images of consecutive AFM scans of the gold foil at the end of the discharge of cell 042604. The indentation in the gold foil was left by a crystal which was pushed away by the AFM tip. The image on the left was recorded at a cell potential of 2.343V, and the image on the right at 2.336V. Some rounded bumps appear on the gold foil between the two scans.**

## 2.3 Conclusions

This work shows the potential of Scanning Probe Techniques in the dynamic study of battery materials during cycling. Atomic Force Microscopy gives unique insight into the evolution of the overall morphology as well as the surface features of  $\text{Li}_x\text{CoO}_2$  crystals as lithium content  $x$  is varied. Beyond surface morphology, surface conductivity and surface mechanical properties can also be measured.

AFM scans of pristine  $\text{LiCoO}_2$  crystals show the presence of rounded bumps on their surface, which corresponds probably to the  $\text{Li}_2\text{CO}_3$  impurity present in the sample. Step expansion and contraction was studied during cycling charge and discharge of a crystal, and found to correlate with the evolution of cell parameters measured from XRD. Lastly, surface layer formation was found to occur if the cell is discharged to a potential of 2.3V vs. lithium metal.



### **3 TEM studies and AC impedance studies of $\text{Li}_x\text{CoO}_2$**

The second part of this study focuses on the insulator-metal transition occurring in  $\text{Li}_x\text{CoO}_2$  for lithium concentrations between  $x=0.75$  and  $x=0.94$ . Several measurement techniques (XRD, TEM, EIS) were applied to study the material at different lithium concentrations corresponding to the phase transition. The phase transition was studied by X-ray diffraction to examine crystal structure and cell parameters, by Transmission Electron Microscopy to find evidence of this phase transition in individual  $\text{Li}_x\text{CoO}_2$  crystals and by AC Impedance Spectroscopy to examine electroanalytical behavior.

#### **3.1 Experimental**

##### **3.1.1 Preparation of coin cells**

The synthesis of  $\text{LiCoO}_2$  and the preparation of coin cells were described in Part 1. Coin cells were charged galvanostatically at a rate of C/100 to obtain different lithium concentrations in  $\text{Li}_x\text{CoO}_2$ :  $x=0.97$ ,  $0.85$ ,  $0.75$ . The coin cells were transferred to the glovebox directly after the charging was finished. They were opened using pliers covered in insulating tape to avoid shorting, and the positive electrode was retrieved. The electrodes were rinsed in EC and allowed to dry. The active material was then scraped off the aluminum foil and used to prepare two TEM samples and one XRD sample per coin cell.

##### **3.1.2 XRD testing**

XRD samples were prepared inside the glovebox by placing some of the  $\text{Li}_x\text{CoO}_2$  charged material onto a glass sample plate. The material was held onto the sample plate by a few drops of binder (Collodion in Amyl Acetate).

XRD measurements were conducted in a Rigaku RU300 powder diffractometer, using copper  $\text{K}\alpha$  radiation. The sample was transferred from the glovebox to the X-ray diffractometer in a sealed container, and was placed in flowing helium during XRD scans. Therefore the sample was exposed to air as little as possible.

Cell parameter refinement from XRD data was performed using commercial software Jade.

### **3.1.3 TEM testing**

TEM samples were prepared by mixing charged  $\text{Li}_x\text{CoO}_2$  crystals in acetone using ultrasounds. Copper grids with lacey carbon films from Ted Pella were used as a support for the powder. To prepare a sample, a grid was dipped inside the solution containing the crystals and allowed to dry.

TEM samples were imaged within less than hour of preparation. Most TEM samples were prepared in air. The samples with a lower lithium content ( $x=0.75$ ) were prepared inside the glovebox by suspending the crystals in DEC.

TEM imaging was performed on JEOL 2000 and JEOL 2010 microscopes.

### **3.1.4 AC impedance spectroscopy**

Coin cells were charged at a slow rate of  $C/100$  and the charge was interrupted in order to perform impedance spectroscopy measurements for different lithium contents. Before and after each impedance step, the cell was allowed to reach equilibrium for 10 min at open-circuit. Impedance was measured for frequencies ranging from 10kHz to 15mHz for coin cell 083004b\_10 and 10mHz for coin cell 083004b\_14, with a perturbation voltage of 5mV.

Analysis of the impedance spectroscopy data was performed with commercial software Zview, with the help of Sundeep Kumar.

## **3.2 Results and discussion**

### **3.2.1 X-ray diffraction results and discussion**

X-ray diffraction was used to determine the lattice parameters in charged  $\text{Li}_x\text{CoO}_2$  samples, for  $x=1, 0.97, 0.85$  and  $0.75$ .

Figure 42, Figure 43 and Figure 44 show XRD patterns of as-prepared and charged  $\text{Li}_x\text{CoO}_2$  samples. For charged samples, very little  $\text{Li}_x\text{CoO}_2$  material was available for collecting the XRD pattern and binder was used to prepare the XRD sample. For the as-prepared sample, a lot of powder was used, and no binder. This is responsible for the presence of a larger amorphous background in the XRD patterns of charged sample, compared with the as-prepared sample. As lithium is removed from the material, it is observed that the (003) and (006) peaks shift towards the lower angles.

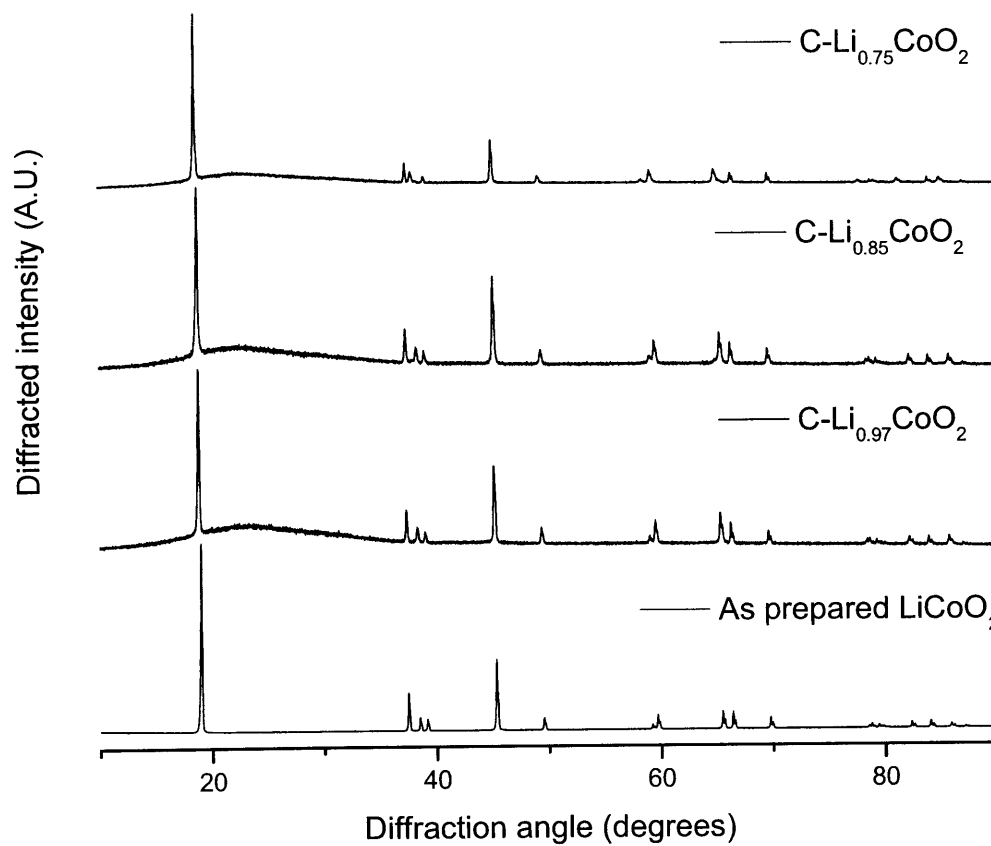


**Figure 42: X-ray diffraction pattern of as-prepared and charged samples of Li<sub>x</sub>CoO<sub>2</sub> for x=0.97, 0.85, 0.75.**

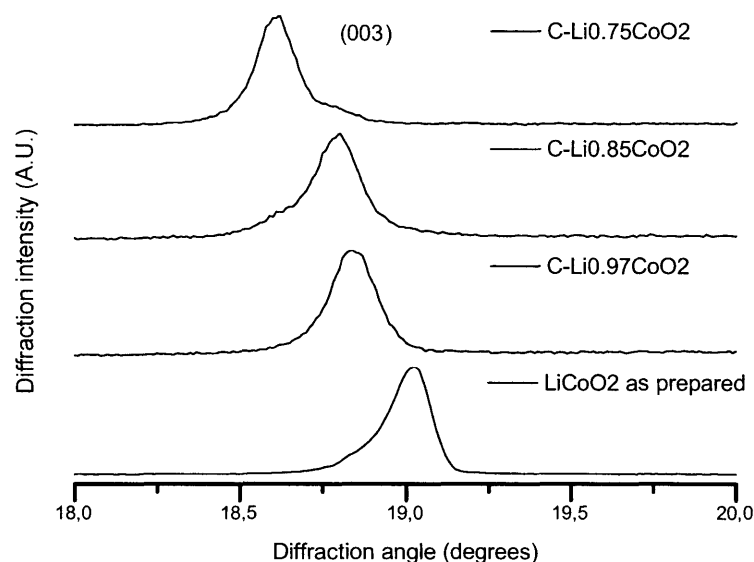


**Figure 43:** X-ray diffraction pattern of as-prepared and charged samples of  $\text{Li}_x\text{CoO}_2$  for  $x=0.97, 0.85, 0.75$ : close-up of the (003) peak. As lithium is de-intercalated from the material, the layer spacing increases, which causes the (003) peak to shift to the lower angles.

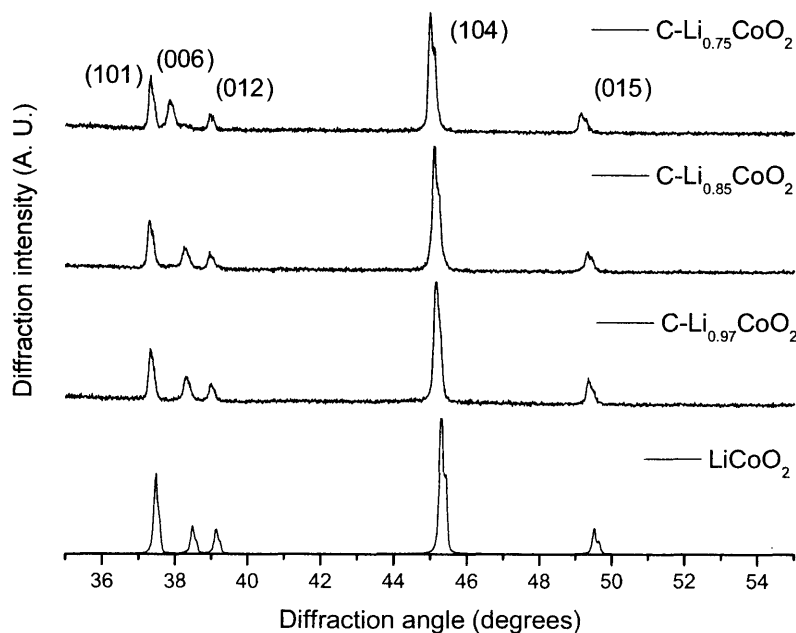


**Figure 44:** X-ray diffraction pattern of as-prepared and charged samples of  $\text{Li}_x\text{CoO}_2$  for  $x=0.97, 0.85, 0.75$ : close-up on the  $35^\circ$ - $55^\circ$  range. As lithium is de-intercalated from the material, the layer spacing increases, which causes the (006) peak to shift to the lower angles.

As lithium is intercalated out of the material, a two-phase transition occurs between  $\text{Li}_{0.75}\text{CoO}_2$  and  $\text{Li}_{0.94}\text{CoO}_2$ . Both phases have the same lattice type with very similar lattice parameters. The c lattice parameter is slightly larger in  $\text{Li}_{0.75}\text{CoO}_2$  than  $\text{Li}_{0.94}\text{CoO}_2$ , because as lithium atoms are deintercalated from between the oxygen planes, there is more electrostatic repulsion between the oxygen atoms. This causes the planes of oxygen atoms to be pushed apart. Therefore the  $\text{Li}_{0.75}\text{CoO}_2$  peaks should be at slightly lower angles than the  $\text{Li}_{0.94}\text{CoO}_2$  one. (003) and (006) peaks are particularly deviated because they correspond to the diffraction of the oxygen planes. Furthermore, this deviation will be larger at high angles.

Table 2 lists the as-prepared charged samples that were studied by XRD. The values of the c and a cell parameters were measured by refinement of the XRD patterns using the commercial Jade software.

**Table 2: Measured cell parameters in as-prepared and charged  $\text{Li}_x\text{CoO}_2$ . Coin cells were charged galvanostatically at a rate of C/100 until the desired lithium content was reached. The coin cell was then taken apart in a glove box and the cathode was examined by XRD.**

Extent of charging	Measured a (Å)	Error on a (Å)	Measured c (Å)	Error on c (Å)	c/a
$\text{LiCoO}_2$	2.8131	0.0013	14.0298	0.0056	4.99
C- $\text{Li}_{0.95}\text{CoO}_2$	2.8193	0.0012	14.0724	0.0045	4.99
C- $\text{Li}_{0.85}\text{CoO}_2$	2.8190	0.0011	14.0719	0.0053	4.99
C- $\text{Li}_{0.75}\text{CoO}_2$	2.8159	0.0016	14.2271	0.0074	5.05

The general trend is that the cell parameter a decreases and the cell parameter c increases as lithium is removed from the material. Ménétrier et al. [34] also conducted an XRD study of charged samples and our results are in agreement with the results that they report. There are slight differences in the values of the a and c parameters, however the ratio c/a is identical.

### 3.2.2 Transmission Electron Microscopy results and discussion

The objective of this TEM study of  $\text{LiCoO}_2$  is to examine the evolution of individual  $\text{Li}_x\text{CoO}_2$  crystals during the first charge, as the material is undergoing the insulator-metal phase transition.

#### 3.2.2.1 Characterization of the parent sample

First, the parent sample was characterized by electron diffraction patterns, shown in Figure 45. These electron diffraction patterns can be indexed to the hexagonal cell (space group  $R\bar{3}m$ , cell parameters  $a=2.815\text{\AA}$  and  $c=14.05\text{\AA}$ ).

Charged samples, with lithium contents of  $x=0.97; 0.96; 0.95; 0.85; 0.7$  were also studied by electron diffraction. The paragraphs below present the diffraction patterns collected from these samples and proposed a model to explain the observed super-lattice reflections.

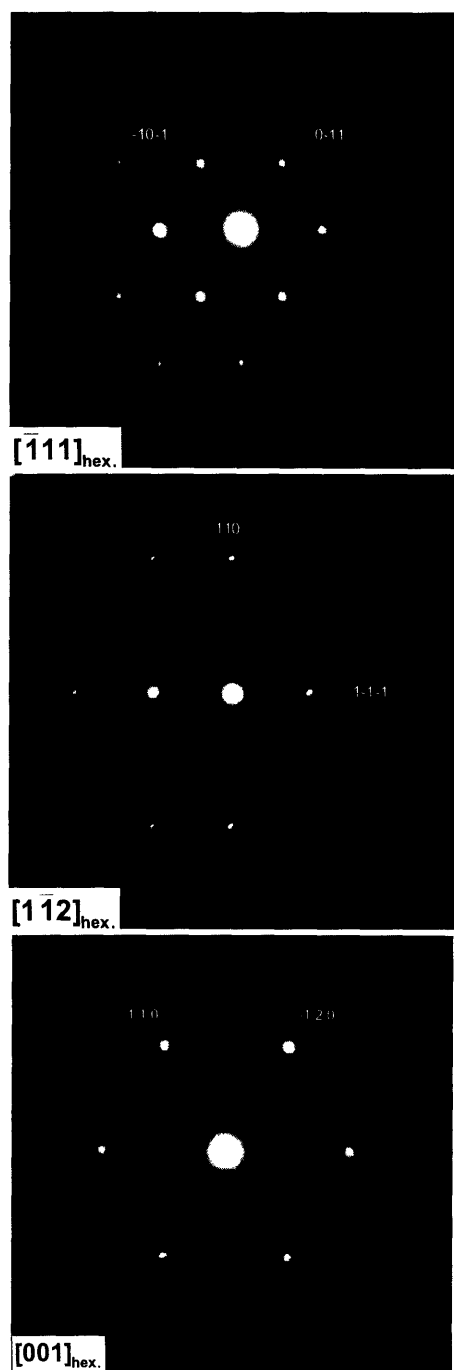


**Figure 45:** Electron diffraction patterns of the  $\text{LiCoO}_2$  parent phase. These diffraction patterns are indexed to the hexagonal cell and do not have super-lattice reflections. The zone axes are  $[-1\ 1\ 1]_{\text{hex}}$  for the pattern on the top and  $[1\ -1\ 2]_{\text{hex}}$  for the pattern in the center,  $[001]_{\text{hex}}$  for the pattern on the bottom.



### 3.2.2.2 Single-phase $\text{Li}_x\text{CoO}_2$ with lithium content in the range 0.7-0.75

#### Samples charged to $\text{Li}_{0.7}\text{CoO}_2$ :

In Figure 46, electron diffraction patterns collected from  $\text{Li}_{0.7}\text{CoO}_2$  charged samples are presented alongside patterns collected from  $\text{LiCoO}_2$  in the same zone axis. Weak spots are present in the diffraction pattern of the charged sample, which are not present in the diffraction pattern of the parent sample. In the  $[-1\ 1\ 1]$  zone axis, these extra reflections are present halfway between the central beam and the  $(-1\ -1\ 0)$  reflection. In the  $[1\ -1\ 2]$  zone axis, these extra reflections are present halfway in between the central beam and the  $(1\ 1\ 0)$  reflection. These extra reflections indicate that a superstructure cell exists in the charged material.

Two schematics of lithium-vacancy ordering in  $\text{Li}_{0.7}\text{CoO}_2$  are presented in Figure 47. The schematics describe how lithium ions and vacancies are located in the lithium planes. Both schematics can describe the observed superstructure in the sample.

The first schematic is based on the hexagonal cell, with alternating fully occupied lithium ion rows and partially occupied rows in the lithium planes. The partially occupied rows have no ordering and the statistical occupancy of the lithium ions is approximately 40% for  $\text{Li}_{0.7}\text{CoO}_2$ . The supercell is  $2a_{\text{hex.}} \times 2a_{\text{hex.}} \times c_{\text{hex.}}$ .

The second schematic is based on a monoclinic cell. The crystallographic relation between the monoclinic unit cell and the hexagonal unit cell is shown in Figure 48. The lithium planes have alternating fully occupied lithium ion rows and partially occupied rows. In the partially occupied rows, every other site has a vacancy, and the remaining sites have a statistical site occupancy of approximately 80%. The supercell is  $2a_{\text{mon.}} \times 2a_{\text{mon.}} \times 2c_{\text{mon.}}$ . The lithium layers are arranged in an ABAB manner, so that the c axis is also doubled.

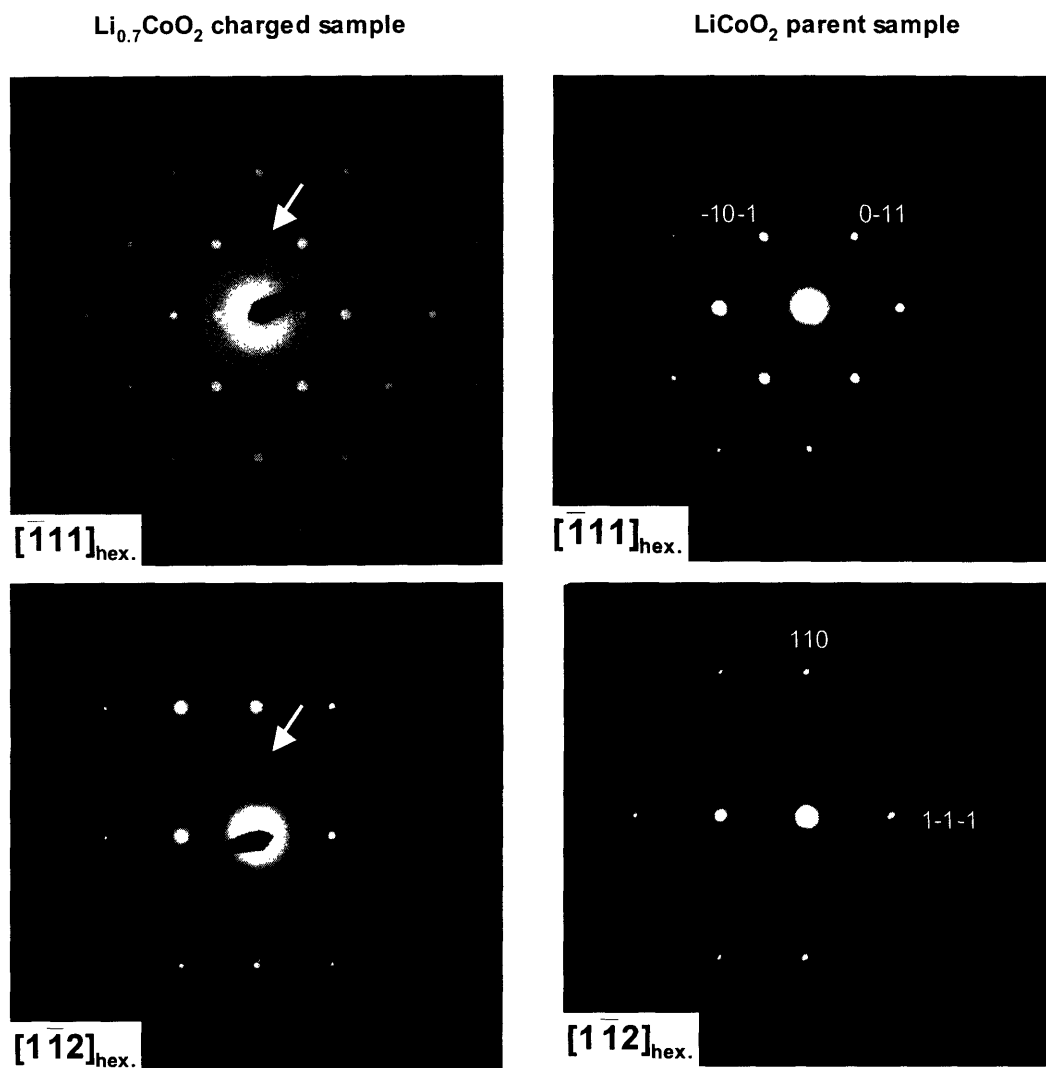
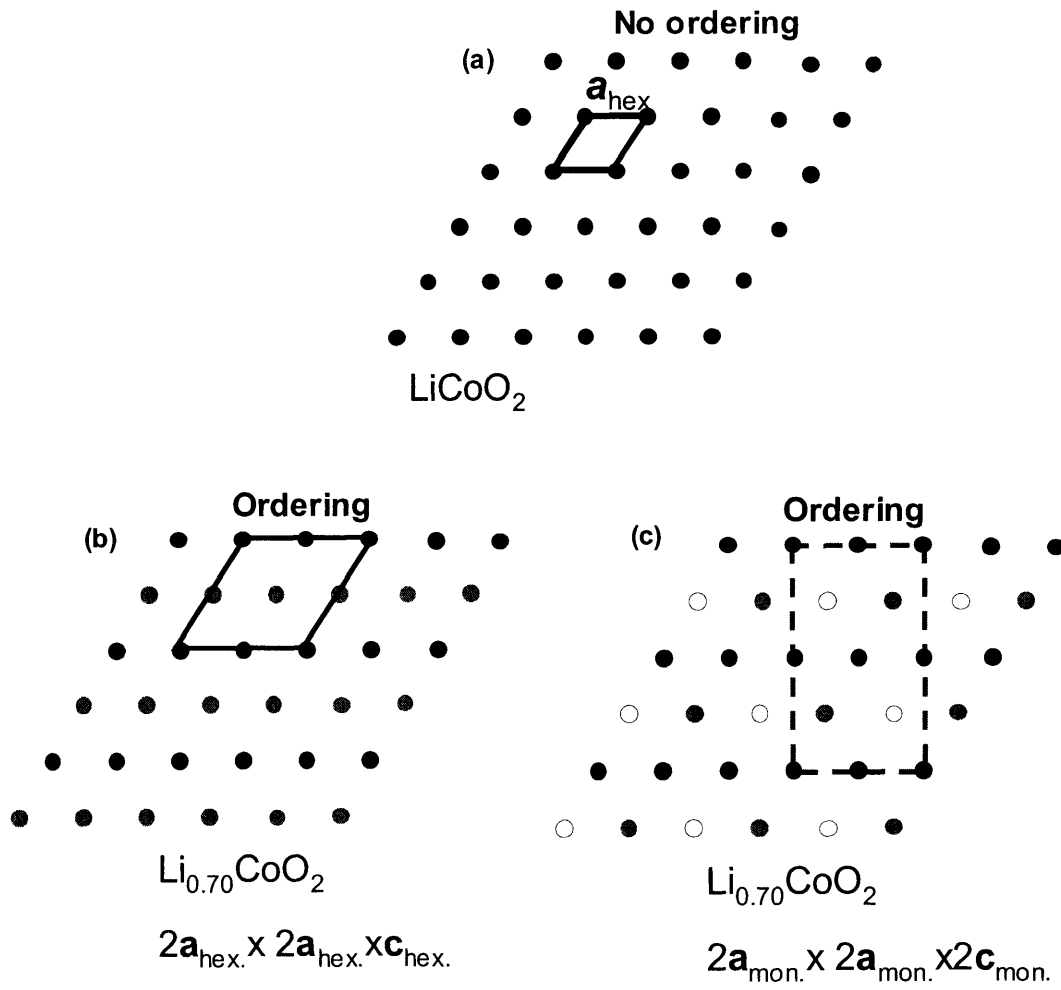


Figure 46: Electron diffraction patterns of a sample charged to a composition of  $\text{Li}_{0.7}\text{CoO}_2$  (on the left), compared with diffraction patterns of the  $\text{LiCoO}_2$  parent sample (on the right). The diffraction pattern of the charged sample has super-lattice reflections, indicated by white arrows.



**Figure 47: Schematics of (a) lithium ion positions in the  $\text{LiCoO}_2$  parent sample, (b) proposed lithium ion positions in  $\text{Li}_{0.7}\text{CoO}_2$  in a hexagonal cell and (c) proposed lithium ion positions in  $\text{Li}_{0.7}\text{CoO}_2$  in a monoclinic cell. The black dots represent lithium ions, the white dots represent vacancies and the gray dots represent a statistical distribution of lithium ions and vacancies.**

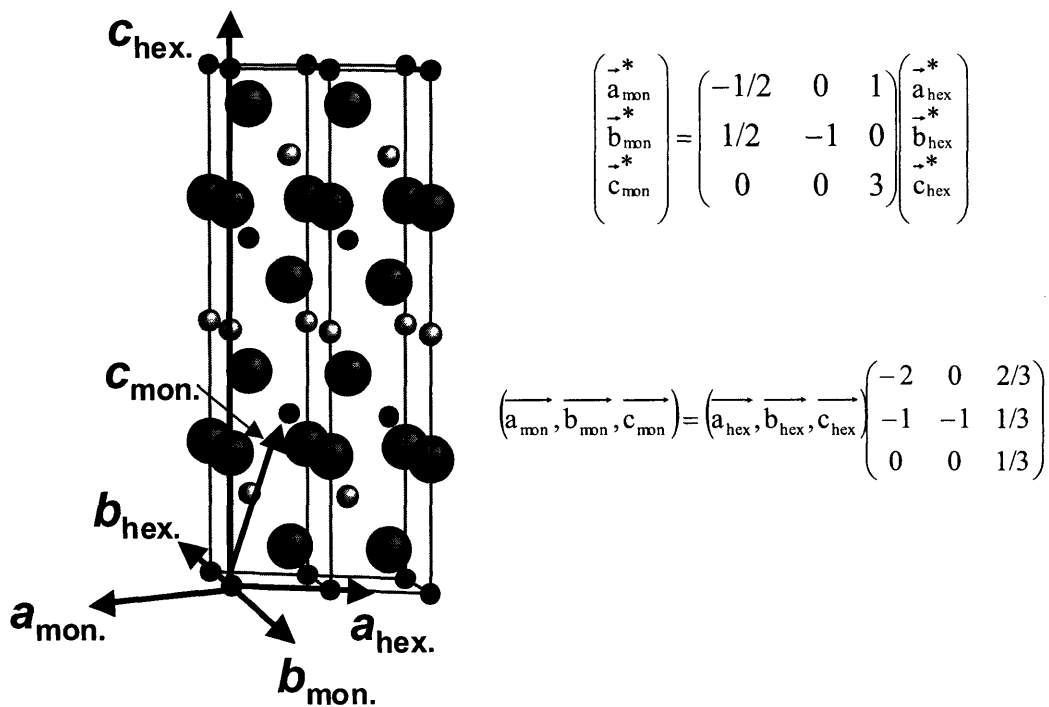


Figure 48: Crystallographic relationship between the hexagonal  $\text{LiCoO}_2$  and monoclinic cell.

**Samples charged to  $\text{Li}_{0.75}\text{CoO}_2$ :**

The diffraction patterns of charged  $\text{Li}_{0.75}\text{CoO}_2$  crystals also show extra reflections (Figure 49), indicating the presence of a supercell.

The same type of ordering as is proposed for  $\text{Li}_{0.7}\text{CoO}_2$  can be proposed for  $\text{Li}_{0.75}\text{CoO}_2$ , shows in Figure 50. The supercell is  $2a_{\text{hex}} \times 2a_{\text{hex}} \times c_{\text{hex}}$ . In the lithium planes, there are alternating fully occupied rows of lithium ions and half-occupied rows of lithium ions. There could be ordering in the half-occupied rows, where lithium ions occupy every other site along the row.

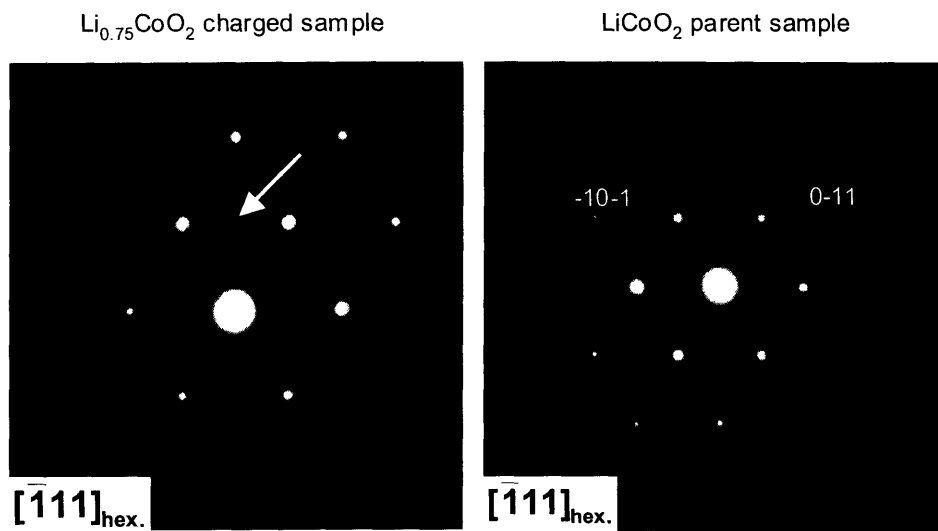


Figure 49: Electron diffraction pattern of a sample charged to a composition of  $\text{Li}_{0.75}\text{CoO}_2$  (on the left), compared with a diffraction pattern of the  $\text{LiCoO}_2$  parent sample (on the right). The diffraction pattern of the charged sample has super-lattice reflections, indicated by white arrows.

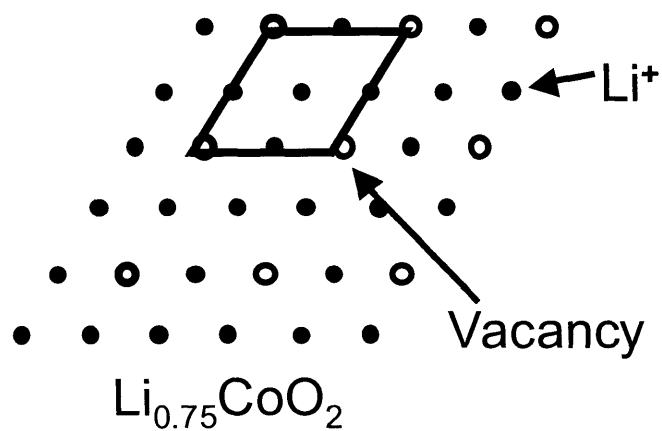


Figure 50: Schematics of lithium ion positions in  $\text{Li}_{0.75}\text{CoO}_2$  in a hexagonal cell. The black dots represent lithium ions and the white dots represent vacancies. The supercell is  $2a_{\text{hex}} \times 2a_{\text{hex}} \times c_{\text{hex}}$ .

### 3.2.2.3 Single-phase $\text{Li}_x\text{CoO}_2$ with a lithium content in the range 0.97 - 0.95

In Figure 51, an electron diffraction pattern collected from a  $\text{Li}_{0.97}\text{CoO}_2$  charged sample is presented alongside a pattern collected from  $\text{LiCoO}_2$  in the same zone axis. Weak spots are present in the diffraction pattern of the charged sample, which are not present in the diffraction pattern of the parent sample. There seem to be three weak diffraction spots between the central beam and the  $(2\ 0\ -1)$  reflection. Electron diffraction data reveal the presence of a  $2a_{\text{mon.}} \times 2b_{\text{mon.}} \times 4c_{\text{mon.}}$  supercell in  $\text{Li}_{0.97}\text{CoO}_2$ , shown in Figure 52. The presence of one vacancy per supercell corresponds to approximately 3% of vacancies in the material.

The lithium ions are coupled with the electrons in the material, and lithium ordering is correlated to the localization of charges. The localized charges are responsible for the semi-conductor behavior of the material at high lithium content. Extra reflections in electron diffraction patterns are most likely due both to localized charges and to localized vacancies.

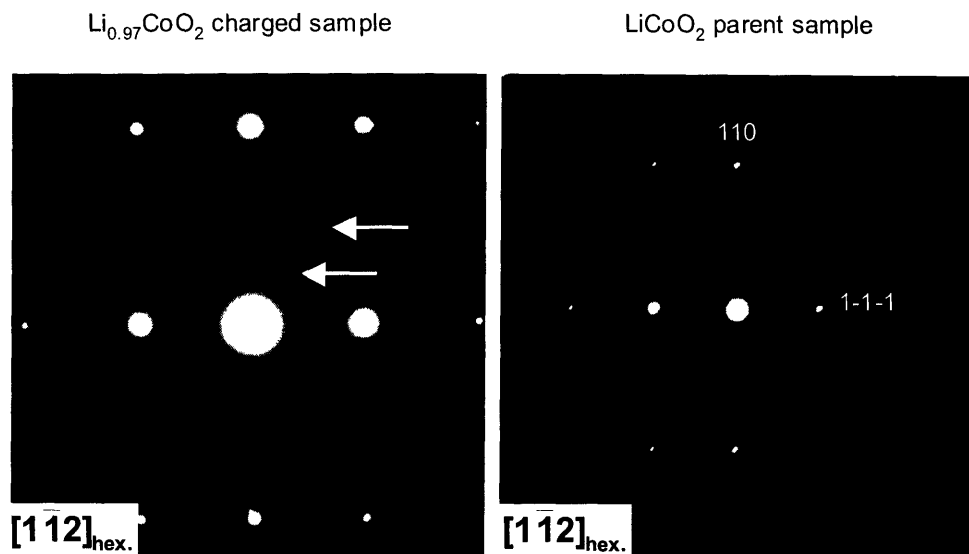


Figure 51: Electron diffraction pattern of a sample charged to a composition of  $\text{Li}_{0.97}\text{CoO}_2$  (on the left), compared with a diffraction pattern of the  $\text{LiCoO}_2$  parent sample (on the right). The diffraction pattern of the charged sample has super-lattice reflections, indicated by white arrows.

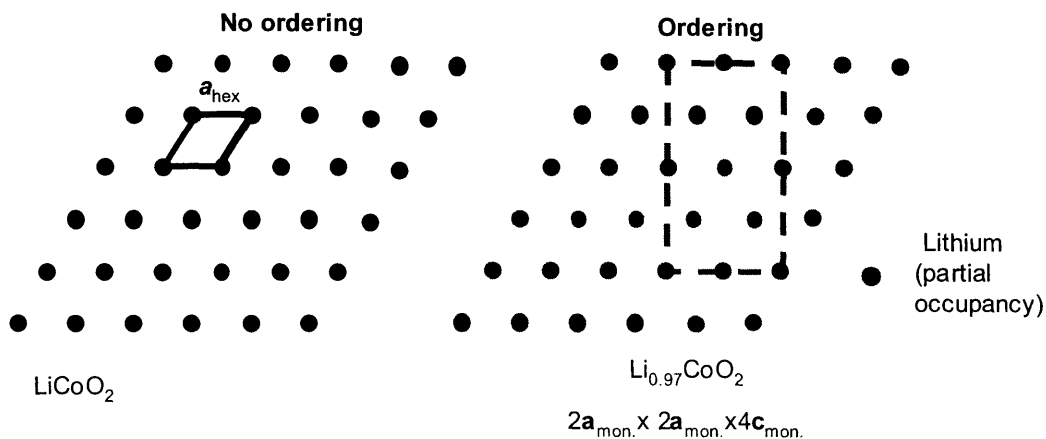


Figure 52: Schematics of lithium ion positions in  $\text{Li}_{0.97}\text{CoO}_2$  in a monoclinic cell. The black dots represent lithium ions and the gray dots represent sites partially occupied by lithium ions. The supercell is  $2a_{\text{mon.}} \times 2a_{\text{mon.}} \times 4c_{\text{mon.}}$ .



#### 3.2.2.4 Two-phase $\text{Li}_x\text{CoO}_2$ with a lithium content of 0.85

In Figure 53, electron diffraction patterns collected from  $\text{Li}_{0.85}\text{CoO}_2$  charged samples are presented alongside patterns collected from  $\text{LiCoO}_2$  in the same zone axis. Weak spots are present in the diffraction pattern of the charged sample, which are not present in the diffraction pattern of the parent sample. In the  $[0\ 0\ 1]$  zone axis, these extra reflections are present between the central beam and the  $(1\ 1\ 0)$  reflection. In the  $[-1\ 1\ 1]$  zone axis, these extra reflections are present halfway in between the central beam and the  $(-1\ -1\ 0)$  reflection.

These extra reflections indicate that a superstructure cell exists in the charged material and they can be explained by the lithium-vacancy ordering schematics proposed above. At a lithium content of  $x=0.85$ , the material is undergoing the insulator-metallic phase transition between  $\text{Li}_{0.94}\text{CoO}_2$  and  $\text{Li}_{0.75}\text{CoO}_2$ . Each crystal contains both phases, and the electron diffraction patterns show features from both phases. Therefore, the superstructure reflections in  $\text{Li}_{0.85}\text{CoO}_2$  can be explained by the ordering found in both the metallic  $\text{Li}_{0.75}\text{CoO}_2$  phase and the insulating phase with high lithium content.

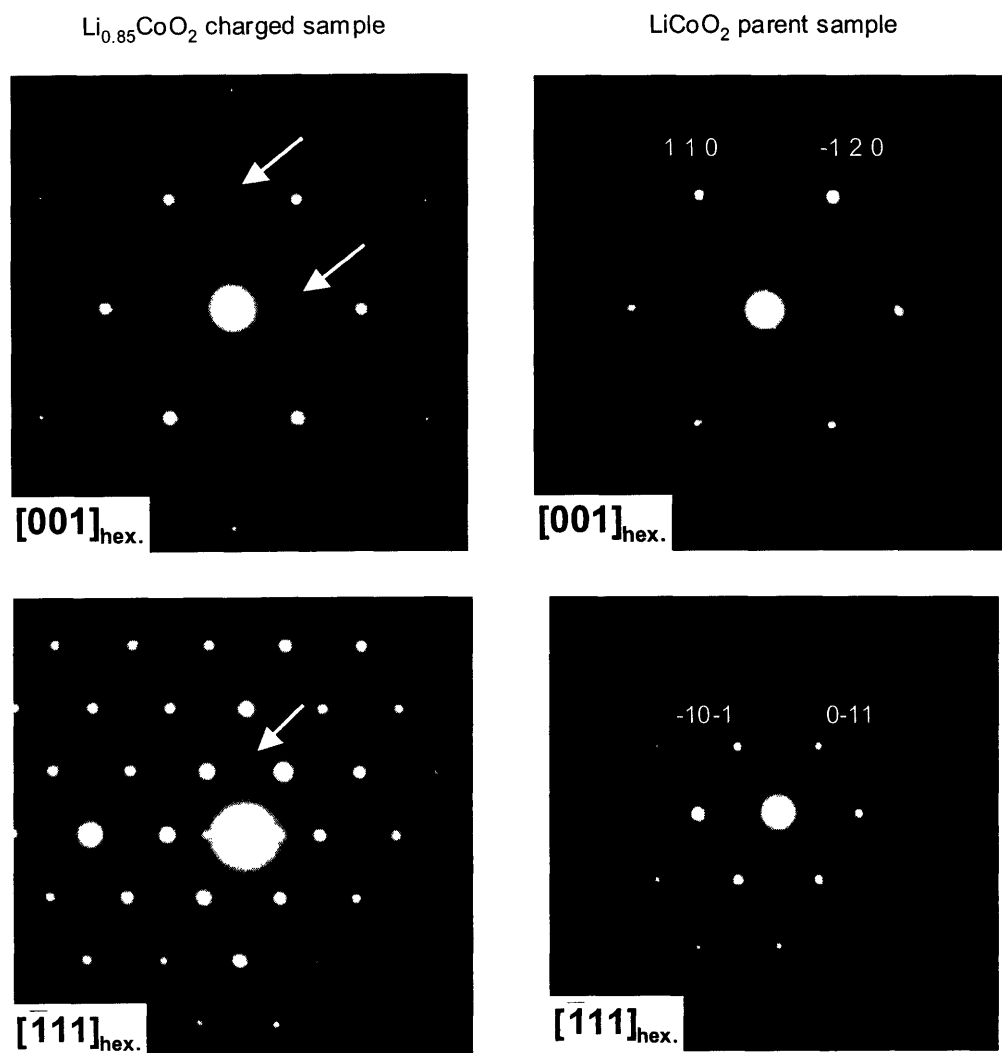


Figure 53: Electron diffraction patterns of a sample charged to a composition of  $\text{Li}_{0.85}\text{CoO}_2$  (on the left), compared with diffraction patterns of the  $\text{LiCoO}_2$  parent sample (on the right). The diffraction pattern of the charged sample has super-lattice reflections, indicated by white arrows.

### 3.2.2.5 Open questions

Other types of extra reflections have been noted in charged samples. Electron diffraction patterns from a charged  $\text{Li}_{0.85}\text{CoO}_2$  sample are shown in Figure 54. This type of super-structure reflections have also been seen in samples charged to other lithium contents, and cannot be explained by the lithium-vacancy ordering model.

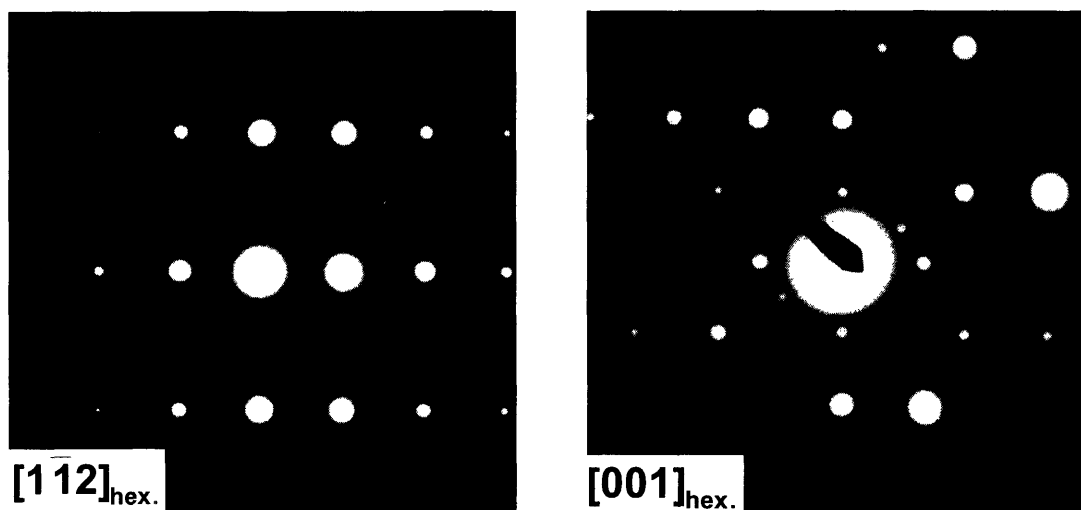


Figure 54: Electron diffraction patterns from a charged  $\text{Li}_{0.85}\text{CoO}_2$  sample. The proposed model cannot explain the super-lattice reflections present in these patterns.

### 3.2.2.6 Bright-field TEM images of charged $\text{Li}_x\text{CoO}_2$ samples

Bright-field images of charged  $\text{Li}_{0.85}\text{CoO}_2$  samples are shown in Figure 55. There are rounded features on the edges of the crystals and their diameter is on the order of 10-40nm. Contrast in these TEM images can come from thickness variations or from variations in the diffraction properties. SEM and AFM images of  $\text{Li}_x\text{CoO}_2$  crystals do not show this type of microstructure, so the contrast cannot be attributed to thickness variations. It is speculated that the contrast is due to differences in the diffraction properties of the insulator and the metallic phases. These microstructures could be domains of insulating and metallic phases, and the TEM image contrast could come from the slight lattice mismatch at the boundary between the phases. If this hypothesis holds true, the metallic phase nucleates in many different parts of the crystal and forms domains on the nanometer scale.

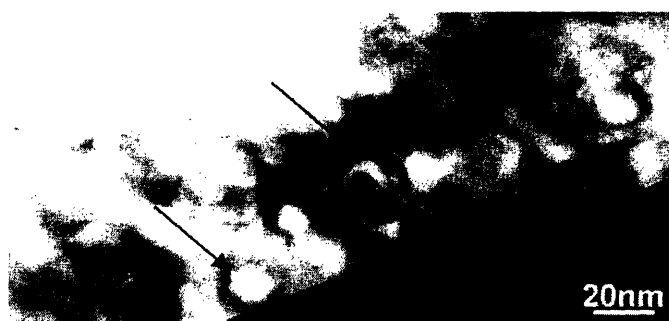
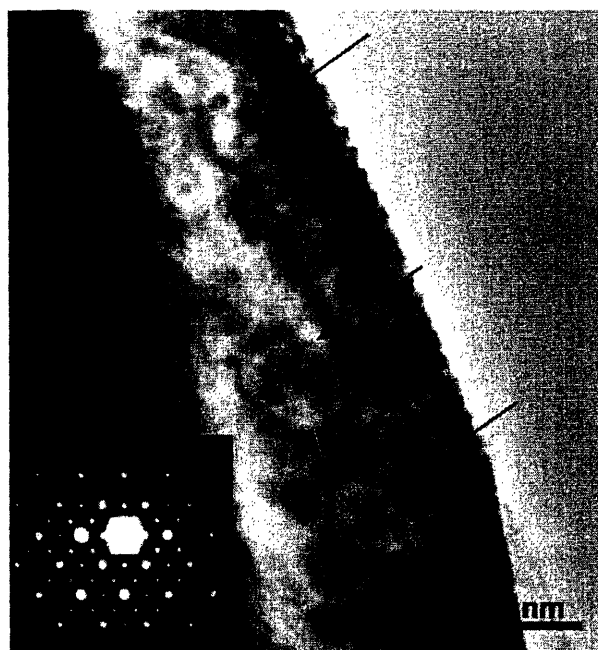


Figure 55: Bright-field TEM images of crystals charged to a lithium content of 0.85. There are microstructures on the edges of the crystals, which could correspond to domains of the insulating and the metallic phases.

### 3.2.2.7 General remarks

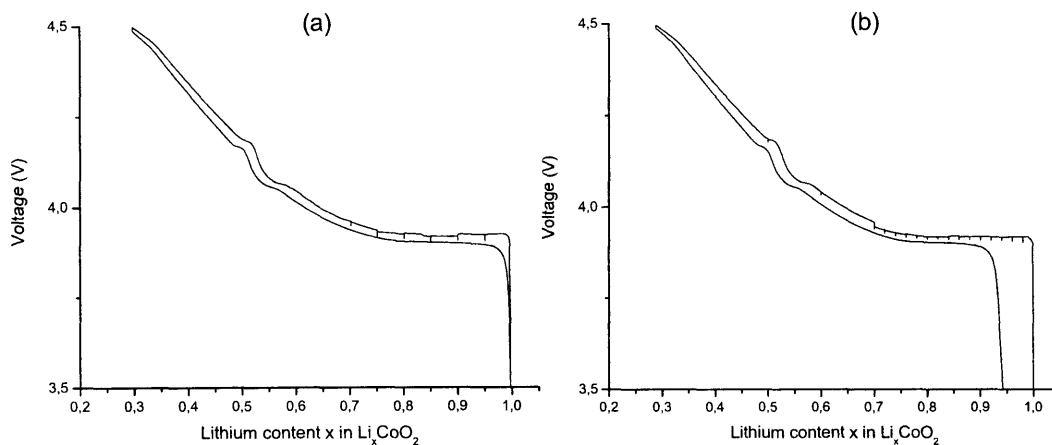
To conclude, superstructure reflections have been observed in charged crystals with lithium contents in the range of 0.97-0.7. The samples with high lithium content ( $x = 0.97$  to 0.95) are single-phase and semi-conductor. Their semi-conductor behavior is linked to charge localization, which is correlated to lithium-vacancy ordering. Both charge and lithium-vacancy ordering are speculated to be causing the superstructure reflections. As lithium ions are removed from  $\text{Li}_x\text{CoO}_2$ , a second phase is created and the material undergoes a two-phase transition from insulating to metallic. For lithium contents in the range of 0.75-0.7, the material is single-phase and metallic. Because of its high electronic conductivity, this phase most probably does not have charge localization. Lithium-vacancy ordering in the lithium layers is responsible for the super-structure reflections. Because the metallic phase is created from the insulating phase, it may retain some of the lithium ordering from that phase. For intermediate lithium contents (for example  $x = 0.85$ ), the material contains two phases and the electron diffraction patterns are a result of the two phases. Therefore, they also show superstructure reflections.

This work is the first study to report lithium-vacancy ordering in the two phases taking part in the insulator-metal transition, as well as the first observation of the presence of microstructural domains in charged crystals, which may be domains of the two phases.

### 3.2.3 Electrochemical Impedance Spectroscopy results and discussion

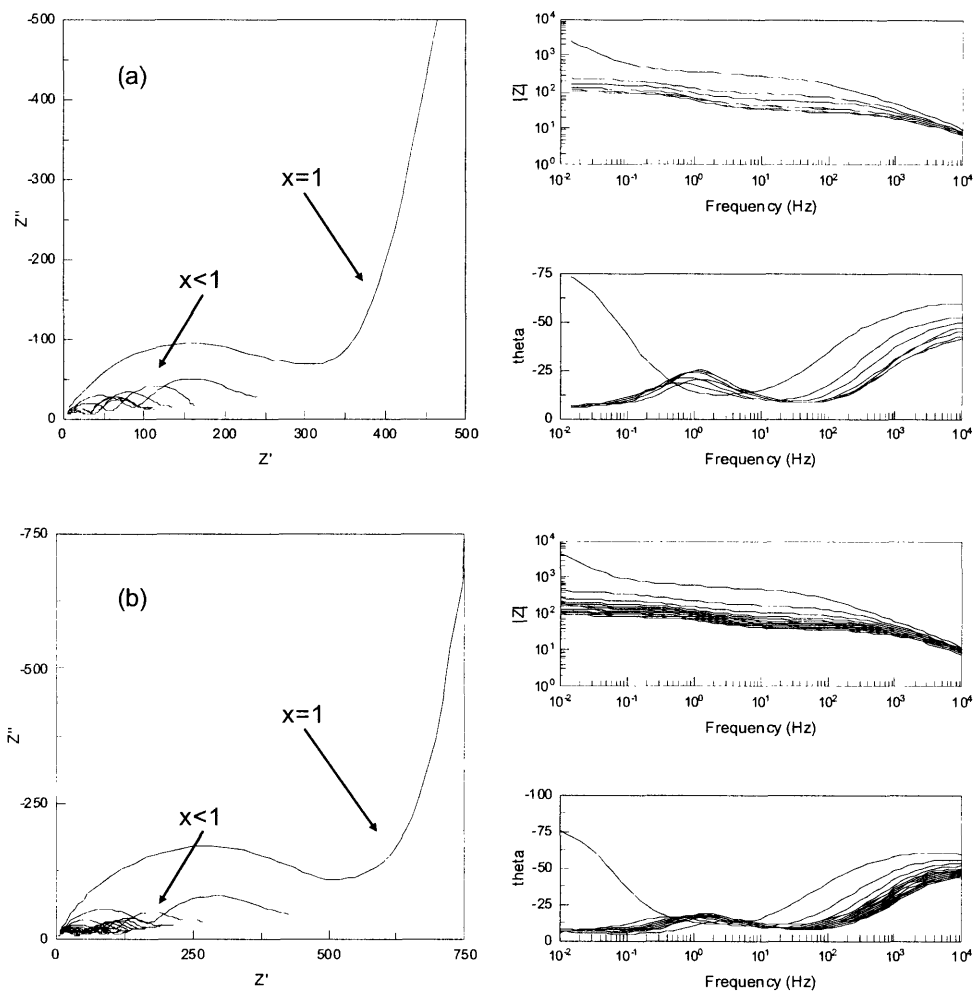
Electrochemical Impedance Spectroscopy gives information on the electronic and ionic properties of the battery components. AC impedance spectroscopy data was collected from two coin cells containing composite electrodes with  $\text{Li}_x\text{CoO}_2$ , in the range of voltages corresponding to the insulator-metal transition. Both coin cells were charged and discharged at the slow rate of C/100 and AC impedance spectroscopy data was measured at regular intervals. Before and after each AC impedance step the cell was allowed to reach equilibrium for 10 minutes at open circuit.

Figure 57 shows the Nyquist and Bode plots for two coin cells, and Figure 56 shows the corresponding galvanostatic charge plots. For a lithium content of  $x=1$ , the Nyquist plot has a depressed semi-circle in the high frequencies and a curved line at low frequencies. For lithium contents  $x<1$ , the Nyquist plots show two depressed semi-circles. Some of the plots also show a straight line at low frequencies. The higher-frequency semi-circle is typically associated with charge transfer and/or surface layers and the lower-frequency semi-circle with the electronic properties of the positive electrode. Both semi-circles become smaller with decreasing lithium content in  $\text{Li}_x\text{CoO}_2$ . The low-frequency line is usually modeled by a Warburg impedance and corresponds to ionic diffusion. It is assumed that the lithium metal negative electrode does not have a significant effect on the impedance data.



**Figure 56: Charge curves of cells 10 (a) and 14 (b), used in AC impedance measurements. Both coin cells were charged at a slow rate of  $C/100$  and the charge was interrupted in order to perform impedance spectroscopy measurements at different lithium contents. Measurements were taken at  $x=1, 0.95, 0.9, \dots 0.7$  for coin cell 083004b\_10 and at  $x=1, 0.98, 0.96, \dots 0.7, 0.6$  and  $0.5$  for coin cell 083004b\_14. Before and after each impedance step, the cell was allowed to reach equilibrium for 10min at open-circuit.**





**Figure 57: Nyquist and Bode plots of coin cells 083004b\_10 (a) and 083004b\_14 (b). Impedance was measured for frequencies ranging from 10kHz to 15mHz, with a perturbation voltage of 5mV.**

The AC impedance data were analyzed according to the equivalent circuit (a) shown in Figure 58 using the commercial software Zview from Scribner Associates. Circuits (b) and (c) were also tried for fitting the data, and they gave similar results to circuit (a). These equivalent circuits are inspired from those proposed by Nobili et al. [30].  $R_s$  corresponds to the electrolyte solution resistance. In circuits (b) and (c) a parallel RC component is added to account for the presence of surface layers on the electrodes. This component is omitted in circuit (a) because our impedance measurements are not conducted at high enough frequencies to measure the effect of surface layers with accuracy.  $C_{dl}$  stands for the double-layer capacitance,  $R_{ct}$  is the charge-transfer resistance,  $R_e$  is the electronic resistance of the positive electrode, and  $C_e$  is a capacitance associated with the rough nature of the composite positive electrode.  $Z_w$  is the Warburg impedance, corresponding to lithium ion diffusion in the electrode. In circuit (c), these RC components are placed in series. In circuits (a) and (b),  $C_{dl}$  is placed in parallel with  $R_{ct}$ , the parallel RC component containing  $R_e$  and  $C_e$ , and  $Z_w$ . This type of equivalent circuit was proposed by Bruce and Saidi and seems to be a better model of the physics of the system than a series arrangement of RC components [35]. The intercalation/de-intercalation mechanism of lithium ions into  $Li_xCoO_2$  is described as: a charge transfer step corresponding to electrons joining the conduction band, the electronic conduction in the bulk, and lithium ion diffusion in the bulk. Finally,  $C_{int}$  represents the intercalation capacity. The paragraph below gives more detail on certain parameters used in the fitting.

First, the intercalation capacity  $C_{int}$  was estimated from the low-frequency impedance value in each plot, according to the following equation [29] :  $C_{int} = -\frac{1}{(\omega Z_w'')_{\omega \rightarrow 0}}$

The value of the intercalation capacity was then fixed during the simulations. Shown in Figure 59, the intercalation capacity reaches a maximum at around 4V, corresponding to the two-phase transition occurring for lithium contents larger than  $x=0.75$ .

Then, simulations were run to evaluate the other parameters. In the simulations, constant-phase elements Q were used in place of the capacitances C:  $Z = \frac{1}{Q(j\omega)^\alpha}$ . If  $\alpha=1$ , the constant-phase element is equal to a capacitance.

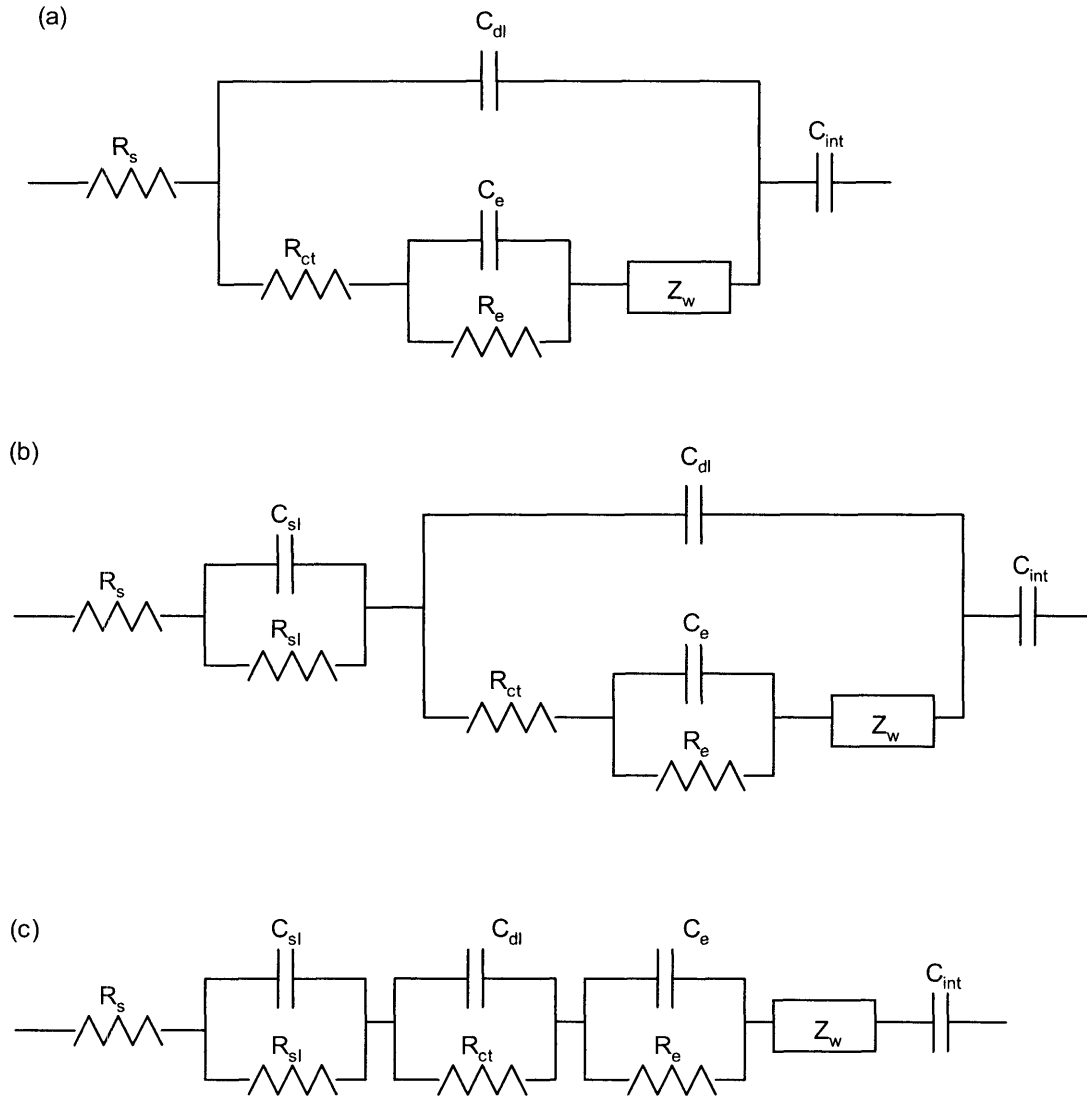
For a lithium content  $x=1$ , the values of the resistances and capacitances were evaluated by fitting each semi-circle independently. The low-frequency semi-circle is not entirely measured so fitting is more difficult. For lithium content lower than 1, the entire data set was used for fitting. The error bars on the graphs indicate the percentage of error in the fitting by Zview. The frequency range used for coin cell 083004b\_14 is broader than that used for coin cell 083004b\_14, so the fitting is more accurate.

Figure 60 shows the evolution of the electronic resistance  $R_e$  of the composite electrode as a function of lithium content  $x$  in  $\text{Li}_x\text{CoO}_2$ . The electronic resistance decreases by almost three orders of magnitude as lithium is pulled out of the positive electrode. The composite electrode is made of  $\text{Li}_x\text{CoO}_2$ , carbon and binder, and the decrease in  $R_e$  is attributed to the evolution of the electronic properties of  $\text{Li}_x\text{CoO}_2$  because the properties of the carbon and the binder are not expected to evolve. For  $0.75 \leq x \leq 1$ ,  $\text{Li}_x\text{CoO}_2$  undergoes a first-order phase transition from semi-conductor to metallic, consistently with the decrease of  $R_e$ . These results are in agreement with those of Nobili et al. [30].

Figure 61 shows the charge transfer resistance as a function of lithium content in  $\text{Li}_x\text{CoO}_2$ . As charge transfer and surface layer effects are recorded in the same frequency range, the surface layers will be accounted for in  $R_{ct}$  and  $C_{dl}$ . The charge transfer resistance decreases from around  $400\Omega$  to around  $50\Omega$  as lithium is pulled out of the material. This decrease in resistance could be attributed to the break-up or evolution of the surface layer covering the electrodes as the cell is charged. Nobili et al. also measure a slight decrease of  $R_{ct}$  at the onset of charge, but only from approximately  $350\Omega$  to  $200\Omega$ .

Finally, the Warburg impedance  $Z_w$  could not be evaluated with good precision because our ac impedance measurements were not conducted at frequencies lower than 10mHz for practical reasons. In fact, some of the complex plane plots do not even show the low-

frequency straight line characteristic of ionic diffusion. Therefore, this data could not be used to calculate the diffusion coefficient of lithium ions.



**Figure 58: Equivalent circuits modeling the behavior of lithium batteries. All of these circuits were used to fit the experimental data, with similar results. In the analysis of the data, circuit (a) was chosen because it is a better representation of the physics of a lithium battery.**

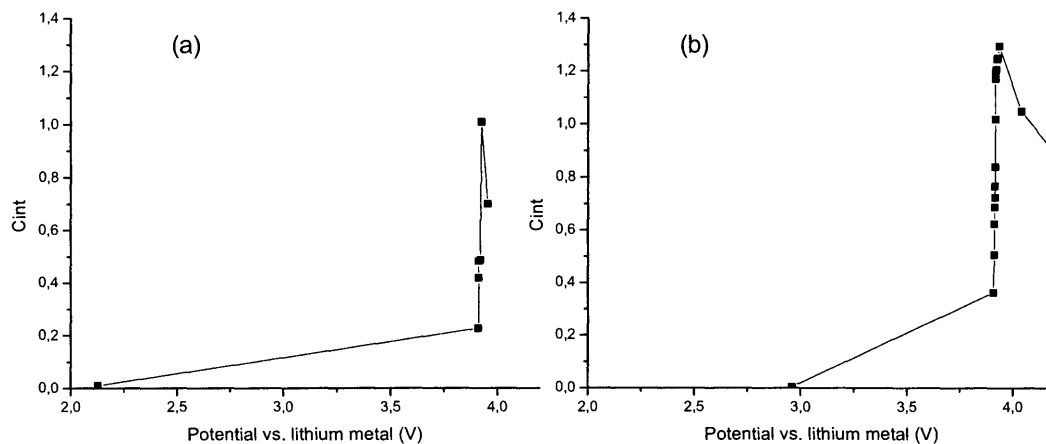


**Figure 59: Intercalation capacitance a function of lithium content  $x$ , for coin cells 083004b\_10 (a) and**

**083004b\_14 (b).  $C_{int}$  was calculated according to:  $C_{int} = -\frac{1}{(\omega Z_w'')_{\omega \rightarrow 0}}$**

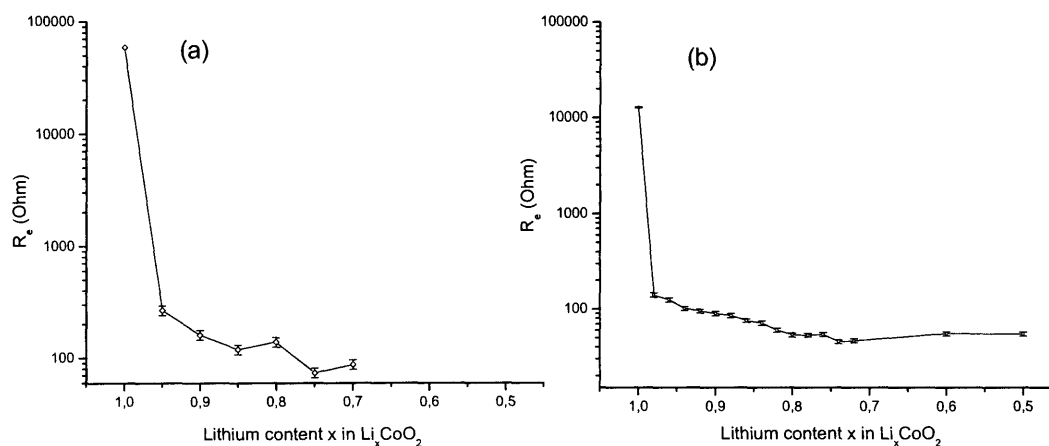


**Figure 60: Electronic resistance of the composite electrode as a function of lithium content  $x$ , for coin cells 083004b\_10 (a) and 083004b\_14 (b).  $R_e$  was assessed by fitting the AC impedance data according to the equivalent circuit (a) shown in Figure 58.**

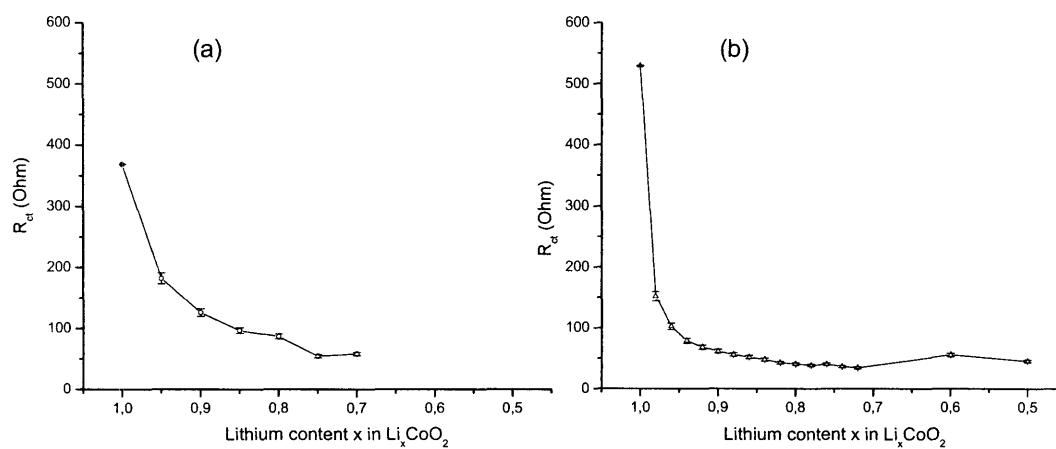


**Figure 61: Charge transfer resistance as a function of lithium content  $x$ , for coin cells 083004b\_10 (a) and 083004b\_14 (b).  $R_c$  was assessed by fitting the AC impedance data according to the equivalent circuit (a) shown in Figure 58.**

## Conclusion

The objective of this work was to examine the evolution of individual  $\text{LiCoO}_2$  crystals during lithium de-intercalation and intercalation. Atomic Force Microscopy and Transmission Electron Microscopy were used to image individual crystals with different lithium concentrations.

Atomic Force Microscopy was used in-situ to probe the dynamic evolution of  $\text{Li}_x\text{CoO}_2$  crystal morphology as lithium ions are de-intercalated and intercalated into the material. The overall crystal morphology did not show significant evolution during the first charge and discharge cycle however evidence was found for the expansion and contraction of crystal steps during cycling. During lithium de-intercalation, it was observed that the crystal step heights increased, reached a maximum and then decreased. The maximum expansion most probably corresponds to the hexagonal to monoclinic phase transition occurring for a lithium content of  $x=0.5$ . The evolution of layer spacing was quantified from AFM data and was found to be in agreement with X-ray diffraction studies by other researchers. Furthermore, rounded bumps were observed on the surface of most of the crystals, and these bumps decreased in size with time as the sample was left in the electrolyte. It is speculated that these bumps are  $\text{Li}_2\text{CO}_3$  impurities, formed on the surface of  $\text{LiCoO}_2$  after storage in air. Lastly, the formation of a surface layer on  $\text{Li}_x\text{CoO}_2$  crystals and the gold foil substrate was observed when the cell was over-discharged to approximately 2.5V.

Transmission Electron Microscopy was used to image individual  $\text{Li}_x\text{CoO}_2$  crystals for different values of lithium concentration in the range corresponding to the insulator-metal phase transition. Superstructure reflections were observed in electron diffraction patterns of charged  $\text{Li}_x\text{CoO}_2$  samples, indicating the presence of lithium-vacancy ordering in the insulating as well as the metallic phase. Bright-field images of charged  $\text{Li}_{0.85}\text{CoO}_2$  crystals also revealed the presence of microstructural features that could correspond to domains of the insulating and the metallic phases. In parallel, Electrochemical Impedance Spectroscopy and X-ray Diffraction were used to characterize the evolution of the electronic and structural properties of  $\text{Li}_x\text{CoO}_2$  during the phase transition. EIS data were



analyzed using an equivalent circuit inspired by the model proposed by Bruce and Saidi [35], and showed that the electronic resistivity of  $\text{Li}_x\text{CoO}_2$  decreased by three orders of magnitude at the onset of charge, in agreement with literature. XRD data from charged  $\text{Li}_x\text{CoO}_2$  samples showed an increase in layer spacing, in good agreement with previous studies done by other researchers.

To conclude, this work is the first study to examine the morphology of  $\text{LiCoO}_2$  crystals during cycling and shows the unique capabilities of AFM in the study of cathode materials for lithium batteries. Future work could couple AFM and AC impedance to study the propagation of the insulator-metal phase transition in individual crystals.

## References

1. Orman, H.J. and P.J. Wiseman, Cobalt(III) Lithium-Oxide,  $\text{CoLiO}_2$  - Structure Refinement by Powder Neutron-Diffraction. *Acta Crystallographica Section C-Crystal Structure Communications*, 1984. 40(Jan.): p. 12-14.
2. Ohzuku, T. and A. Ueda, Solid-State Redox Reactions of  $\text{LiCoO}_2$  (R3m) for 4 Volt Secondary Lithium Cells. *J. Electrochem. Soc.*, 1994. 141(11): p. 2972-2977.
3. Pereira, N., et al., Stoichiometric, Morphological, and Electrochemical Impact of the Phase Stability of  $\text{Li}_x\text{CoO}_2$ . *Journal of the Electrochemical Society*, 2005. 152(1): p. A114-A125.
4. Wang, H.F., et al., Electron Microscopic Characterization of Electrochemically Cycled  $\text{LiCoO}_2$  and  $\text{Li(Al,Co)O}_2$  Battery Cathodes. *Journal of Power Sources*, 1999. 82: p. 594-598.
5. Van der Ven, A., et al., First-Principles Investigation of Phase Stability in  $\text{Li}_x\text{CoO}_2$ . *Physical Review B*, 1998. 58(6): p. 2975-2987.
6. Reimers, J.N. and J.R. Dahn, Electrochemical and in-situ X-Ray-Diffraction Studies of Lithium Intercalation in  $\text{Li}_x\text{CoO}_2$ . *Journal of the Electrochemical Society*, 1992. 139(8): p. 2091-2097.
7. Amatucci, G.G., J.M. Tarascon, and L.C. Klein, Cobalt Dissolution in  $\text{LiCoO}_2$ -Based Non-Aqueous Rechargeable Batteries. *Solid State Ionics*, 1996. 83(1-2): p. 167-173.
8. Koltypin, M., et al., The Study of Lithium Insertion-Deinsertion Processes into Composite Graphite Electrodes by in-situ Atomic Force Microscopy (Afm). *Electrochemistry Communications*, 2002. 4(1): p. 17-23.
9. Ogumi, Z. and S.K. Jeong, Spm Analysis of Surface Film Formation on Graphite Negative Electrodes in Lithium-Ion Batteries. *Electrochemistry*, 2003. 71(12): p. 1011-1017.
10. Inaba, M., et al., Surface Film Formation on Graphite Negative Electrode at Elevated Temperatures. *Electrochemistry*, 2003. 71(12): p. 1132-1135.
11. Aurbach, D., Electrode-Solution Interactions in Li-Ion Batteries: A Short Summary and New Insights. *Selected Papers Presented at the 11th IMLB, Jun 22-28, 2002*. 119-121: p. 497-503.
12. Bullard III, J.W. and R.L. Smith, Structural Evolution of the  $\text{MoO}_3$  (010) Surface During Lithium Intercalation. *Solid State Ionics*, 2003. 160(3-4): p. 335-349.

13. Vidu, R., F.T. Quinlan, and P. Stroeve, Use of in-situ Electrochemical Atomic Force Microscopy (Ec-Afm) to Monitor Cathode Surface Reaction in Organic Electrolyte. *Industrial & Engineering Chemistry Research*, 2002. 41(25): p. 6546-6554.
14. Vidu, R. and P. Stroeve, Improvement of the Thermal Stability of Li-Ion Batteries by Polymer Coating of  $\text{LiMn}_2\text{O}_4$ . *Industrial & Engineering Chemistry Research*, 2004. 43(13): p. 3314-3324.
15. Campana, F.P., et al., In-situ Atomic Force Microscopy Study of Dimensional Changes During  $\text{Li}^+$  Ion Intercalation/De-Intercalation in Highly Oriented Pyrolytic Graphite. *Electrochemistry Communications*, 2005. 7(1): p. 107-112.
16. Ménétrier, M., et al., The Insulator-Metal Transition Upon Lithium Deintercalation from  $\text{LiCoO}_2$  : An Electronic Properties and  $^7\text{Li}$  NMR Study. *Journal of Materials Chemistry*, 1999. 9: p. 1135-1140.
17. Marianetti, C., Kotliar G., Ceder G., A First-Order Mott Transition in  $\text{Li}_x\text{CoO}_2$ . *Nature Materials*, 2004.
18. Gabrisch, H., R. Yazami, and B. Fultz, The Character of Dislocations in  $\text{LiCoO}_2$ . *Electrochemical and Solid State Letters*, 2002. 5(6): p. A111-A114.
19. Wang, H.F., et al., Tem Study of Electrochemical Cycling-Induced Damage and Disorder in  $\text{LiCoO}_2$  Cathodes for Rechargeable Lithium Batteries. *Journal of the Electrochemical Society*, 1999. 146(2): p. 473-480.
20. Li, J., et al., Studies on the Cycle Life of Commercial Lithium Ion Batteries During Rapid Charge-Discharge Cycling. *Journal of Power Sources*, 2001. 102(1-2): p. 294-301.
21. Choi, S.H., J. Kim, and Y.S. Yoon, A Tem Study of Cycled Nano-Crystalline HT- $\text{LiCoO}_2$  Cathodes for Rechargeable Lithium Batteries. *Journal of Power Sources*, 2004. 135(1-2): p. 286-290.
22. Yazami, R.O.Y., Gabrisch H., Fultz B., Mechanism of Electrochemical Performance Decay in  $\text{LiCoO}_2$  Aged at High Voltage. *Electrochimica Acta*, 2004. in press(in press): p. in press.
23. Gabrisch, H., R. Yazami, and B. Fultz, A Transmission Electron Microscopy Study of Cycled  $\text{LiCoO}_2$ . *Journal of Power Sources*, 2003. 119: p. 674-679.
24. Gabrisch, H., R. Yazami, and B. Fultz, Hexagonal to Cubic Spinel Transformation in Lithiated Cobalt Oxide - Tem Investigation. *Journal of the Electrochemical Society*, 2004. 151(6): p. A891-A897.

25. Shao-Horn, Y., et al., Probing Lithium and Vacancy Ordering in O3 Layered  $\text{Li}_x\text{CoO}_2$  (x Approximate to 0.5) - an Electron Diffraction Study. *Journal of the Electrochemical Society*, 2003. 150(3): p. A366-A373.
26. Choi, Y.M., et al., Effects of Lithium Content on the Electrochemical Lithium Intercalation Reaction into  $\text{LiNiO}_2$  and  $\text{LiCoO}_2$  Electrodes. *Journal of Power Sources*, 1995. 56(1): p. 25-30.
27. Barker, J., et al., An Electrochemical Investigation into the Lithium Insertion Properties of  $\text{Li}_x\text{CoO}_2$ . *Electrochimica Acta*, 1996. 41(15): p. 2481-2488.
28. Aurbach, D., et al., Common Electroanalytical Behavior of Li Intercalation Processes into Graphite and Transition Metal Oxides. *Journal of the Electrochemical Society*, 1998. 145(9): p. 3024-3034.
29. Levi, M.D., et al., Solid-State Electrochemical Kinetics of Li-Ion Intercalation into  $\text{Li}_{1-x}\text{CoO}_2$ : Simultaneous Application of Electroanalytical Techniques SSCV, PITT, and EIS. *Journal of the Electrochemical Society*, 1999. 146(4): p. 1279-1289.
30. Nobili, F., et al., An AC Impedance Spectroscopic Study of  $\text{Li}_x\text{CoO}_2$  at Different Temperatures. *Journal of Physical Chemistry B*, 2002. 106(15): p. 3909-3915.
31. Dokko, K., et al., Kinetic Characterization of Single Particles of  $\text{LiCoO}_2$  by AC Impedance and Potential Step Methods. *Journal of the Electrochemical Society*, 2001. 148(5): p. A422-A426.
32. Levi, M.D. and D. Aurbach, Impedance of a Single Intercalation Particle and of Non-Homogeneous, Multilayered Porous Composite Electrodes for Li-Ion Batteries. *Journal of Physical Chemistry B*, 2004. 108(31): p. 11693-11703.
33. Zhuang, G.V., et al.,  $\text{Li}_2\text{Co}_3$  in  $\text{LiNi}_{0.8}\text{Co}_{0.15}\text{Al}_{0.05}\text{O}_2$  Cathodes and Its Effects on Capacity and Power. *Journal of Power Sources*, 2004. 134(2): p. 293-297.
34. Menetrier, M., et al., The Insulator-Metal Transition Upon Lithium Deintercalation from  $\text{LiCoO}_2$ : Electronic Properties and Li-7 NMR Study. *Journal of Materials Chemistry*, 1999. 9(5): p. 1135-1140.
35. Bruce, P.G. and M.Y. Saidi, The Mechanism of Electrointercalation, in *Journal of Electroanalytical Chemistry*. 1992. p. 93-105.